University of California
Los Angeles

Accelerating Ultra-Short Electron/ Positron Bunches in Field Ionization Produced Plasmas

A dissertation submitted in partial satisfaction
of the requirements for the degree
Doctor of Philosophy in Electrical Engineering

by

MIAOMIAO ZHOU

2008

The dissertation of MIAOMIAO ZHOU is approved.

Francis F. Chen

Steven Cowley

Chandrashekhar Joshi

Warren B. Mori, Committee Chair

University of California, Los Angeles

2008

To my parents, who had more confidence in me than myself.

Table of Contents

List of Figures

List of Tables

Acknowledgments

First and foremost, I would like to express my great gratitude to my advisor Prof. Warren Mori. Without his guidance, it would not have been possible for me to conduct all the work in this dissertation. His academic expertise, positive attitude and kind personality have been key supporting factors for me throughout my research. I am also grateful to Prof. Chan Joshi for providing me with the valuable opportunity to participate in the experiments and to contribute to the collaboration. Working closely with him has been a great learning experience for me.

I would like to thank Chengkun Huang for helping me with many numerical and coding issues in QuickPIC and Wei Lu for many helpful discussions on a wide range of topics. I would also like to thank Viktor Decyk, Frank Tsung, Michail Tzoufras, Jay Fahlen and Ben Winjum for their help and discussion on the code framework, the Dawson cluster, the IDL scripts, etc.

During the E167 experiments, members of the collaboration have been very helpful in familiarizing me with the experiments and my discussions with them motivated several topics in this dissertation. I would like to acknowledge their help. They are Chris Clayton (who taught me a lot during the experiments), Ken Marsh and Devon Johnson from UCLA; Patric Muggli (who read several chapters of this dissertation and made suggestions), Prof. Tom Katsouleas, Erdem Oz, and Suzhi Deng from USC; Ian Blumenfeld, Neil Kirby, Mark Hogan, Rasmus Ischebeck, Dieter Walz and Prof. Robert Siemann from SLAC.

I would like to thank Prof. Francis Chen and Prof. Steve Cowley, for their very kind support as members of my comittee. Their feedback on my work was great encouragement for me.

Last but not least, I would like to thank my family and friends who stood behind me throughout my Ph.D. study, especially during the time of writing this dissertation. They have always been the source of my inspiration.

Vita

1978	Born, Wuxi, Jiangsu, China
1996–2000	B.S. in Physics, Tsinghua University, Beijing , China
2000–2002	Research Assistant in Electrical Engineering Department, Tsinghua University, Beijing, China
2002–2005	M.S. in Electrical Engineering, University of California, Los Angeles, California, U.S.A.
2005–present	Ph.D. candidate in Electrical Engineering, University of California, Los Angeles, California, U.S.A.

Publications

M. Zhou, C. E. Clayton, C. Huang, C. Joshi, W. Lu, K. A. Marsh, W. B. Mori, T. Katsouleas, P. Muggli, E. Oz, M. Berry, I. Blumenfeld, F-J. Decker, M. J. Hogan, R. Ischebeck, R. Iverson, N. Kirby, R. Siemann, D. Walz, "*Beam head erosion in self-ionized plasma wakefield accelerators*", Proceedings of PAC07, Albuquerque, NM, June 2007, p. 3064

I. Blumenfeld, C. E. Clayton, F-J. Decker, M. J. Hogan, C. Huang, R. Ischebeck, R. Iverson, C. Joshi, T. Katsouleas, N. Kirby, W. Lu, K. A. Marsh, W.

B. Mori, P. Muggli, E. Oz, R. H. Siemann, D. Walz and M. Zhou, *"Energy Doubling of 42GeV electrons in a meter scale plasma wakefield accelerator"*, Nature, 445, p. 741-744, 2007

C. Huang, W. Lu, M. Zhou, C. E. Clayton, C. Joshi, W. B. Mori, P. Muggli, S. Deng, E. Oz, T. Katsouleas, M. J. Hogan, I. Blumenfeld, F. J. Decker, R. Ischebeck, R. H. Iverson, N. A. Kirby, and D. Walz, *"Hosing instability in the blow-out regime for plasma wakefield"*, Phys. Rev. Lett., vol. 99, 255001, 2007

C. Huang, V. K. Decyk, C. Ren, M. Zhou, W. Lu, W. B. Mori, J. H. Cooley, T. M. Antonsen Jr., T. Katsouleas, *"QUICKPIC: A highly efficient particle-in-cell code for modeling wakefield acceleration in plasmas"*, J. Compt. Phys., 217, 658-679, 2006

W. Lu, C. Huang, M. Zhou, M. Tzoufras, F. S. Tsung, W. B. Mori, and T. Katsouleas, *"A nonlinear theory for multidimensional relativistic plasma wave wakefields"*, Phys. Plasmas 13, 056709, 2006

W. Lu, C. Huang, M. Zhou, W. B. Mori, and T. Katsouleas, *"A nonlinear kinetic theory for multi-dimensional plasma wave wakefields"*, Phys. Rev. Lett., vol. 96, 165002, 2006

E. Oz, S. Deng, T. Katsouleas, P. Muggli, C. D. Barnes, I. Blumenfeld, F-J. Decker, P. Emma, M. J. Hogan, R. Iverson, N. Kirby, P. Krejcik, C. O'Connell, R. H. Siemann, D. Waltz, D. Auerbach, C. E. Clayton, C. Huang, D. K. Johnson, C. Joshi, W. Lu, K. A. Marsh, W. B. Mori, M. Zhou, *"Ionization-induced electron*

trapping in ultrarelativistic plasma wakes", Phys. Rev. Lett., vol. 98, 084801, 2007

D. K. Johnson, D. Auerbach, I. Blumenfeld, C. D. Barnes, C. E. Clayton, F-J. Decker, S. Deng, P. Emma, M. J. Hogan, C. Huang, R. Ischebeck, R. Iverson, C. Joshi, T. Katsouleas, N. Kirby, P. Krejcik, W. Lu, K. A. Marsh, W. B. Mori, P. Muggli, C. O'Connell, E. Oz, R. H. Siemann, D. Walz, M. Zhou, "*Positron production by X rays emitted by betatron motion in a plasma wiggler*", Phys. Rev. Lett., vol. 97, 175003, 2006

S. Deng, C. D. Barnes, C. E. Clayton, C. O'Connell, F-J. Decker, R. A. Fonseca, C. Huang, M. J. Hogan, R. Iverson, D. K. Johnson, C. Joshi, T. Katsouleas, P. Krejcik, W. Lu, W. B . Mori, P. Muggli, E. Oz, F. Tsung, D. Walz, M. Zhou, "*Hose instability and wake generation by an intense electron beam in a self-ionized gas*", Phys. Rev. Lett., vol. 96, 045001, 2006

M. Zhou, C. E. Clayton, V. K. Decyk, C. Huang, D. K. Johnson, C. Joshi, W. Lu, W. B. Mori, F. S. Tsung, S. Deng, T. Katsouleas, P. Muggli, E. Oz, F-J. Decker, R. Iverson, C. O'Connell, D. Walz, "*Modeling self-ionized plasma wakefield acceleration for afterburner parameters using QuickPIC*", Proceedings of PAC05, Knoxville, TN, May 2005, p. 2905

W. Lu, C. Huang, M. Zhou, W. B. Mori and T. Katsouleas, "*Limits of linear plasma wakefield theory for electron or positron wake*", Phys. Plasmas 12, 063101, 2005

Abstract of the Dissertation

Accelerating Ultra-Short Electron/ Positron Bunches in Field Ionization Produced Plasmas

by

MIAOMIAO ZHOU

Doctor of Philosophy in Electrical Engineering

University of California, Los Angeles, 2008

Professor Warren B. Mori, Chair

The acceleration of ultra-short electron/positron bunches in field-ionization produced plasmas is studied through particle-in-cell (PIC) simulations. The 3D fully relativistic parallel PIC code QuickPIC[1] is able to model afterburner relevant plasma wakefield acceleration (PWFA) parameters due to the implementation of the quasi-static approximation. Several new physics packages, including field-ionization and radiation reaction, were added into QuickPIC so that it could be used to simulate frontier PWFA experiments. The wakes created by a short electron bunch in the blow-out regime when its self electric field ionizes a gas to produce the plasma is studied by comparing them with wakes created in pre-ionized plasmas. A criteria for the wake amplitude to scale similarly with drive beam parameters is obtained. A detailed simulation study of the energy doubling experiment at Stanford Linear Accelerator Center (SLAC) suggests that the much faster beam head erosion process in a field-ionized plasma is what causes the maximum energy gain to saturate as the plasma length is increased (as published in [2]). Other observations from the simulation such as beam scalloping, loss of charge from the defocusing field, azimuthally asymmetric wakes

due to emittance asymmetry are also discussed. A theoretical model that provides scalings for the head erosion rate in terms of beam/plasma parameters is described. The predictions from the model are in good agreement with simulation results. The first simulation study of a positron beam propagating in an extended length of field-ionized plasma is presented. Beam head erosion as well as the dynamic focusing followed by a stabilization of the beam envelope is observed. This simulation, which has beam parameters in the same range as those can be produced at SLAC, achieved multi-GeV energy gain for the tail of the positron beam in tens of centimeters of a field-ionized plasma.

CHAPTER 1

Introduction to Plasma Based Acceleration

The potential for ultra-high acceleration gradients has motivated extensive research in plasma-based acceleration during the nearly three decades since Tajama and Dawson[3] first proposed using an intense laser pulse to excite plasma waves for electron acceleration. Plasma is an ideal medium for high-gradient acceleration since it is already ionized and can support very large electric fields, on the order of the nonrelativistic wavebreaking limit $E_0 = m_e c\omega_p/e \simeq \sqrt{n_p(cm^{-3})}V/cm$[4], where $\omega_p = \sqrt{4\pi n_p e^2/m_e}$ is the plasma frequency and n_p is the plasma density. This limit for a typical plasma (e.g. $n_p = 10^{18}cm^{-3}$, $E_0 \simeq 100GV/m$) is several orders larger than the maximum electric field conventional radio frequency linear accelerators can sustain, $\sim 20MV/m$, partly due to the breakdown of the material of the wall in the structure. The high accelerating gradient in plasmas offers the promise of reducing the length of a future accelerator by at least three orders of magnitude, from kilometers to meters.

1.1 Basic concepts

In plasma based accelerators, a drive beam, either particle beam or laser pulse(s), propagates through a plasma, generating a plasma wave wake. The particle beam driven case is called Plasma Wakefield Accelerators(PWFA) and it was first proposed by Chen et. al. [5] in 1985. The laser driven case falls

into 3 categories depending on the normalized parameters of the laser. They are the Laser Wakefield Accelerator(LWFA) where the driver is a single short laser pulse, the Plasma Beat Wave Accelerator(PBWA) where the drivers are two lasers whose frequency difference generates a beat at the plasma frequency, and the Self Modulated Laser Wakefield Accelerator(SMLWFA) where a long laser pulse evolves into a train of pulses due to Raman forward scattering. Fig. 1.1 from [1] is reproduced here to illustrate the concepts behind these schemes. There are also studies of wakefields driven by multiple electron bunches or laser pulses,

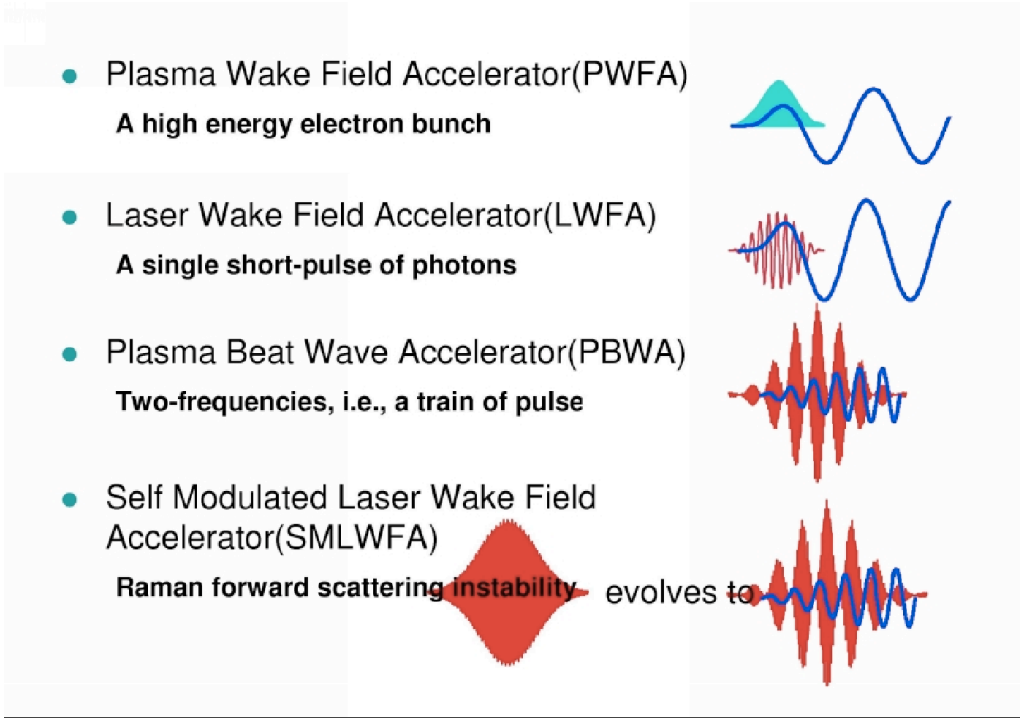

Figure 1.1: Four basic plasma based acceleration schemes(reproduced from [3]) (Solid blue lines: longitudinal electric field)

where the wakefield amplitude can be enhanced[6].

In the PWFA, wakefields are driven by forces associated with the space charge electric field of the particle beam. For a relativistic beam, $\mathbf{v}_b \approx \hat{z}c$, the dominant electric field is in the radial or transverse direction. This force can be expressed as $\mathbf{F} = -m_e c^2 \nabla_\perp \phi$, where ϕ is the normalized scalar potential $\phi = e\Phi/m_e c^2$ and is determined by a 2D Poisson's equation $-\nabla_\perp^2 \phi = 4\pi\rho_b$, where ρ_b is the charge desnity of the beam[1]. For laser driven plasma accelerators, the origin of the plasma wave is the ponderomotive force $\mathbf{F} = -m_e c^2 \nabla(\mathbf{a}^2/2)$, where $\mathbf{a}$ is the normalized vector potential $\mathbf{a} = e\mathbf{A}/m_e c^2$. This force comes from the second order motion of an electron in a laser field. (The first order is the "quiver motion" due to the electric field only $\mathbf{v_q} = c\mathbf{a}$)[7]. These driving forces displace the plasma electrons and generate a plasma wave after the particle beam or laser pulse passes by the plasma electrons and the more massive ions pull the electrons back.

1.2 Development of theories – from linear to nonliner, fluid to kinetic

In order to understand the underlying physics of plasma-based accelerators, numerous studies using theory, simulation and experiment have been carried out.

There are basically two types of models that can be used to describe the waves in a plasma – the fluid model and the kinetic model. The fluid models are effective as long as the plasma electron fluid velocity is less than the phase velocity of the plasma wave[8] and or the trajectories of individual electrons do not cross. In plasma-based accelerators, the plasma wave velocity equals the driver group velocity which is near the speed of light. In a 1D cold plasma, the condition that plasma particle trajectories cross each other is completely equivalent to the plasma density becoming infinite and the particle velocity exceeding the phase

velocity[9]. When narrow wakes are excited and multi-dimensional offsets are important, then trajectory crossing occurs. When these conditions are violated, a kinetic model must be used instead, where the evolution of the distribution function itself rather than its moments must be studied.

Let's begin by reviewing linear fluid theory. When the wakefields are weak enough (e.g. $\frac{n_b}{n_0} \ll 1$ or $|\mathbf{a}| \ll 1$) so that the perturbed plasma density excited by them are much smaller than the equilibrium plasma density ($\frac{n_1}{n_0} \ll 1$), then the wake is in the linear regime. In this regime, the fluid description is appropriate and the linearized fluid equations are sufficient to describe the wake. In particular, the equation for the perturbed density can be obtained from linearized fluid equations (Poisson's equation, the continuity equation, and the momentum equation) and can be written as[7]

$$(\frac{\partial^2}{\partial t^2} + \omega_p^2)\frac{\delta n}{n_0} = -\omega_p^2 \frac{n_b}{n_0} + c^2\nabla^2 \frac{a^2}{2} \tag{1.1}$$

where $a = 0$ for PWFA and $n_b = 0$ for laser-driven plasma accelerators. The solution for $\frac{\delta n}{n_0}$ can be obtained via Green's function. The equation for the accelerating electric field E_z can be written as

$$\nabla_\perp^2 E_z + \frac{\omega_p^2}{c^2} E_z = -\partial_\xi 4\pi e n_0 \frac{\delta n}{n_0} \tag{1.2}$$

where $\xi = z - ct$. (A similar equation exists for the radial electric field.) Based on this, E_z in a PWFA is given by [10]

$$E_z(r,\xi) = -4\pi \int_\xi^\infty d\xi' \rho_\parallel(\xi') \cos k_p(\xi'-\xi) \times \frac{k_p^2}{2\pi} \int_0^{2\pi} d\theta' \int_0^\infty dr' r' \rho_\perp(r',\theta') K_0(k_p|r-r'|) \tag{1.3}$$

where $\rho_\parallel(\xi)\rho_\perp(r,\theta) = \rho_b(r,\theta,\xi)$ is the beam charge density, and K_0 is the zeroth-order modified Bessel function of the second kind. Applying a bi-gaussian distribution in both longitudinal and transverse directions for the beam density, the

accelerating field on axis can be written as[11]

$$E_z(0,\xi) = [\sqrt{2\pi}(q/e)(mc\omega_p/e)(n_b/n_p) \times (k_p\sigma_z e^{k_p^2\sigma_z^2/2})R(0)]cos(k_p\xi), \qquad (1.4)$$

where

$$R(0) = k_p^2 \int_0^\infty r'dr'\rho_\perp(r')K_0(k_p r') \qquad (1.5)$$

For laser driven accelerators, the electric field can be written as [7]

$$\mathbf{E}(\mathbf{r},t) = -(m_e c^2\omega_p/e)\int_0^t dt' \sin\omega_p(t-t')\nabla a^2(\mathbf{r},t')/2 \qquad (1.6)$$

Although linear fluid theory can give useful expressions for quantities in plasma-based accelerators and is able to explain some basic issues, it is not always an accurate description of the real physics because the condition $\frac{n_1}{n_0} \ll 1$ is not always satisfied. Furthermore, the nonlinear multi-dimentional regime, where $\frac{n_1}{n_0} \simeq 1$ or $\frac{n_1}{n_0} > 1$, can be more favorable for accelerating electrons because the accelerating field is larger, the focusing fields are ideal, more charge can be accelerated, and a laser driver propagates more stably[12, 13].

Assuming the driver intensity is strong enough to excite a nonlinear plasma wave yet not too strong to make the plasma electron trajectories cross, a fluid model can still be used to describe the wake generation as long as we keep the nonlinear terms. The equation for the scaler potential derived from 1-D nonlinear fluid equations for beam drivers[12] and laser drivers[14] can be written together as[7]

$$k_p^{-2}\frac{\partial^2\phi}{\partial\xi^2} = \frac{n_b}{n_0} + \gamma_p^2\{\beta_p[1 - \frac{1+a^2}{\gamma_p^2(1+\phi)^2}]^{-1/2} - 1\} \qquad (1.7)$$

where $\beta_p = \frac{v_p}{c}$, $\gamma_p = (1-\beta_p^2)^{-1/2}$ and v_p is the phase velocity of the plasma wave. In principle, the self-consistent electric field can be obtained from Eq.(1.7) for any driver shape by differentiation. Compared with the 1-D results, the multi-dimensional results are much more complicated. In order to solve the 2-D or

3-D nonlinear fluid equations, numerical codes are usually needed, such as in [15] (beam driver) and [16](laser driver). No field expressions in general can be given explicitly. However, some common qualities, such as a highly peaked charge density, larger wake amplitude (may exceed E_0), steepened wave form and sometimes elongated wavelength (in highly nonlinear cases) were observed among different studies. These properties qualitatively agree with the 1-D theory predictions([13] Fig.1), and actually they qualitatively agree with PIC simulations which includes all nonlinearities and kinetic effects. Fig. 1.2(b) shows these nonlinear effects by comparing with the linear case(Fig. 1.2(a)). Both of them are produced by 3-D PIC simulations(QuickPIC). Recently, Lu et. al.[17][23], presented a nonlinear multi-dimensional theory for wakes excited by intense lasers and particle beams.

As the driver intensity further increases and the wake becomes nonlinear, one fundamental question that naturally comes to mind is what precisely determines the condition for the fluid model to break down and at what wave amplitude (the "wavebreaking" amplitude) does this occur. Studies have been carried out on this topic since 1950s, starting with a cold nonrelativistic 1-D plasma. The famous expression $E_0 = \frac{m_e c \omega_p}{e}$ was obtained by recognizing that the maximum E field arises when simultaneously, sheet crossing, particle trapping, and wave steeping occur[4]. Later, it was found that relativistic velocity of the fluid elements will increase the wavebreaking amplitude[18] while a finite plasma temperature can reduce it[19]. It was not until 1988 that both effects were considered and the limit was obtained for a warm relativistic plasma as $E_{max} = mc\omega_p e^{-1}\beta^{-1/4}(\ln 2\gamma_{ph}^{1/2}\beta^{1/4})^{1/2}$[20], where $\beta = 3T_{th}/mv_{ph}^2$. All these 1-D conclusions were re-derived in a unified treatment in [9], where the correct nonlinear fluid equations (either in Eulerian coordinate or Lagrangian coordinate[21]) were derived for each case first, and then a correspondingly feasible form of the wavebreaking condition was applied. In 2-D and 3-D, however, there is no sys-

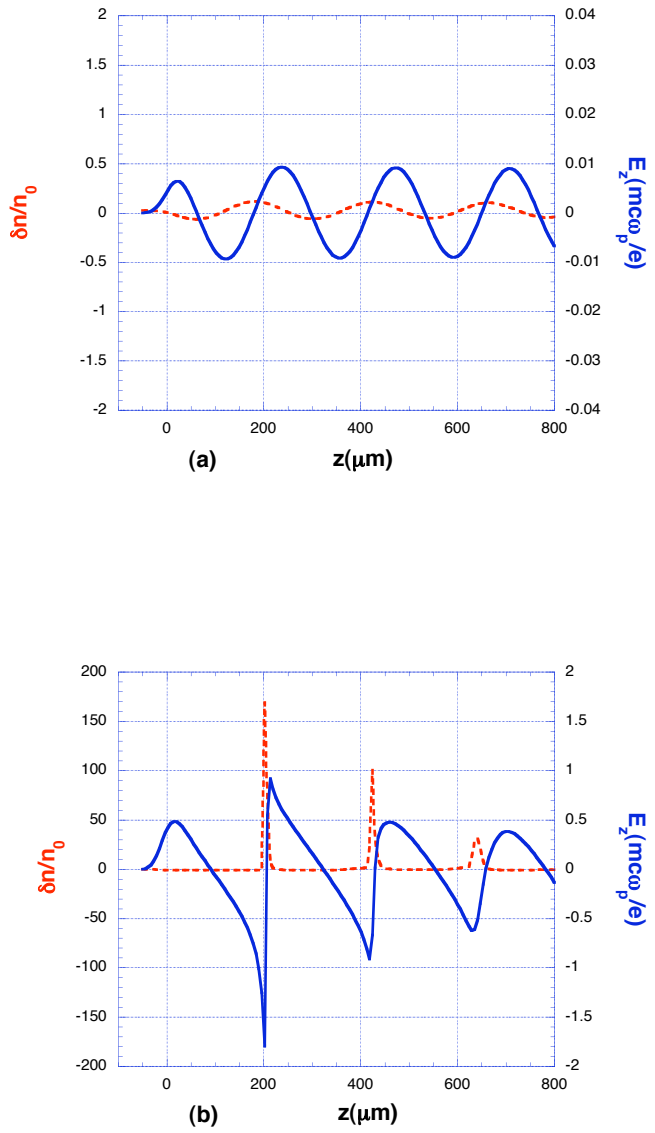

Figure 1.2: (a) Linear plasma wake ($\frac{n_b}{n_p} = 0.079$) and (b) nonlinear plasma wake ($\frac{n_b}{n_p} = 10$). Both (a) and (b) have a bi-gaussian beam with $\sigma_r = 10\mu m$, $\sigma_z = 20\mu m$ at $z = 0$. Only difference is number of electrons in the beam.

tematic wavebreaking study based on nonlinear fluid equations because the precise meaning of wavebreaking, particle trapping, and trajectory crossing becomes blurred. Simulations are normally used to search for the maximum coherent wave that the plasma is able to support, which remains a fundamental question of interest in multi-dimensions.

In the multidimensional nonlinear regime, the fluid model breaks down, and a kinetic model becomes necessary. Kinetic descriptions are usually achieved either by solving the plasma kinetic equations numerically (e.g. Vlasov or Fokker-Plank equations) or by particle simulation, which straightforwardly computes the motions of a collection of charged particles, self-consistently interacting with each other and with externally applied fields. The later can be thought of as solving the Klimontovich equation for finite size paricles. The first method has been used successfully in some areas, such as laser plasma interactions and magnetic fusion. However, because it treats phase space as a continuum, there has always been difficulties in finding an accurate yet economical representation of velocity space in long-time simulations, especially for multidimensional problems[22]. This will be particularly an issue in plasma-based acceleration where the bulk plasma is cold and the average momentum is large. On the other hand, particle simulation is more adaptable and has already played an important role in this field for many years. It propelled this field in two basic ways. Firstly, it helped to explore the essential physical processes involved in plasma-based acceleration, including nonlinear plasma wave excitation[23]; the self-consistent evolution of drivers, such as the self-focusing of short laser pulses[24] and the hosing instabilities[25] and head erosion[26] of the electron beam; as well as other important mechanisms such as self-injection through particle trapping[27]. Secondly, it has been used to model ongoing experiments to confirm and explain the experimental observations[28][29][2] and to help choose optimal parameters for future

experiments[30][31]. With the complexity in theories and considerable cost of experiments, particle simulations has become an essential tool in plasma-based acceleration study.

This dissertation will focus on the use of PIC simulation to study PWFA. Chapter 2 will introduce the afterburner relevant PWFA experiments and summarize their recent findings and current status. Chapter 3 will give an introduction to PIC codes in general and the quasi-static PIC code, QuickPIC, which is the tool used for this dissertation. Several new models were added into QuickPIC in order to simulate the current experiments, and they will be explained in Chapter 4. Chapter 5 to 7 will show results from simulations of electron beam driven PWFAs and explain some important physics mechanisms involved. The simulation findings of positron beam driven PWFAs will be discussed in chapter 8.

1.3 Experimental achievements

Before going into more detail of PWFA, which is the topic of the rest of this dissertation work, we review the major experimental milestones in plasma-based accelerator research using both particle beam and laser drivers.

Successful experiments before 1996 where electron acceleration was observed were summarized in [7]. We can see the accelerating gradient was much larger for laser drivers (up to 100GV/m) than beam drivers (up to 30MV/m). This is basically because the laser drivers were much stronger than the beam drivers for the state-of-the-art technology at that time. The laser intensities were up to $10^{19} W/cm^2$, while the maximum beam intensities were only around $10^{12} W/cm^2$. However, since the relativistic beams were much 'stiffer' than the laser pulses,

they were able to propagate much longer in a plasma, resulting in a similar energy gain(30MeV in $\approx$ 1 meter[32]) as compared to the laser driver case (44MeV in $\approx 0.44mm$[33]). The 'stiffness' of the drivers are represented by $\gamma = \frac{1}{\sqrt{1-(v_b/c)^2}}$ for beam drivers and $\gamma_{eff} = \frac{\omega_0}{\omega_p}$ for laser drivers, where ω_0 is the laser frequency. For the two maximum energy gain experiments prior to 1996([32][33]), a $500MeV$ electron beam with $\gamma = 978$ was used, and a laser pulse with $\lambda = 1.05\mu m$ in $n_p = 10^{19}cm^{-3}$ plasma with $\gamma_{eff} = 10$ was used. Another big difference between these two experiments (and most beam driven and laser driven experiments then) was that the electrons being accelerated in the beam driven case were from the beam tail while those in the laser driven case came from the background plasma. This is actually a direct result of the larger gradient and relatively slower phase velocity of the wake in laser driven experiments. In order for an initially stationary background electron to catch up with the driver, it has to be accelerated in a large enough gradient fast enough before it slips back into the decelerating region of the wake.

Large progress in experiments has been made in the past ten years for both types of drivers. For LWFA, higher power, short-pulse laser sources ($40TW$, $30fs$) have become available and technologies have been developed to guide intense lasers (e.g. by a preformed plasma density channel[34] or self-guiding), resulting in longer propagation distances. In 2004, three different groups reported production of $\sim 100MeV$ self-injected electron beams with $<\approx 10\%$ energy spread [35][36][37]. And recently, self-trapped electrons with energies near $1GeV$ were observed[38]. For PWFA, the progress has been tremendous due to the access to the worlds most intense electron beam at the Stanford Linear Acceleration Center (SLAC). The maximum beam intensity at SLAC is currently $10^{21}W/cm^2$ due to the ability to produce short beams ($\sigma_z \sim 10\mu m$). Interestingly, this is comparable to today's most powerful lasers[39]. Recently, some electrons in the

tail of the 42GeV SLAC beam were doubled in energy in only $85cm$ of a lithium plasma[2]. This is a remarkable achievement when one realizes that it took ~ 3 kilometers for the electrons to gain their initial 42GeV of energy. Although there are still issues that need to be solved, these recent experimental results in both LWFA and PWFA provide hope for the realization of practical plasma-based accelerators.

CHAPTER 2

Plasma Wakefield Accelerator Experiments

There has been a very close connection between the advances in particle-in-cell methods and in experimental results for plasma-based accelerator research. This has remained true during the SLAC/UCLA/USC E-164/167 collaboration. This close connection is important because understanding the experimental realities points the way towards adding the necessary realism into the models and the simulations help to unravel the physical phenomena from the experimental data as well as help design new experiments. In the past few years, this collaboration has yielded a number of rich new beam and plasma physics results and demonstrated key physics milestones for a beam-driven plasma afterburner. As part of the E164-167 collaboration, the author participated in several experimental runs carried out at Stanford Linear Accelerating Center (SLAC). In this chapter, the concept of a plasma afterburner will be introduced, the experimental setup at SLAC will be described, and the major experimental results will be summarized.

2.1 Original conceptual design of a plasma afterburner

The idea of a plasma afterburner or energy doubler dates back to the earliest work on PWFA. However, until recently, the necessary physics understanding was not mature enough to propose a realistic set of design and scaling laws. During the SLAC/UCLA/USC collaboration, a more detailed description of the

plasma afterburner was proposed[40]. The paper detailed how the energy of the 50GeV Stanford Linear Collider (SLC) electron and positron beams could be doubled using several meter long plasma sections. One of the promises of this specific design was possibly reaching the high energy frontier so that the SLC facility could have been used to search for the Higgs boson, which according to the standard model exists at energies above 100GeV. This energy was beyond the reach of both SLC and Large Electron Positron Collider (LEP) at CERN. Furthermore, the afterburner concept and design of [40] has been extended to possible International Linear Collider (ILC) designs.

The conceptual design is illustrated in Fig. 2.1 (reproduced from [40]). The electrons and positrons are accelerated to the collider's nominal energy ($\sim 50GeV$ for SLC), overcompressed to form two microbunches each, and then the trailing bunches are doubled in energy over a few meters in the plasma. To sustain the luminosity at the interaction point (IP), a shorter section of high density plasma can be used as a plasma lens to focus the trailing bunch.

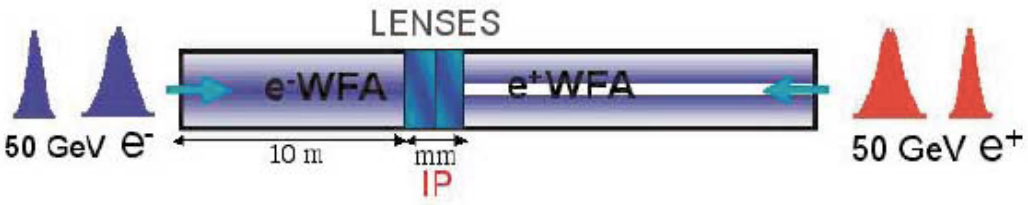

Figure 2.1: Conceptual design of a plasma afterburner (reproduced from [40])

This design was made possible based on a finding (through simulations) that a scaling based on linear theory [41] where the wakefield amplitude is inversely proportional to the square of the bunch length (Eq.(2.1)) still approximately holds even in the nonlinear regime[11]. This indicates the possibility of enhancing the

accelerating gradient by further reducing the bunch length,

$$eE_0 \approx 240(MeV/m)(\frac{N}{4\times 10^{10}})(\frac{0.6mm}{\sigma_z})^2 ln(\sqrt{\frac{10^{16}cm^{-3}}{n}}\frac{50\mu m}{\sigma_r}). \qquad (2.1)$$

for narrow bunches[11].

The viability of this idea was tested by looking at the wakefields excited by the electron beams with the then nominal SLC beam parameters except with smaller bunch lengths. For example, a beam with 3×10^{10} electrons in a bi-Gaussain distribution of radius $\sigma_r = 25\mu m$ and $\sigma_z = 63\mu m$ (10 times shorter than the original SLC beam but several times longer that what is currently available) can excite a wake with both the useful accelerating field (E_{acc}) and the decelerating field (E_{dec}) around $10GV/m$ under the optimal plasma density (chosen to be $1.8 \times 10^{16}cm^{-3}$ according to $k_p\sigma_z \approx \sqrt{2}$ from the linear theory[41]). In this case, the transformer ratio ($\equiv E_{acc}/E_{dec}$) is approximately 1 and suggests the stopping of the initial $50GeV$ driving bunch (pump depletion) in a few (~ 5) meters and the doubling the energy of the trailing bunch energy to $\sim 100GeV$ in this distance.

The realization of the above promise is contingent upon a lot of physics and technological issues being understood and overcome. Several of these were identified as being the most important. Among these are (i) beam loading and phasing, where a trade-off between higher energy and smaller energy spread needs to be optimized and understood; (ii) transverse beam dynamics, where the hosing instability predicted by theory which may potentially breakup the beam should be prevented; (iii) developing a plasma source, where producing a sufficiently long and dense enough high-density plasma source remains a challenge for laser photoionization technology; and (iv) positron acceleration, where the wake made by positron beams is typically smaller than that from a corresponding electron beam and where wake excitation behaves differently in the nonlinear regime.

Based on this afterburner concept, a series of "afterburner relevant" experiments have been carried out at SLAC. Some of the critical issues mentioned above have been resolved (e.g. long high-density plasma source), some have been explored with much progress being made (e.g. positron acceleration, greatly reduced hosing growth) and some still needs to be further addressed (e.g. beam loading). At the same time, as the experiments progressed, new issues arose (e.g. higher optimal plasma density required, beam head erosion, trapped particles). These new phenomena are physically interesting themselves and are also critical in the realization of the afterburner. In the following sections, the experimental setup and major results from the SLAC experiments will be summarized and an update on the latest afterburner design for the ILC will be given.

2.2 Experimental setup at SLAC

The experimental setup at the Final Focus Test Beam (FFTB) at SLAC has evolved and improved over the years. Fig. 2.2 shows the layout of the most recent energy doubling experiment[2]. A 50 femtosecond long ($\sigma_z \sim 15\mu m$) 42GeV electron beam (propagating from left to right) containing 1.8×10^{10} particles is focused to a spot size of $\sim 10\mu m$ at the entrance of a 85 cm long column of lithium vapour ("plasma oven") with a density of $2.7 \times 10^{17} cm^{-3}$. The beam exiting the plasma traverses a meter-long dipole magnet ("spectrometer magnet"), which disperses the beam electrons according to their energy. In order to distinguish the particles' displacement due to their energy change (gain or loss) from their possible vertical deflection while exiting the plasma, the spectra are measured at two different locations ("e^- spectrum" after the plasma). At each of the locations, the particle distribution is measured by Cerenkov radiation emitted as the electrons pass through a $15mm$ air gap established by two silicon wafers

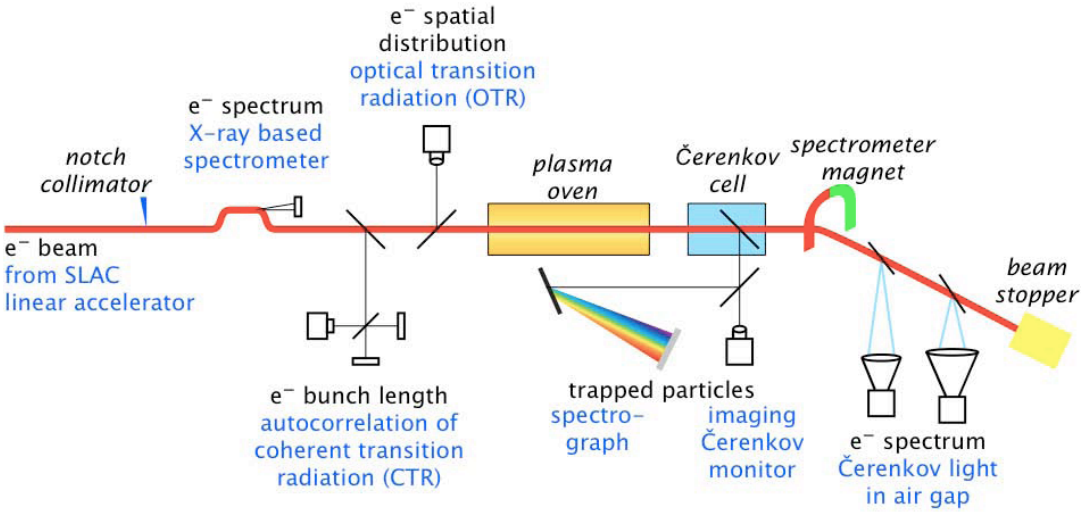

Figure 2.2: Schematic of the experimental layout [31]

(shown as one in Fig. 2.2), positioned at an angle of 45 degrees to the beam. The second wafer acts as a mirror and deflects the Cerenkov light into a lens that images the origin of the light onto a cooled charged coupled detector (CCD). The reason for using the Cerenkov light instead of directly measuring the particle distribution using phosphor is to prevent the interference from x-rays emitted while the beam undergoes betatron oscillations inside the plasma. The electrons pass the wafers almost unperturbed.

Many other diagnostics were developed to assist the beam tuning and better understanding of the beam-plasma interactions. These include the incoming beam energy spectrum measurement ("e^- spectrum" before the plasma), where the horizontally energy dispersed beam is sent to a vertical magnetic chicane, and its synchrotron radiation is recorded on a phosphor screen; the Michelson autocorrelator ("e^- bunch length"), which can be used to measure the bunch length and the average bunch profile using the coherent transition radiation (CTR) generated when the beam passes a Ti foil; and the beam transverse profile measurement

("e^- spatial distribution"), where the beam's transverse distribution is recorded through an optical transition radiator (OTR) before and after (not shown) the plasma oven. A "Cerenkov cell" filled with one atmosphere of Helium gas was used to study trapped particles by imaging the far field of the light (Cerenkov ring). The "spectrograph" records the spectrum of plasma light, including the beating pattern which may infer the spacing between bunches of trapped particles. Before the incoming energy measurement, a notch collimator was also developed to generate two bunches by making a cut in the longitudinal direction of the beam (by making use of the energy-time correlation in a energy dispersed region). The idea was to separate the accelerated particles from the rest of the beam so that a mono energetic beam could be generated.

2.3 Major results from the SLAC experiments

Tremendous progress has been made during the past 7 years from the PWFA experiments at SLAC. In these experiments, the acceleration distance was extended from mm scale to meter scales[42] and acceleration in a positron wake was also observed for the first time[43]. The first acceleration of electrons by more than one GeV was observed in a $\sim 10cm$ long plasma[44], and most recently, the energy of some of the electrons in a 42GeV beam was doubled in just 85 cm[2]! These experiments have demonstrated the dramatic increase in accelerating gradients by reducing the bunch length, thereby validating the $1/\sigma_z^2$ scaling of the wake.

The highest energy achieved in these experiments are plotted together with other plasma based acceleration results in Fig. 2.3 (from [31]). The progress which is quantified in units of energy gain per year is in sharp contrast with the leveling off of the Livingstone curve using conventional RF technologies [45].

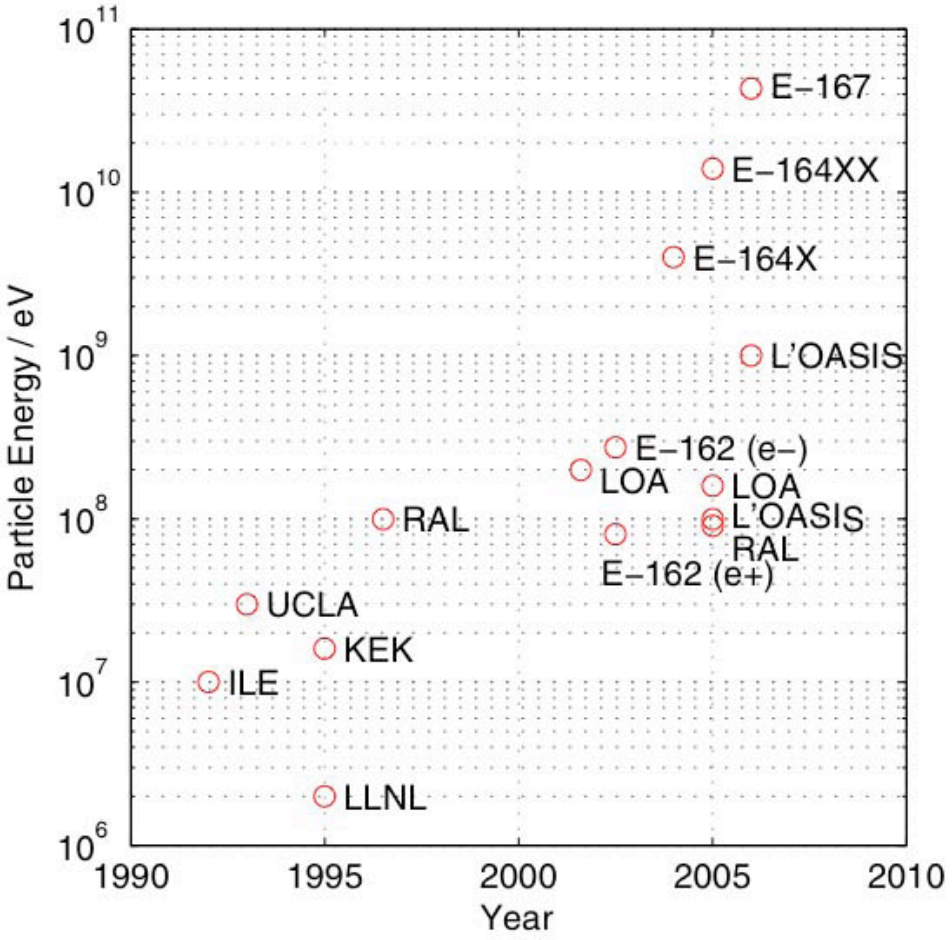

Figure 2.3: The maximum energy achieved by plasma based accelerator experiments is plotted versus time [31]

Not only did these experiments provide milestones in energy gain and acceleration length, they provided key and fundamental results in intense beam-plasma interactions. These results can be broken down into the following topics (i) electron transverse dynamics [46][42][47][26] (ii) positron acceleration and transverse dynamics[43][48][49] (iii) synchrotron radiation from betatron oscillation[50][51] (iv) field-ionization[53] and (v) electron trappping[54]. Each is briefly summarized hereafter.

The electron beam transverse dynamics could be studied by measuring variation of the beam spot sizes at the plasma exit as a function of plasma length. Alternatively it can be inferred by studying the variation of the exiting spot size under different plasma densities. Oscillations were observed when the beam and plasma are not matched (emittance spreading is not balanced by ion focusing)[46], and the damping of the oscillation was observed when the matching condition was approached[42]. Both of these observations agreed with envelope calculations under a linear focusing force as long as the density is low enough so that the wake is excited in the blow-out regime. The gradual formation of the ion channel from complete blowout (zero focusing to uniform ion focusing) was also observed by looking at different 'slices' of the spot sizes near the beam head[47]. In the most recent energy doubling experiment[2], a new phenomena – beam head erosion – is suggested by simulations to be the limiting factor for further energy gain[26]. This longitudinal erosion of the beam is caused by the transverse spreading of the beam head due to the lack of focusing and the resulting backward slippage of the ionization front.

Acceleration and transverse dynamics of positron beams inside a plasma were also explored in these experiments. The first positron acceleration was observed at an average rate of $\sim 56 MeV/m$ over a 1.4 meter long plasma[43]. A maximum

demagnification of the transverse spot size by a factor of two was demonstrated and the focusing force was observed to vary in a nonlinear fashion along the full $12ps$ length of the beam[48]. The halo formation around a positron beam core due to the slice emittance growth from the nonlinear focusing force was also observed in the experiments[49].

The betatron oscillation of the ultra-relativistic beam particles inside the plasma ion column generates synchrotron radiation strongly peaked in the forward direction. Although incoherent and broadband, the peak brightness of the x-ray beam is comparable to the undulator radiation at synchrotron light sources[50]. The absolute photon yield, the angular spread and the density dependence of the X-rays were measured[50]. These strong X-rays can be used to generate positrons in the energy range of $3-30MeV$ by colliding with a tungsten target[51].

The original idea of increasing the accelerating field by reducing the bunch length according to Eq.(2.1) has led the experiments into a whole new regime. When the bunch length of the electron beam at SLAC was reduced from a few hundred microns to tens of microns, the space charge field of the beam becomes large enough to field-ionize some of the neutral gases and produce the plasma by itself[52]. This resolves the problem of producing high-density long plasma sources using laser photo-ionization and is also free of timing and alignment issues. Extensive experiments has been carried out to test the ionization onset under different beam parameters using different types of gases[53]. Both the $3GeV$ energy gain results[44] and the most recent energy doubling experiments[2] were performed under this field-ionization regime.

A new phenomenon emerges when the gradients of the wakefields in these experiments exceeds $\sim 10GV/m$. An intense beam of self-trapped electrons is

observed under this condition. On the one hand, these trapped electrons are equivalent to the dark current of RF accelerators and can create unwanted, low energy particles and may also potentially load the plasma wake and therefore degrade the quality of the accelerated beam. However, on the other hand, these trapped electrons themselves have interesting properties such as multi-GeV energies, lower emittance than the drive beam and bunch lengths of only 10's of femoseconds. The physics of particle trapping by electrons born within the wakefield from field ionization in the 3D relativistic plasma waves is studied in [54], where the measured threshold wakefield for trapping ($\sim 30GV/m$) is found significantly below the theoretical prediction from [18] ($\sim 4TV/m$). This discrepancy was explained by the fact that the trapped electrons here come from the ionized Helium buffer gas, which were born inside the wake where the initial potential was low enough for trapping to happen significantly below the standard threshold.

2.4 Update on a future afterburner design

With the new knowledge and insights gained from the PWFA experiments, the design of a future afterburner based on the original idea[40] has consistently been reexamined and improved over the years. At the 2006 Advanced Accelerator Concepts (AAC) workshop, the latest design was discussed[55] and the major conclusions are listed below.

A multiple stage design was considered for an afterburner which accelerates 100 GeV particle beams to 500 GeV. In this design, a train of the drive bunches each at 100 GeV will be separated to independently drive each stage of the plasma accelerator. The witness beam will go through each stage gaining approximately 100 GeV in a few meters per stage. The ability to control head erosion and to limit the hosing instability are among obvious advantages to this approach. An

alternative approach that utilizes a single plasma accelerator stage with properly shaped drive beams that permit a high transformer ratio was also proposed. Simpler synchronization and transport lines were considered among the advantages of this approach.

The viability of these designs depends on several critical issues. Ion collapse is one of the concerns of the design for the International Linear Collider (ILC) parameters. The witness beam is so intense so that on its own it will cause the ions to collapse on the time scale of the beam passage[56]. This effect is also an issue of LWFA. Therefore, a simple extension of the SLAC experiment is not applicable. Using heavier ion species such as Argon[57], using hollow plasma channels and using a nonlinear matching section have been suggested as possible solutions. Ultimately, a combination of these ideas may be necessary. It was also pointed out that using the dictated parameters from ILC may not be the optimal linac-afterburner combination. A completely different set of consistent parameter set may be needed to optimize the performance.

Other critical issues including beam head erosion, hosing instabilities, positron acceleration, two bunch experiments (loading of the wake), etc. were identified or discussed at and since the 2006 AAC workshop. Some of these issues in the field-ionized regime will be addressed using simulations in the later chapters of this dissertation.

CHAPTER 3

Particle In Cell Codes for Modeling PWFA

In this chapter, the simulation tools for modeling PWFA will be introduced. First, a brief introduction will be given to particle in cell (PIC) codes in general. The properties of the most widely used fully explicit PIC codes will be discussed. Next, a novel quasi-static PIC code – QuickPIC which can efficiently model the afterburner stage of a PWFA will be introduced. Last, challenges and improvement required in QuickPIC will be pointed out.

3.1 Paritcle In Cell (PIC) simulations

As described in Chapter 1, in the non-linear regime of a PWFA, the plasma response to a particle/laser driver is nonlaminar and electron trajectory crossing occurs. Therefore a fluid description is no longer suitable and a kinetic or particle based model is needed. Moreover, in any plasma-based accelerator design, the trailing beam spot sizes required for matched beams and for efficient beam loading are extremely narrow, and the bulk plasma is "cold" while the average momentum is large. These facts make it difficult to directly solve the plasma kinetic equations or fluid equations, where the phase space is treated as continuum. It therefore seems naturally follows that a particle-based model is required.

The idea of studying plasma physics by using a computer to follow charged particles starts in the late 50's and early 60's. The breakthrough was developing

the concepts of finite size particles so that simulations using few numbers of simulation particles reproduced properties of real plasmas with orders of magnitude more particles. Since even with the fastest computer available, it is impossible to follow every real particle because of the huge number of them in typical problems, super-particles (or macro-particles) are used. Each super-particle has the same charge to mass ratio as a real particle while its mass (and charge) can be many orders of magnitude larger, e.g. 10^4. The trajectories of the super-particles are the same as those of the real particles because they depend on the charge to mass ratio and not the mass nor the charge separately. This is the main reason why super-particles can be used.

However, the justification of using fewer but more massive particles to model a real plasma is not trivial. Actually, while some quantities, such as the plasma frequency, remain the same, some other quantities, such as the collision frequency, may change. This can be seen by writing out the ratio of these quantities between super-particles and real electrons while $\frac{n_e}{n_s} = \frac{m_s}{m_e} = \frac{q_s}{q_e}$ ('s' stands for super-particle). For example, the plasma frequency remains unchanged,

$$\frac{\omega_{ps}}{\omega_{pe}} = \sqrt{\frac{n_s q_s^2 m_e}{n_e q_e^2 m_s}} = 1 \tag{3.1}$$

On the other hand, electron-ion collision frequency $\nu_{ei} = ln\Lambda \cdot nq^4/16\pi\epsilon_0^2 m^2 v^3$[58] scales roughly with the particle mass.

$$\frac{\nu_{ies}}{\nu_{ie}} = \frac{n_s}{n_e}\frac{q_s^4}{q_e^4}\frac{m_e^2}{m_s^2}\frac{ln\Lambda_s}{ln\Lambda_e} = \frac{m_s}{m_e}\frac{ln\Lambda_s}{ln\Lambda_e} \simeq \frac{m_s}{m_e}, \tag{3.2}$$

where $\Lambda = \overline{\lambda_D/r_0}$ and $r_0 = q^2/4\pi\epsilon_0 m v^2$. Note that $v_e = v_s$ since the trajectories are unchanged. Therefore, the collisional frequency is increased by using super particles unless the interaction at close distances is modified. This effect can be reduced by using finite size particles where the particles are described as clouds instead of points[59]. In this way, the force between two particles goes to zero

instead of infinity when the distance between them goes to zero, leading to less collisional effects. If a particle size is roughly a Debye length, then much of the kinetic behavior can be modeled using a smaller number of finite size particles. More discussion of validity of using super-particles can be found in Chapter 1 of [22]. "The point is", as stated in the book, "within all three branches of plasma study (experiment, theory, computation), practitioners must exercise a great deal of care, enough to obtain the essence of the problem, but not so much as to inhibit achieving any result. "

Other important effects in PIC codes include the possible numerical instabilities associated with the utilization of discrete spatial grids and finite time steps. These phenomena are related to spatial aliasing and time aliasing, respectively[59]. For the case of a discrete spatial grid, since the coordinates of particles are given exactly (have continuous values), their density has much shorter wavelength components than those of the field quantities which are defined only on grids. The spatial aliasing may cause these short wavelength density perturbations to resonate with longer wavelength higher phase velocity E field waves (both longitudinal and transverse), leading to unphysical instability or damping. Besides the use of finite size particles to avoid these effects, it is sometimes beneficial to use higher order weighting schemes (fatter particles) and smoothing or filtering algorithms. Similarly, the time aliasing can cause unphysical resonance by converting high-frequency high phase velocity waves into low-frequency low phase velocity ones due to undersampling. The way out of this problem is to choose time steps shorter compared to the minimum period of oscillation supported by the system. In full PIC code, this leads to the Courant condition.

Compared to other codes (e.g. Vlasov code and MHD code), PIC codes make the fewest approximation. However, this means it is also most computationally

intensive among these codes.

3.2 Full PIC codes

Depending on the field equations a PIC code is based on, it can be classified as a fully explicit PIC code or a reduced PIC code. In a fully explicit PIC code, the full set of Maxwell's equations are solved with 'no' approximation (other than the use of a grid), therefore a full PIC code includes all possible electromagnetic modes. If approximations are made to the Maxwell's equations, it becomes a reduced PIC code. Most commonly used reduced PIC codes include the electro-static codes ($\nabla \times \mathbf{E} = 0$ in Maxwell's equations)[22], Darwin codes ($\frac{\partial \mathbf{E_{sol}}}{\partial t} = 0$ in Maxwell's equations, where E_{sol} is the divergence free part of the electric field)[22], and the quasi-static codes (details will be discussed in the next section). For PWFA research, electromagnetic full PIC codes were the most extensively used. Detailed discussion of this full PIC algorithm can be found in [22]. Some properties of this algorithm will be highlighted hereafter.

In a full PIC code, the field equations and particle push equations are discretized in a time centered manner, so that they can be advanced using the leapfrog method. This time-centered property of the equations removes the requirement of an iteration loop and yields minimal error. Here, 'the field equations' refers to Faraday's law and Ampere's law from Maxwell's equations because the other two (Gauss's law and $\nabla \cdot B = 0$) are automatically satisfied as long as they are true at the initial time step (which is straightforward to ensure) and the continuity equation is rigorously satisfied at each time step (this is nontrivial and needs careful consideration). The 'particle push equations' here refers to equations of motion $\frac{d\mathbf{p}}{dt} = \mathbf{F}$ and $\frac{d\mathbf{r}}{dt} = \mathbf{v}$.

In space, the field and density quantities are staggered on the so-called Yee mesh so that centered spacial differencing can be used. In a warm plasma, the grid size should be able to resolve the debye length so that the collective behavior of the plasma can be preserved. However, when a plasma is cold (e.g. in the PWFA case), only the plasma skin depth (c/ω_p) is needed to be resolved.

In each computational cycle, the charge and current densities are deposited at the grids; the electric and magnetic fields are then solved; these fields are interpolated at the particles positions; and the particle positions and velocities are updated based on these fields. This cycle then continues for the desired number of time steps.

When space and time are discretized in the way described above, the resulting numerical dispersion relation of an electromagnetic wave can differ from the continuous space and time result. In order to avoid unphysical damping or growth from complex ω's and to avoid numerical error from the dispersion relation, restrictions on $\Delta t/\Delta x$ are present for stability reasons (the Courant condition). For example, $\Delta t/\Delta x < 1/c$ needs to be satisfied for a 1D electromagnetic wave in vacuum. However, when the field equations are solved using finite difference time domain rather than with FFT's, all allowed choices of $\Delta t/\Delta x$ yield a slower phase velocity of the electromagnetic wave from the true dispersion relation. As an example, Fig. 3.1 shows the numerical dispersion relation of a 1D electromagnetic wave in vacuum for different choices of $\Delta t/\Delta x$ while the real dispersion relation is $\omega = kc$. Similar restrictions (the Courant condition) also apply in a plasma for 2D and 3D electromagnetic waves. .

The Courant condition has two important implications. First, it implies that the maximum time step Δt that can be chosen is restricted by the grid size Δx, which has to be small enough to resolve the smallest wavelength in a specific

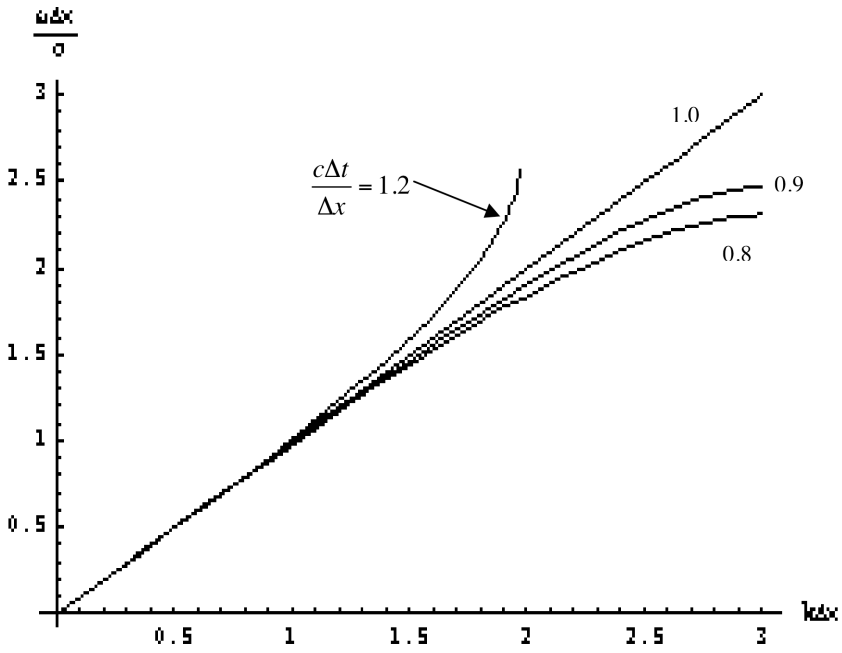

Figure 3.1: Numerical dispersion relation of a 1D electromagnetic wave in vacuum for different choices of $\Delta t/\Delta x$

problem. This sets up a lower limit to the number of time steps needed in a simulation which models a fixed amount of physical time and therefore full PIC codes are generally very computationally intensive. For example, to model a $1GeV$ stage of a PWFA, 10^{13} pushes are required and that will take about 10,000 CPU hours on a typical CPU of today[60]. The second implication is the spurious Cerenkov radiation. For choices of time step and grid sizes that satisfy the Courant condition, the phase velocity of electromagnetic waves can be numerically slowed down below c (speed of light in vacuum). Therefore when there are relativistic particles present (which is the case in PWFA), they can travel faster than this unphysically "slow" light wave, thereby producing unphysical Cerenkov radiation. Since the numerical speed of this light wave is slower for short wavelengths, the radiation normally has high frequency. This high frequency "noise" may couple back to the particles, interfering with real physics. In order

to suppress the growth of this radiation, time or spacial filtering of the high frequency or short wavelength components can be applied. However, caution should be used since they may introduce new non-physical results.

In the next section, we will introduce a 3D electromagnetic PIC code – QuickPIC. It is a reduced PIC code based on the quasi-static approximation. QuickPIC uses its own advancing scheme, therefore it is not subject to the Courant condition and the unphysical Cerenkov radiation as the full PIC codes. Of course, it also has its own limitations.

3.3 The quasi-static PIC code – QuickPIC

QuickPIC is a highly efficient code capable of modeling the afterburner stages of a PWFA based on the quasi-static approximation[24]. The physical picture of this approximation is interpreted in section 3.2.1. Other properties of the code are discussed in detail in [1], the essence of which will be summarized/reinterpreted in the following sections.

3.3.1 Quasi-static approximation

In plasma based acceleration problems, the driver (particle beam or laser pulse) travels at a speed near c. For quantities of interest, such as the electric and magnetic fields around the beam, it is more convenient to use a new set of coordinates (x, y, ξ, s) than the original set (x, y, z, t), where $\xi = ct - z$ and $s = z$. The relationship between these 2 coordinate sets is illustrated in Fig. 3.2. We can see that s is basically the distance that the driver has traveled into the plasma (since the field point that we are interested in is always near the beam) and ξ is a measure of the longitudinal distance from this field point to the moving window

center which travels at c and is near the beam center. It's worth noting that this coordinate transformation is merely a mathematical one, not one that changes the physical frame, i.e., a Lorentz transformation.

The mathematical form of the quasi-static approximation is $\frac{\partial}{\partial s} \ll \frac{\partial}{\partial \xi}$. From Fig. 3.2 we can see, this essentially means that the quantities at A are much more similar to those at A' than those at B, where A and A' have the same ξ but different s while A and B have the same s but different ξ. This is true when the driver evolves over distances much longer than the bunch length or the plasma wavelength. For a certain distance Δs which could involve many plasma oscillations, the beam may not evolve. So the fields around it will remain the same during this Δs. For this reason, the quasi-static approximation is also called the 'frozen-field' approximation. As stated in Chapter 1, since the driver in plasma based accelerators are usually very 'stiff' (γ for beam drivers up to 10^5), and evolves at a much larger scale ($\sim$ the betatron wavelength $\lambda_\beta = \frac{c}{\sqrt{2\gamma}\omega_p}$) than the scale of variation of the fields around the beam ($\sim$ the plasma wavelength $\lambda_p = 2\pi\frac{c}{\omega_p}$), the quasi-static approximation is a good description of the system.

The application of the quasi-static approximation leads to two major characteristics of the algorithm. First, it simplifies the Maxwell's equations so that the fields can be solved locally in 2D. Second, it allows large time steps to be taken when updating the beam. The former one gives time saving in the sense that for a specific s where the beam has a certain shape, the fields around it are solved much faster by solving 2d equations, while the latter one gives time saving in the sense that for a certain distance Δs, the number of time steps taken can be minimized to resolve only the beam betatron oscillation instead of the plasma oscillation.

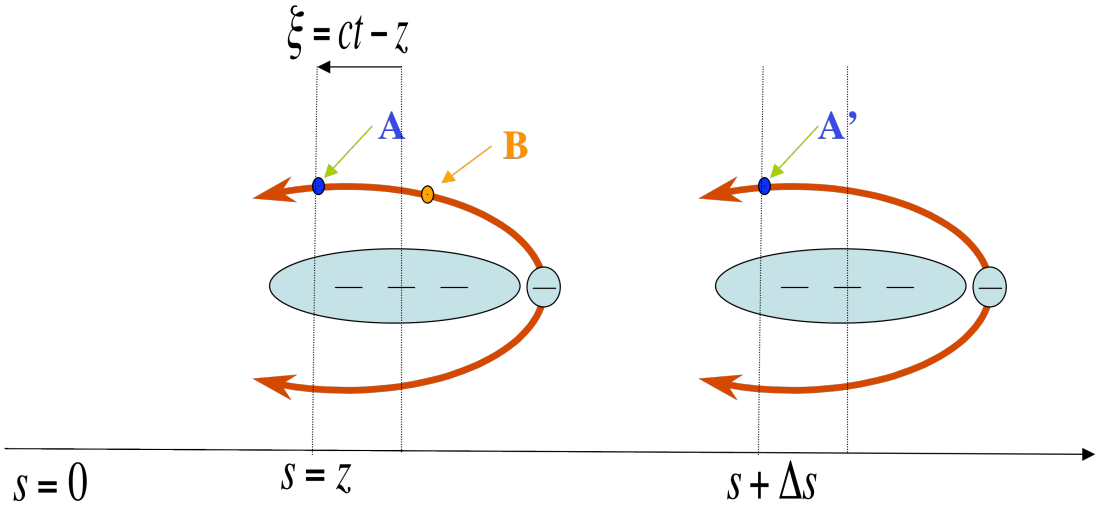

Figure 3.2: Schematic of the quasi-static approximation

3.3.2 Basic equations under the quasi-static approximation

In this section we will show how the full 3D Maxwell's equations reduce to 2D equations under the quasi-static approximation for a specific choice of gauge. Appropriate particle pusher equations are also obtained.

Maxwell's equations in the Lorentz gauge are

$$(\frac{1}{c^2}\frac{\partial^2}{\partial t^2} - \nabla^2)\mathbf{A} = \frac{4\pi}{c}\mathbf{j} \tag{3.3}$$

$$(\frac{1}{c^2}\frac{\partial^2}{\partial t^2} - \nabla^2)\phi = 4\pi\rho \tag{3.4}$$

while the Lorentz gauge condition is

$$\nabla \cdot \mathbf{A} = -\frac{1}{c}\frac{\partial \phi}{\partial t} \tag{3.5}$$

The position and velocity of plasma electrons (and ions if necessary) are updated by

$$\frac{d\mathbf{P}_{e,i}}{dt} = q_{e,i}(\mathbf{E} + \frac{1}{c}\mathbf{v}_{e,i} \times \mathbf{B}) \tag{3.6}$$

$$\frac{d\mathbf{X}_{e,i}}{dt} = \mathbf{v}_{e,i} \tag{3.7}$$

In most cases the ions are kept stationary as a uniform background. Beam particles are updated similarly by

$$\frac{d\mathbf{P}_b}{dt} = q_b(\mathbf{E} + \frac{1}{c}\mathbf{v}_b \times \mathbf{B}) \tag{3.8}$$

$$\frac{d\mathbf{X}_b}{dt} = \mathbf{v}_b \tag{3.9}$$

Now, we approximate Maxwell's equations (corresponding to (3.3) and (3.4)) under the quasi-static approximation. In order to do this, we change to the (x, y, ξ, s) coordinates. For field quantities where ξ and s are separate parameters, the partial derivatives in (x, y, z, t) and those in (x, y, ξ, s) are related by

$$\frac{\partial}{\partial t} = c\frac{\partial}{\partial \xi} \tag{3.10}$$

$$\frac{\partial^2}{\partial t^2} = c^2\frac{\partial^2}{\partial \xi^2} \tag{3.11}$$

$$\frac{\partial}{\partial z} = -\frac{\partial}{\partial \xi} + \frac{\partial}{\partial s} \tag{3.12}$$

$$\nabla^2 = \frac{\partial^2}{\partial x^2} + \frac{\partial^2}{\partial y^2} + \frac{\partial^2}{\partial z^2} = \frac{\partial^2}{\partial x^2} + \frac{\partial^2}{\partial y^2} + (-\frac{\partial}{\partial \xi} + \frac{\partial}{\partial s})^2 \tag{3.13}$$

Applying the quasi-static approximation $\frac{\partial}{\partial s} \ll \frac{\partial}{\partial \xi}$ into (3.12) and (3.13), we have

$$\frac{\partial}{\partial z} \approx -\frac{\partial}{\partial \xi} \tag{3.14}$$

$$\nabla^2 \approx \frac{\partial^2}{\partial x^2} + \frac{\partial^2}{\partial y^2} + \frac{\partial^2}{\partial \xi^2} \tag{3.15}$$

Using (3.11) and (3.15) in (3.3) and (3.4), we obtain

$$-\nabla_\perp^2 \mathbf{A}(x, y, \xi, s) \approx \frac{4\pi}{c}\mathbf{j}(x, y, \xi, s) \tag{3.16}$$

$$-\nabla_\perp^2 \phi(x, y, \xi, s) \approx 4\pi\rho(x, y, \xi, s) \tag{3.17}$$

Noticing that the second order time derivative, $\frac{\partial^2}{\partial t^2}$, and longitudinal derivative $\frac{\partial^2}{\partial z^2}$ terms in (3.3) and (3.4) have been canceled due to the quasi-static approximation.

At the same time, by using (3.10) and (3.14), the gauge condition (3.5) becomes

$$\nabla_\perp \cdot \mathbf{A}_\perp \approx -\frac{\partial}{\partial \xi}(\phi - A_z) = -\frac{\partial}{\partial \xi}\psi \tag{3.18}$$

where the pseudo-potential ψ is defined as

$$\psi \equiv \phi - A_z \tag{3.19}$$

In order to derive the equations of motion which best exploit the quasi-static equations, we must first choose a coordinate system. Usually, the trajectory of a particle is described as a curve in a 3D space (x, y, z) with time used as the parameterization of this curve, $x(t)$, $y(t)$, $z(t)$. As described previously, the field equations are simplified if we make a mathematical transformation to the set of variables x, y, $\xi \equiv ct - z$, $s \equiv z$. The trajectory of a plasma particle is defined as a curve in x, y, s space with ξ now playing the role of time. The time derivative $\frac{d}{dt}$ is now $(1 - \frac{v_z}{c})\frac{d}{d(\xi/c)}$ since $d\xi = dct - dz = c(1 - \frac{v_z}{c})dt$. The equations of motion are now

$$\frac{d\mathbf{p}_e}{d(\xi/c)} = \frac{1}{1 - v_{ez}/c}\mathbf{F}(x(\xi), y(\xi), s(\xi); \xi) \tag{3.20}$$

where $\mathbf{F} = q_e(\mathbf{E} + \frac{1}{c}\mathbf{v}_e \times \mathbf{B})$

$$\frac{dx_e}{d(\xi/c)} = \frac{p_{ex}}{m\gamma(1 - v_{ez}/c)} \tag{3.21}$$

$$\frac{dy_e}{d(\xi/c)} = \frac{p_{ey}}{m\gamma(1 - v_{ez}/c)} \tag{3.22}$$

$$\frac{ds_e}{d(\xi/c)} = \frac{v_{ez}}{1 - v_{ez}/c} \tag{3.23}$$

The quasi-static assumption implies that $\frac{\partial \mathbf{F}}{\partial s} \approx 0$. Therefore, as we will discuss shortly, it is not necessary to calculate the $s(\xi)$ part of the trajectory. Note

that s is different for each particle for a specific ξ, but under the quasi-static approximation, the trajectories in x and y depend very weakly on s.

For a beam particle which is moving near the speed of light in the z direction, we use the propagation distance of the moving window $s_w \equiv ct$ as the time like variable. The equations of motion are changed little except now we need an equation for ξ. The differential $\frac{d}{dt}$ is now $\frac{d}{d(s_w/c)}$, so

$$\frac{d\mathbf{p}_b}{ds_w} = \frac{1}{c}\mathbf{F}(x(s), y(s), \xi(s); s) \tag{3.24}$$

$$\frac{dx_b}{ds_w} = \frac{p_{bx}}{\gamma mc} \tag{3.25}$$

$$\frac{dy_b}{ds_w} = \frac{p_{by}}{\gamma mc} \tag{3.26}$$

$$\frac{d\xi_b}{ds_w} = 1 - \frac{p_{bz}}{\gamma mc} \tag{3.27}$$

To summarize, we have obtained a reduced set of Maxwell's equations (3.16) (3.17) and the correponding gauge condition (3.18) under the quasi-static approximation. The equations of motion for plasma electrons (3.20)–(3.23), and for beam particles (3.24)–(3.27), are also obtained. The transverse derivative operators in the reduced Maxwell's equations (3.16) (3.17) indicate that these equations can be solved locally in 2D, given the source term $\mathbf{j}$ or ρ as well as the boundary condition on this 2D slice. The beam particles are updated in s_w while the plasma particles are updated with ξ acting as the time-like variable.

3.3.3 QuickPIC code structure

Based on the equations in last section and also within the spirit of the disparity of the time-scale for he evolution between the beam and the plasma, QuickPIC was designed with the unique structure shown in Fig. 3.3.

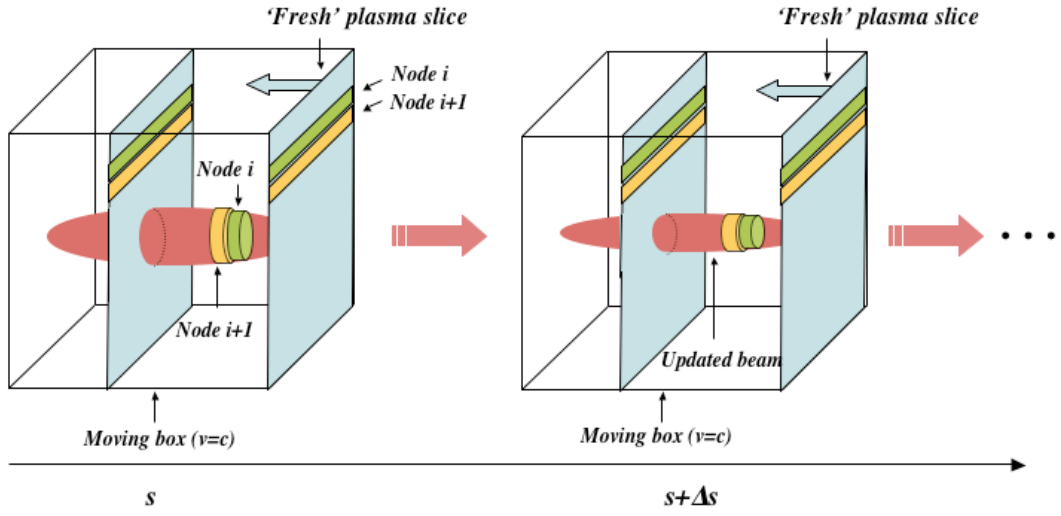

Figure 3.3: Schematic of QuickPIC code structure

At the beginning of the simulation, the 3D beam is initialized with particles on a (x, y, ξ) grid with appropriate momenta at a fixed s. A 'fresh' 2D slice of plasma particles is then swept through the beam (by advancing in ξ) in the moving window where the beam is kept stationary, and the value of s is assumed to be the same for each plasma particle. This corresponds to the process of the beam running into a 'fresh' slice of plasma at a fixed s in a stationary frame. Using a 'fresh' plasma slice is justified by noticing that the beam moves at $v_{bz} \approx c$, so any plasma in front of it is always unperturbed.

The flow chart of QuickPIC is shown in Fig. 3.4. It is a combination of a parallelized 2D code (for the plasma particles) embedded in a parallelized 3D code (for the beam particles). The 3D code contains the beam particles and uses the 2D code as a transverse field solver at each slice. The 3D code passes the beam density as the input to the 2D code and obtains the electric and magnetic fields as the output from the 2D code. The 3D part is distributed to different processors along ξ while the 2D part is distributed along y as shown in Fig. 3.3.

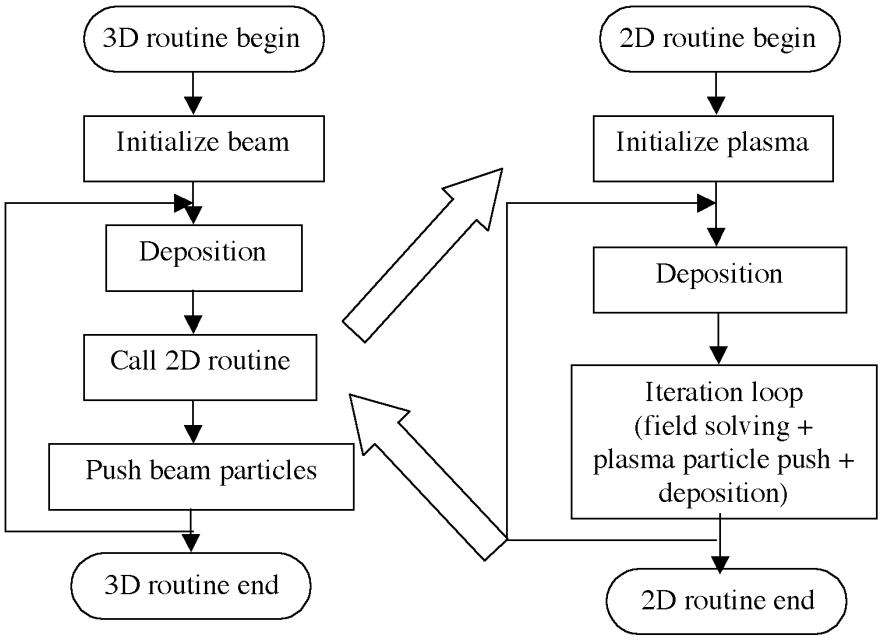

Figure 3.4: QuickPIC flow chart

3.3.4 Implementation of the quasi-static equations in QuickPIC

The basic set of equations described in section 3.3.2 only gives the essential physics of the quasi-static approximation. The practical implementation of this approximation into a code involves many more detailed considerations. These details are discussed in [1] and [60], the highlights of which will be summarized in this section. We have separated these considerations into six topics: (i) The continuity equation, (ii) Charge and current deposition, (iii) Particle push, (iv) Predictor-corrector loop, (v) Diffusion coefficient, and (vi) Boundary conditions.

(i) Continuity equation: Similar to full PIC codes, the continuity equation needs to be satisfied in order to guarantee the self-consistency of the code. Using (3.16) – (3.19), the continuity equation under the quasi-static approximation takes the form

$$\frac{\partial(c\rho - j_z)}{\partial \xi} + \nabla_\perp \cdot \mathbf{j}_\perp = 0 \tag{3.28}$$

This needs to be satisfied by the charge and current densities from both the plasma and beam particles. Note that if one integrates over all space in a 2D slice, $\int d\mathbf{x}_\perp (c\rho - j_z)$ is conserved. Therefore, the total charge, $\int d\mathbf{x}_\perp \rho$ is not conserved. Physically, this is due to the fact that particles can move between slices if they have a finite axial velocity. If the number of PIC particles remains fixed within the 2D slice, then charge will be conserved unless the charge per particle varies. In what immediately follows, we describe how to deposit the charge and current such that $\int d\mathbf{x}_\perp (c\rho - j_z)$ is conserved.

(ii) Charge and current deposition: The charge density from the beam particle is deposited in the same way as the normal deposition in a full PIC code. However, in order to satisfy (3.28), the current density from the beam is deposited according to $j_{bz} \approx c\rho_b$ and $\mathbf{j_b}_\perp \approx 0$. When depositing plasma particles, the time that a particle stays inside a certain slice of ξ needs to be taken into account. This time contribution can be measured by

$$\frac{ds_w}{d\xi_e} = \frac{1}{1 - v_{ez}/c} \tag{3.29}$$

Therefore the charge and current density contribution from plasma particles can be written as

$$\rho_e = \frac{1}{Volume} \sum_i \frac{q_{ei}}{1 - v_{eiz}/c} \tag{3.30}$$

$$\mathbf{j}_e = \frac{1}{Volume} \sum_i \frac{q_{ei}\mathbf{v}_{ei}}{1 - v_{eiz}/c}. \tag{3.31}$$

This deposition scheme for the plasma particles also satisfies the continuity equation (3.28).

(iii) Particle push: Because it is challenging to advance a beam particle using (3.24) directly, simplified forms are used by assuming $\mathbf{v_b} \approx c\hat{z}$. Essentially, this is

reasonable if the self-forces of the beam, which scale as $\frac{1}{\gamma_b^2}$, can be neglected. Under this assumption, the electric fields can be expressed using the psedo-potential ψ.

$$\frac{d\mathbf{p_{b\perp}}}{ds_w} = \frac{q_b}{c}\mathbf{E_{focusing}} \approx -\frac{q_b}{c}\nabla_\perp \psi \tag{3.32}$$

$$\frac{dp_{bz}}{ds_w} \approx \frac{q_b}{c}E_z \approx \frac{q_b}{c}\frac{\partial \psi}{\partial \xi} \tag{3.33}$$

These are used together with (3.25) – (3.27) to advance the beam particles. When advancing the plasma particles, the transverse coordinates and transverse momenta can be updated in ξ using (3.21), (3.22) and the transverse component of (3.20). In reality, in order to simplify the calculation, these fully relativistic equations are cast into the form of a non-relativistic Boris pusher with a modified electric field and an effective charge

$$\frac{d\mathbf{u}_{p\perp}}{d\xi} = \frac{q_{eff}}{m}[\gamma \mathbf{E}_\perp + (\frac{\mathbf{u}_p}{c} \times \mathbf{B})_\perp] \tag{3.34}$$

$$\frac{d\mathbf{x}_{p\perp}}{d\xi} = \frac{\mathbf{u}_{p\perp}}{1 - q_e\psi/mc^2} \tag{3.35}$$

where the effective charge is defined as

$$q_{eff} \equiv \frac{q_e}{1 - q_e\psi/mc^2} \tag{3.36}$$

and $\mathbf{u} = \gamma\mathbf{v}$ is the proper velocity. For the longitudinal part, since we are not interested in s_e as a function of ξ, we do not keep track of s_e. Moreover, the longitudinal velocity $v_z(\xi)$ is not updated directly. Instead, it is calculated based on the transverse momentum and the pseudo-potential using

$$\widetilde{p}_z \approx \frac{1 + \widetilde{p}_\perp^2 - (1+\widetilde{\psi})^2}{2(1+\widetilde{\psi})} \tag{3.37}$$

$$\gamma \approx \frac{1 + \widetilde{p}_\perp^2 + (1+\widetilde{\psi})^2}{2(1+\widetilde{\psi})}. \tag{3.38}$$

where $\widetilde{p} = \frac{p}{mc}$ and $\widetilde{\psi} = \frac{\psi}{mc^2/e}$ are normalized momentum and normalized pseudo-potential, respectively. (3.37) and (3.38) are obtained through a quantity, $\gamma - \widetilde{p_z} - \widetilde{\psi} \approx 1$, that is conserved under the quasi-static approximation[24].(For the reader's convenience, the derivation of this conserved quantity as well as 3.37 and 3.38 are reproduced from [61] in appendix A.)

(iv) Predictor-corrector loop: In the 2D part of QuickPIC, the velocity and positions of the plasma particles need to be advanced in ξ according to (3.34) and (3.35). However, due to the instantaneous nature (i.e. the lack of $\frac{\partial}{\partial \xi}$ term) of the field equations (3.16) and (3.17), it is not possible to advance this system using the explicit leap-frog scheme. Instead, an implicit predictor-corrector loop is used. How the quantities are predicted and corrected during the iteration is explained in [1] in detail, and the basic idea is given hereafter. Assume the velocity is known at the integer step m of ξ and the position is known at the half integer step $(m + 1/2)$. In order to advance the velocity to the next integer step $(m + 1)$, the fields need to be known at $(m + 1/2)$. The fields are related to the scalar and vector potentials through

$$\mathbf{E}_\perp = -\nabla_\perp \phi - \mathbf{A}_{\perp\xi}, \tag{3.39}$$

$$E_z = \frac{\partial}{\partial \xi}\psi, \tag{3.40}$$

$$\mathbf{B}_\perp = (\mathbf{A}_{\perp\xi} + \nabla_\perp A_z) \times \hat{z}, \tag{3.41}$$

$$B_z = \nabla_\perp \cdot (\mathbf{A}_\perp \times \hat{z}), \tag{3.42}$$

while ϕ and $\mathbf{A}$ can be obtained from charge and current densities instantaneously through (3.16) and (3.17). Therefore, if predictions are made for ρ, $\mathbf{j}_\perp$ as well as $\mathbf{j}_{\perp\xi}$ at $(m + 1/2)$, the fields will be known at $(m + 1/2)$, which can be used to calculate the velocity at $(m + 1)$. This calculated velocity is then used to make a correction to the predicted ρ, $\mathbf{j}_\perp$ and $\mathbf{j}_{\perp\xi}$ values at $(m + 1/2)$. A new value of

the velocity at $(m+1)$ will then be calculated based on these new predictions. This predictor-corrector process can be iterated to minimize the errors. After an accurate enough velocity is obtained at $(m+1)$, the position at $(m+1/2)$ can be advanced to the next step at $(m+3/2)$. This iterative process completes one cycle in the 2D advancing scheme.

(v) Diffusion coefficient: The predictor-corrector loop described above suffers from one kind of numerical instability similar to one that occurs in Darwin codes. The low $k_\perp$ modes of $\mathbf{A}_{\perp\xi}$ are the most unstable, they grow rapidly and soon dominate the fields and forces in a few iterations. This is due to the instantaneous nature of the elliptical equations (3.16) and (3.17). In order to avoid this instability in QuickPIC, these poisson like equations are modified into parabolic diffusion equations which have a finite response time,

$$D_j^{-1}\frac{\partial}{\partial T}\mathbf{A}_{\perp\xi} = \nabla_\perp^2\mathbf{A}_{\perp\xi} + \frac{4\pi}{c}\mathbf{j}_{\perp\xi} \tag{3.43}$$

$$D_\rho^{-1}\frac{\partial}{\partial T}\phi = \nabla_\perp^2\phi + 4\pi\rho \tag{3.44}$$

Here the diffusion terms act as high-pass filters in the k space of the potentials and damp out the unstable low k modes[62]. The proper choice of the diffusion coefficient and the number of iterations influence the accuracy and efficiency of this algorithm. Through experimentation, it has been found that $D_j = D_\rho = (c/\omega_p)^2$[63] and 2 iteration steps gives rapid convergence to accurate enough results (compared to full PIC code) in a large parameter range. QuickPIC solves for these diffusion equations (3.43) and (3.44) in Fourier space using the FFT routines. These routines involve transposing large amounts of data and are currently the most time-consuming part in QuickPIC.

(vi) Boundary conditions: When solving for fields using (3.43) and (3.44) (in Fourier space), the code supports both periodic and conducting boundary

conditions. All simulations presented in this dissertation were performed using the conducting boundary condition.The simulation box is a square for the 2D slice. The actual plasma is not contained in a square conductor. However, if the boundaries are far away compared to the blowout radius then the conducting boundaries are very appropriate since the **E** and **B** fields will be shielded away beyond a few plasma skin depth c/ω_p of the blowout radius. In these simulations, the beam particles have an open boundary condition where the ones going out of the simulation box transversely will be eliminated. The plasma particles have a reflecting boundary condition in the transverse direction although in most cases, the simulation window is chosen to be wide enough so that there are minimal numbers of reflected plasma electrons and their influence is therefore negligible.

3.3.5 QuickPIC framework and parallelization

QuickPIC is built from the UCLA Parallel Particle-in-Cell (UPIC) Framework [64]. This Framework provides trusted components for the rapid construction of new, parallel PIC codes, using object-oriented ideas. It is designed in layers. Each layer contains several types of classes and several operations (subroutines) on the objects of these classes. The bottom layer consists of general supporting classes such as the error class, the parallel class etc., which are written in Fortran77 and are highly optimized. Normally, classes in this layer do not need to be changed. The upper layer consists of high level physical classes such as the 'species2d' class, which describes a group of 2d particles of the same species (e.g. the plasma electrons in the 2d slice in QuickPIC). The operations on these class objects normally include generating and deleting an object and other typical manipulations (e.g. deposition and particle push for 'species2d' objects). The middle layer provides helper classes for the upper layer objects, for example, the

middle level class 'part2d' describes the properties of a specific particle species (e.g. charge, mass, etc.) and is a component of the 'species2d' class. Both upper and middle layers are written in Fortran95 and may need modifications to meet the requirement of a specific problem.

As has been mentioned in the previous section, QuickPIC currently decomposes the 3D domain in the longitudinal direction and the 2D domain in the y direction. Most parallel operations are processed in the bottom layer of the Framework and are normally hidden from the upper layer. However, some concepts, for example guard cells (which deal with processor boundaries) and the particle manager (which moves particle to the correct domain), have to be understood in order to safely modify the upper level codes. When a code is parallelized, the ideal time saving scales with the number of decomposition domains. However, in reality the network communication overhead limits this savings. During much of this research period, it has been found [60] that QuickPIC scales up to 32 processors on 'Seaborg' (a 6,656 processor IBM SP cluster at the National Energy Research Scientific Computer Center) and up to 16 processors on 'Dawson' (a 512 processor Mac G5 cluster at UCLA). All simulations presented in this dissertation are performed on these two clusters using these optimal number of processors. Recently, significant improvements have been made such that QuickPIC now scales to over 1000 processors.

In the previous sections, properties of the full PIC codes and the quasi-static QuickPIC were discussed. By utilizing the quasi-static approximation, QuickPIC can lead to time savings of $100 \sim 1000$ times compared to full PIC codes when modeling afterburner relevant PWFAs[60]. However, as described in chapter 2, new physics (such as field-ionization) arise and they are not included in the original QuickPIC model. In the next chapter, we will describe the implementation

of several of these models into QuickPIC, and some of their applications will be shown in the later chapters.

CHAPTER 4

Adding Realism into QuickPIC

In order to model the afterburner relevant experiments, several improvements were made to QuickPIC. These include the addition of a field-ionization package, modeling the radiation reaction force, and implementing realistic beam/plasma parameters. They will be described in detail in this chapter. A preliminary model that attempts to handle self-trapped particles, as well as its implementation in QuickPIC will be described at the end of this chapter.

4.1 Modeling field-ionization

In this section, the field ionization package will be described. First, the theoretical field ionization model – the ADK model[65] will be introduced. Then the modifications to QuickPIC will be described, followed by the benchmark of the wake fields against those from full PIC simulations with an ADK model.

4.1.1 Ionization rate and the ADK model

When neutral atoms or ions are exposed to an external electric field, their valence electrons may escape if the field is strong enough. Ionization can happen in either the multi-photon ionization regime or the tunneling ionization regime depending on the frequency and strength of the external electric field. The tran-

sition between these two regimes is determined by the Keldysh parameter[66] $\gamma = (\frac{|\varepsilon_0|}{2U_p})^{1/2}$, where ε_0 is the ionization energy and $U_p = E^2/(4\omega^2)$ is the ponderamotive potential, and ω is the frequency of the electric field. Multi-photon ionization happens when $\gamma \gg 1$ (high frequency electric field), while tunneling ionization happens when $\gamma \ll 1$ (low frequency electric field). Tunneling ionization got its name because of the electron's ability to tunnel through the potential barrier due to quantum effects. When the frequency is low, the electron can tunnel through the modified potential barrier within a single laser cycle. In PWFA, the external electric field is mainly from the space charge field of the particle beam which changes on a time scale of the σ_z/c where σ_z is the bunch length. Furthermore, the electric field does not oscillate, therefore, in the beam driven PWFA case, ionization does not occur in the multi-photon like regime.

Up till now, we have used the term 'tunneling ionization' in its generalized sense, referring to all ionization happening when $\gamma \ll 1$. In fact, when the low frequency external electric field is stronger than a critical value $E_{crit} = (\sqrt{2}-1)\varepsilon_0^{3/2}$, the barrier in the potential disappears and the electrons can escape "classically". This regime is called the Barrier Suppression Ionization (BSI) regime[66]. Values of E_{crit} for several types of gases from [67] are reproduced in Fig. 4.1. Since the beam space charge field can exceed $100GV/m \sim 1TV/m$ if its spot size is small enough (see next section), it is possible to access the BSI regime for several types of potential gases in PWFA experiments such as Li, Cs and H.

When ionization happens, the generated plasma density $n_p(t)$ is determined by

$$\frac{dn_p(t)}{dt} = w(t)(n_0 - n_p(t)) \tag{4.1}$$

where $w(t)$ is the ionization rate and n_0 is the initial neutral density.

From the above discussion, in order to properly model field ionization in

Atom/ion	ξ_i (eV)	Z	n^*	E_{crit} (GV/m)
H	13.6	1	1.00	75.3
He	24.5	1	0.746	182.
He+	54.4	2	1.00	602.
Li	5.39	1	1.59	18.7
Li+	75.5	2	0.848	985.
Cs	3.89	1	1.87	11.5
Cs+	25.1	2	1.47	189.

Figure 4.1: Critical Electric field of several types of gases [67]

PWFA, we need an ionization rate formula suitable for the tunneling regime (and the BSI regime too if possible). Reference [67] has concluded that the ionization rate from the ADK model[65] is the best choice here for two reasons. First, among the different theoretical models, it agrees best with numerical solutions of time dependent Schrondinger equation (TDSE) for the hydrogen atom in the tunneling and BSI regimes[66]. Second, it agrees best with experimental results in [68].

The ionization rate given by the ADK model can be rewritten in convenient units as [67]

$$w(s^{-1}) \approx 1.52 \times 10^{15} \frac{4^{n^*}\xi_i(eV)}{n^*\Gamma(2n^*)}(20.5\frac{\xi_i^{3/2}(eV)}{E(GV/m)})^{2n^*-1} \times exp(-6.83\frac{\xi_i^{3/2}(eV)}{E(GV/m)}), \tag{4.2}$$

where ξ_i is the ionization energy and $n^* \approx 3.69Z/\xi_i^{1/2}(eV)$ is the effective principal quantum number. For a specific type of gas, this rate is only a function of the external electric field. For example, for $Li \rightarrow Li^+$, $\xi_i = 5.39eV$, the ionization rate is

$$w_{Li}(s^{-1}) \approx \frac{3.51 \times 10^{21}}{E^{2.18}(GV/m)} exp(\frac{-85.5}{E(GV/m)}). \tag{4.3}$$

The probability of ionization or the fraction of ionized atoms/ions can be obtained by integrating this rate over time, $p = \int w(t)dt$. Fig. 4.2 shows the ionized fraction calculated from the ADK formula versus the electric field during $\Delta t = 200fs$ for different types of gases. This Δt is roughly the transit time of a short beam driver in PWFA experiments ($\Delta t = 6\sigma_z/c$, $\sigma_z \approx 10\mu m$).

From Fig. 4.2 we can see that the ionization rates are similar to step functions in E. The ionized fraction is not very sensitive to the ionization time but very sensitive to the electric field. Therefore, for each type of gas, there is roughly a threshold electric field for full ionization. For example, for $Li \rightarrow Li^+$, $E_{th} \approx 5GV/m$.

In order to estimate the extent of ionization, a simple calculation of the electric field from a relativistic bi-gaussian beam is done. Since the beam velocity is near c, its electric field is dominantly in the transverse direction ($E_r \gg E_{||}$). Using Guass's law, we can get the expression of E_r as a function of r and ξ (see Fig. 4.3)

$$\begin{aligned} E_r(r,\xi) &= \frac{eN}{\epsilon_0(2\pi)^{3/2}\sigma_z} e^{-\frac{\xi^2}{2\sigma_z^2}} \frac{1-e^{-\frac{r^2}{2\sigma_r^2}}}{r} \\ &= 22960(\frac{N}{2\times 10^{10}}) \frac{1}{\sigma_z(\mu m) r(\mu m)} e^{-\frac{\xi^2}{2\sigma_z^2}} (1-e^{-\frac{r^2}{2\sigma_r^2}})(GV/m) \end{aligned} \tag{4.4}$$

As shown in Fig. 4.4(a), E_r is still a gaussian distribution in the longitudinal direction and has the same σ_z as the beam profile. While in the radial direction, as shown in Fig. 4.4(b), it is zero for both $r = 0$ and $r \rightarrow \infty$ and reaches a maximum value at $r = 1.585\sigma_r$ for any specific ξ. The overall maximum of E_r is at $\xi = 0$ and $r = 1.585\sigma_r$

$$E_{r-max}(\xi = 0, r = 1.585\sigma_r) = 10360(\frac{N}{2\times 10^{10}}) \frac{1}{\sigma_z(\mu m)\sigma_r(\mu m)} (GV/m) \tag{4.5}$$

It is proportional to the number of electrons in the beam and inversely proportional to σ_r and σ_z.

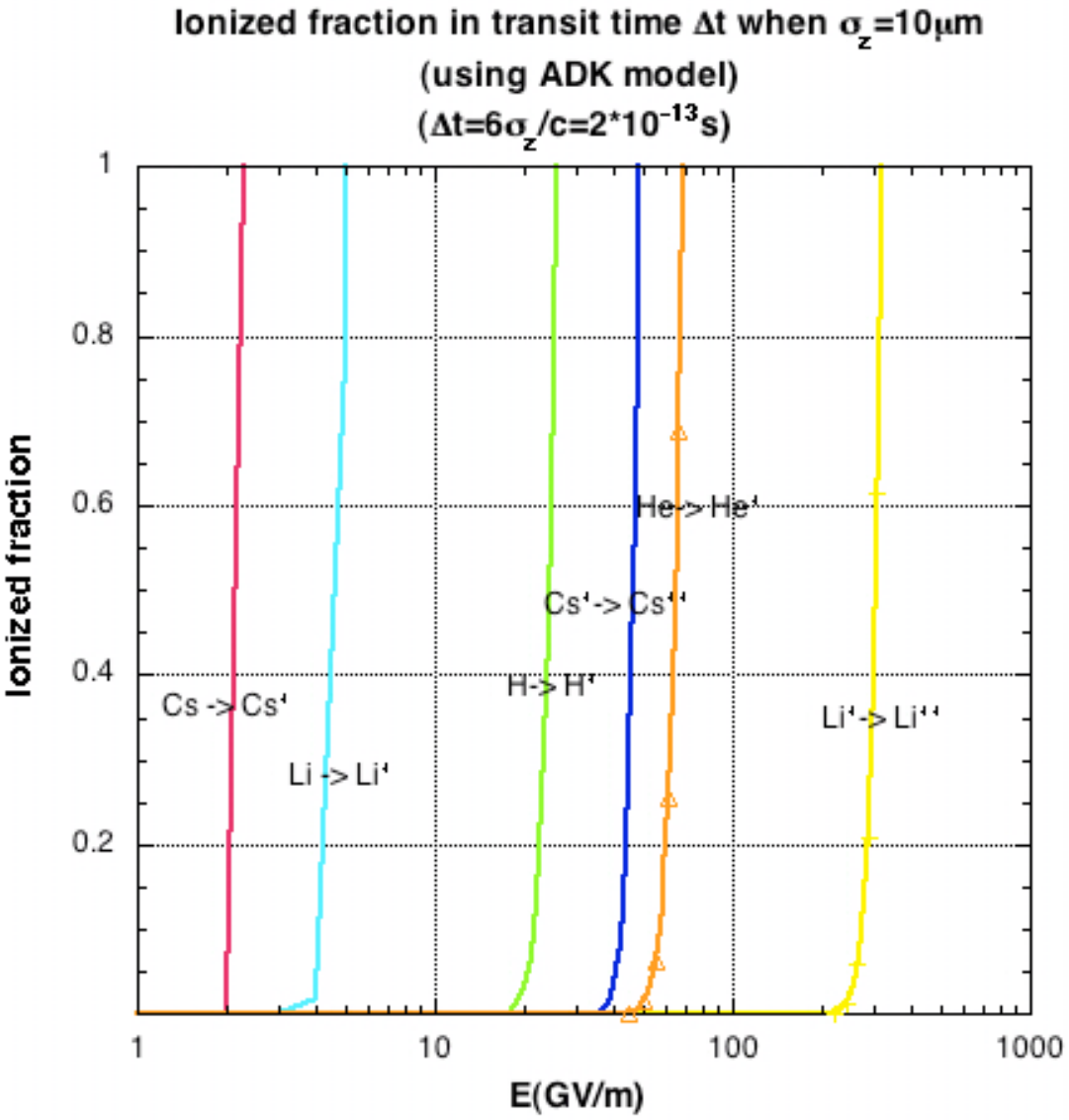

Figure 4.2: Threshold electric fields of full ionization for different types of atoms/ions

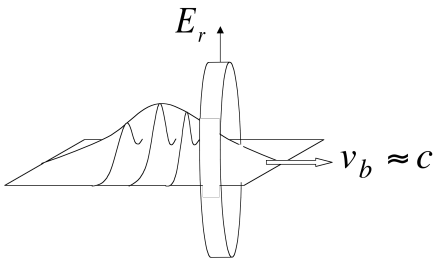

Figure 4.3: Electric field of a relativistic bi-gaussian beam

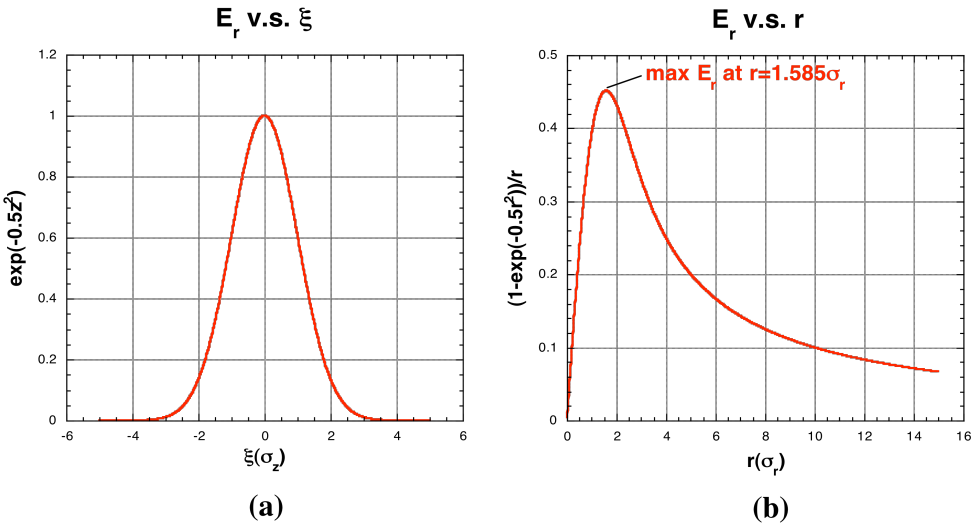

Figure 4.4: Electric field of a relativistic bi-gaussian beam in the (a) longitudinal and (b) transverse directions

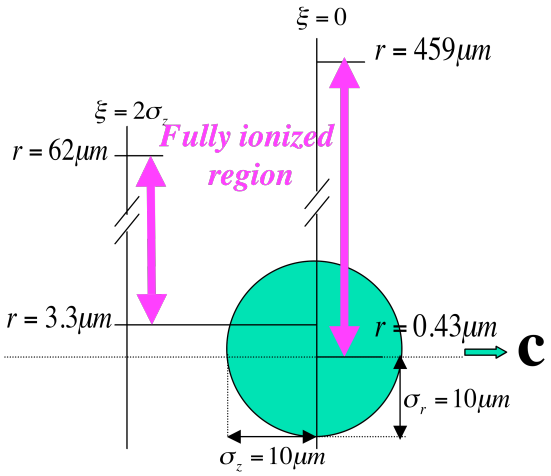

Figure 4.5: Fully ionized region of a short beam

For example, for a beam with $N = 2 \times 10^{10}$, $\sigma_r = 10\mu m$ and $\sigma_z = 10\mu m$, E_{r-max} is $103.6GV/m$. If we use $E > 5GV/m$ as a rough criteria for full ionization, then for this beam, as shown in Fig. 4.5, the full ionization region at $\xi = 0$ extends from $r = 0.43\mu m$ to $459\mu m$, and that at $\xi = 2\sigma_z$ extends from $r = 3.3\mu m$ to $62\mu m$.

It is important to know the extent of full ionization because if full ionization is not reached for most of the cross sectional area near the beam, the plasma wake generated will degrade compared with a pre-ionized one as has been observed in some full PIC simulations[67].

4.1.2 The ionization package in QuickPIC

While adding ionization into QuickPIC, there are several complications due to either different physics for ionized electrons or the code structure.

The first concern was the normalization. In QuickPIC, at the beginning of each simulation, the code reads the input parameters in physical units and con-

verts them into normalized units based on the actual plasma density . For example, from cm^{-3} to n_p and from μm to $\frac{c}{\omega_p}$. Then, separate input files are written for the 3D part and the 2D part of the code, using these normalized parameters. (The 3D and 2D parts used to be two separate codes and can be run independently.) Using normalized parameters means that both the 3D and the 2D parts lose information of the absolute value of quantities and only have the knowledge of their ratios to the common basis (the normalizing quantities). However, they still yield meaningful results because the 3D and the 2D parts are correctly scaled. In this sense, each simulation actually represents a series of physical processes which have different set of physical parameters but a common set of normalized parameters.

This normalization scheme needs to be reconsidered when ionization is added. First, we can no longer choose the actual plasma density as the normalizing density (as is typically done in the code). Instead, we arbitrarily choose one value and normalize other quantities (including the actual plasma density and neutral density) in terms of it. Second, since the ionization rate needs quantities in physical units (e.g. electric field in GV/m, Δt in second), extra information in physical units (e.g. $n_{normalizing}$ in cm^{-3}, simulation box length in μm) needs to be written in the 2D input file. This information is used to convert quantities back into physical units before calculating the ionization probability. This leads to one important property of this type of simulation, that is, each simulation only represents one actual physical gas density and beam density because ionization is a process involving 'absolute values' and can not be scaled.

Besides the reconsideration of the normalization, there are two other major concerns, which are associated with QuickPIC's specific algorithms.

First, we need to rethink the calculation of $p_{||}$ and γ of the ionized electrons

based on the conserved quantity as mentioned in Chapter 2. From appendix A we know, for all plasma electrons

$$\frac{d(\gamma - \widetilde{p_z} + \widetilde{q_e}\widetilde{\psi})}{dt} = \frac{\widetilde{q_e}e}{mc}\frac{\partial}{\partial s}(\phi - \beta \cdot \mathbf{A}) \tag{4.6}$$

Based on the spirit of quasi-static approximation ($\frac{\partial}{\partial s} \approx 0$), we know

$$\gamma - \widetilde{p_z} + \widetilde{q_e}\widetilde{\psi} \approx const. \tag{4.7}$$

i.e., $\gamma - \widetilde{p_z} + \widetilde{q_e}\widetilde{\psi}$ is a time conserved quantity. For electrons in pre-ionized plasmas, there is always a moment in each electron's history for which it is stationary at far ahead of the beam. In this case, the constant can be evaluated that its $\gamma = 1$, $p_z = 0$ and the potentials are $\mathbf{A} = 0$, $\phi = 0$ before the drive beam reaches the particle. (We choose $\mathbf{A} = 0$, $\phi = 0$ for unperturbed regions ahead of the beam where $\mathbf{j} = 0$ and $\rho = 0$). Therefore, this constant for pre-ionized electrons is always 1 is assumed. However, if the electrons are born inside the perturbed region (such as the ionized electrons born near the beam), their initial $\mathbf{A}$ and ϕ are normally non-zero and this needs to be taken into account. In this case, the constant should be written as

$$\gamma - \widetilde{p_z} + \widetilde{q_e}\widetilde{\psi} \approx 1 + \widetilde{q_e}\widetilde{\psi_0} \tag{4.8}$$

where $\widetilde{\psi_0} = \widetilde{\phi_0} - \widetilde{a}_{z0}$ is the initial normalized pseudo-potential at the initial position where it is assumed the electron is born at rest. Based on (4.8), the calculation of γ and p_z are changed accordingly from (3.37) and (3.38) to

$$\widetilde{p_z} \approx \frac{1 + \widetilde{p}_\perp^2 - (1 + \widetilde{\psi} - \widetilde{\psi_0})^2}{2(1 + \widetilde{\psi} - \widetilde{\psi_0})} \tag{4.9}$$

$$\gamma \approx \frac{1 + \widetilde{p}_\perp^2 + (1 + \widetilde{\psi} - \widetilde{\psi_0})^2}{2(1 + \widetilde{\psi} - \widetilde{\psi_0})}. \tag{4.10}$$

Another concern comes from the choice of the 'diffusion coefficient' when solving for the fields. As has been described in chapter 3, the 'diffusion coefficient'

depends on the plasma density in a pre-ionized case. During the first stage of the ionization package, we chose this 'diffusion coefficient' based on the neutral density accordingly. It appears that this simple choice gives accurate enough wakes even when the beam's electric field is just above ionization threshold (see benchmark in next section). In the future, improvement can be made by setting this diffusion coefficient according to the local ionized plasma density which varies with each 2d step. This should hopefully require fewer iterations in order to get agreement with full PIC codes.

Adding the ionization package was done by generating a new field-ionized electrons species. This species is deposited in the same way as the pre-ionized electrons and is pushed in the same way too except for the calculation of γ and $p_{||}$. Although most parallel operations are hidden inside the lower layer of the Framework, caution still needed to be taken at several places, such as generating particles near the processor boundaries, using guard cells when depositing ionized electrons, and broadcasting parameter namelists during initialization. Other details include determining the particle positions inside the cell (i.e. quiet start – which has an effect on the hosing instability), method of integrating the ionization rate, and converting units between the 3D part and 2D part of the code.

4.1.3 Benchmark of field-ionized wakes

We compared the field-ionized longitudinal wake from QuickPIC with those from OSIRIS[69, 70]. Fig. 4.6(a) is a case where the space charge fields near the beam are considerably above lithium's ionization threshold ($E_{rmax} = 26GV/m$), while (b) is a case where they are near the threshold ($E_{rmax} = 11.7GV/m$). In Fig. 4.6(a), a parameter scan is presented in order to check the influence of the simulation parameters, such as the number of particles per cell and resolution in

the z direction. We can see that for all these simulation parameters with ≥ 4 particles per cell and $\leq 0.15\frac{c}{\omega_p}$ per grid (i.e. ≥ 42 grids per plasma wavelength), the results change little. In fact, the QuickPIC results might be more correct because of subtle issues regarding initializing the drive beam (see discussion later). The OSIRIS result in (a) is from a 3D simulation while that of (b) is from a 2D (r-z) simulation. In the past we have shown that for short propagation distances the differences between 2D and 3D OSIRIS are negligible.

In both cases, QuickPIC and OSIRIS agree very well. The only slight differences are in the magnitude of: (1) The first decelerating fields (slightly smaller in QuickPIC); (2) The value of the very spike of the first accelerating peak; and (3) In some cases, the second and later accelerating and decelerating peaks. Among these, (2) and (3) have little effect for problems we are interested in. In fact, given that the first accelerating peaks almost overlap, the value of the spike will not influence the energy gain much since number of particles residing inside this spike is very small. Moreover, since in most cases only the first accelerating peak is used for beamloading and it is not influenced by any physical process that's behind it ($v \sim c$), the differences in the second and later peaks have little relevance. One effect for (1), is that an error in the decelerating field means an error in the transformer ratio, which may become relevant if pump depletion becomes a critical issue.

Very recently, we identified the reason for the discrepancy. In these benchmarks, the diffusion coefficient is chosen for the fully ionized density. However, before ionization, there is no plasma. Therefore, the diffusion coefficient effectively shields out the vacuum fields of the beam for $k's < \omega_p/c$. Since the dominant wavenumber for the self-fields is $k \sim 1/\sigma_r$, then if $k_p\sigma_r << 1$, this will have little effect. This issue was resolved by not iterating the solution for the self-fields

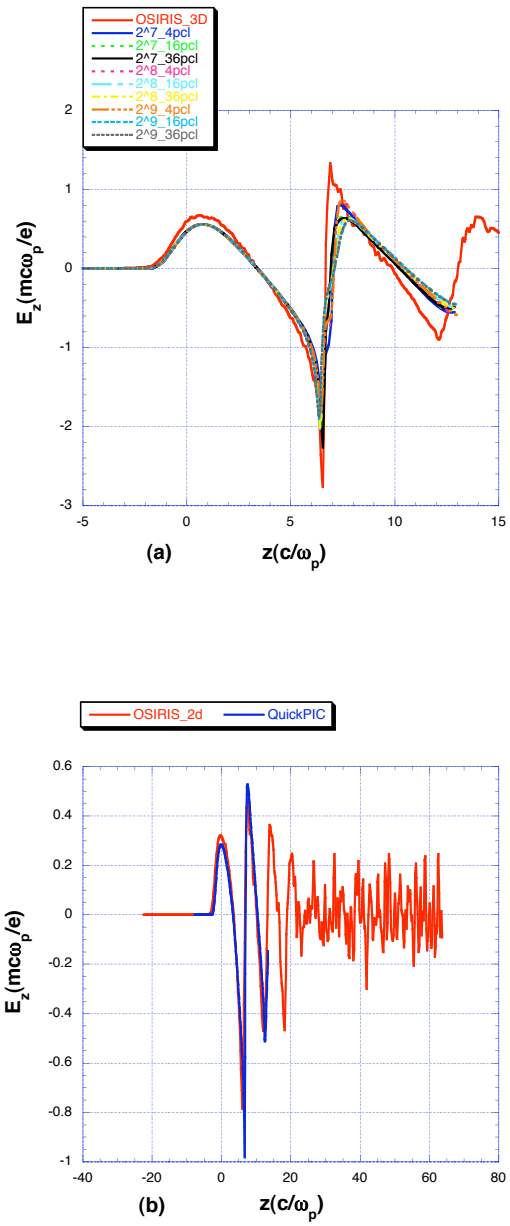

Figure 4.6: Benchmark of self-ionized plasma wake versus OSIRIS results. (a) High above threshold ($N_b = 2 \times 10^{10}$, $\sigma_r = 20\mu m$, $\sigma_z = 20\mu m$, $n_p = 1.25 \times 10^{17} cm^{-3}$) (b) Just above threshold ($N_b = 2 \times 10^{10}$, $\sigma_r = 14.1\mu m$, $\sigma_z = 63\mu m$, $n_p = 4.2 \times 10^{16} cm^{-3}$)

of the beam and improving the predictor. When this was done, there was excellent agreement between QuickPIC and OSIRIS. However, at the moment, there are subtle effects at the conducting boundary. We have found that the numerics issue just described does not effect the physics studied in this dissertation. As a result, the numerical choices used throughout for the predictor-corrector represent the best compromise for speed versus accuracy. Improving the numerics of the self-ionization routine is an area for future work.

Another related issue for QuickPIC is the choice of the 'diffusion coefficient' when the plasma volume is only partially ionized. As stated above, the diffusion coefficient is chosen based on the neutral density instead of the real plasma density by assuming that the iteration converges to the same value fast enough despite differences in this coefficient. However, this may cause error when the plasma density is not constant when the plasma is not fully ionized. In the future, it might be necessary to use a diffusion coefficient which varies with the local plasma density in each 2D step.

Given the overall good agreement with OSIRIS and bearing in mind the issues discussed above, we can explore some problems in the self-ionized PWFA research using QuickPIC with at least a factor of ~ 100 times improvement in computing speed.

4.2 Radiation reaction

As we know, an accelerating charged particle will radiate through electromagnetic fields (or photons) and this radiation carries energy and momentum. In order to satisfy energy and momentum conservation, the charged particle must experience a recoil at the time of emission, i.e. the radiation must exert an addi-

tional force (self-force) on the charged particle. The equation of motion will then have the form

$$\frac{d\mathbf{p}}{dt} = \mathbf{F}_{ext} + \mathbf{F}_{rad} \tag{4.11}$$

where $\mathbf{F}_{ext}$ is the external force and $\mathbf{F}_{rad}$ is the radiation reaction force.

The classical aspects of the radiation reaction is discussed in chapter 16 of [71] and $\mathbf{F}_{rad}$ is known as the Abraham-Lorentz force in the nonrelativistic limit and the Lorentz-Dirac force in the relativistic limit. One alternative form of the relativistic Lorentz-Dirac force in terms of external force and particle velocity is derived in [73] and summarized in [71] as

$$\mathbf{F}_{rad} = \tau_e[\gamma\frac{d\mathbf{F}}{dt} - \frac{\gamma^3}{c^2}\frac{d\mathbf{v}}{dt} \times (\mathbf{v} \times \mathbf{F})] \tag{4.12}$$

where $\tau_e = \frac{2}{3}\frac{e^2}{mc^3} = 6.26 \times 10^{-24}s$ is the characteristic time for electron and $\mathbf{F}$ is the external force. (All $\mathbf{F}$s hereafter will be referring to external forces). Note that $\mathbf{v} \cdot \mathbf{F}_{rad} = P_{loss}$.

In most applications, $\mathbf{F}_{rad}$ is much smaller than the external force. Therefore most PIC codes do not include the $\mathbf{F}_{rad}$ term inside the equation of motion. However, in the application of PWFA, the cumulative effects from $\mathbf{F}_{rad}$ is no longer negligible. In fact, the energy loss due to radiation can be on the same order as the energy gain from the wakefield (e.g. as in the SLAC multi-GeV energy gain experiment [44]). Correctly modeling this effect will influence many important aspects of the system, such as the pump depletion distance, the highest energy gain, etc .

To estimate the importance of $\mathbf{F}_{rad}$ for current and future plasma or laser wakefield accelerators (in this case, the trailing beam will radiate), we start from the relativistic Larmor formula:

$$P_{loss} = -\frac{2}{3}\frac{e^2}{c}\gamma^6[(\dot{\vec{\beta}})^2 - (\vec{\beta} \times \dot{\vec{\beta}})^2] \tag{4.13}$$

or equivalently

$$P_{loss} = -\frac{2}{3}e^2m^2c^3(\frac{dp_\mu}{d\tau}\frac{dp^\mu}{d\tau}) \tag{4.14}$$

where p_μ are the components of the energy momentum 4-vector and τ is the proper time.

For an electron executing a betatron oscillation in asymmetric ion channel, $\vec{\beta} \approx c\hat{\mathbf{z}}$ and $\dot{\vec{\beta}} \approx \hat{x}\frac{\omega_\beta}{\gamma}x_0 cos(\omega_\beta t + \phi_x) + \hat{y}\frac{\omega_\beta}{\gamma}y_0 cos(\omega_\beta t + \phi_y)$, where $\omega_\beta = \frac{\omega_p}{\sqrt{2\gamma}}$ and x_0 and y_0 are the maximum offsets for the particle in the x and y directions. Substituting these trajectories into (4.13) and assuming $x_0 = y_0 = r_0$ gives

$$P_{loss} = -\frac{1}{3}\frac{e^2}{c^3}\omega_p^4\gamma^2 r_0^2. \tag{4.15}$$

If we use this to define a decelerating electric field $P_{loss} = eE_{rad}c$, then the ratio of decelerating field to the accelerating wakefield can be written as

$$\frac{E_{rad}}{E_{acc}} \approx \frac{1}{\frac{eE_{acc}}{mc\omega_p}} 1.5 \times 10^{-5}(\frac{\gamma mc^2}{50GeV})^2(\frac{n}{10^{16}cm^{-3}})^{\frac{3}{2}}(\frac{r_0}{1\mu m})^2 \tag{4.16}$$

Furthermore, if we assume that the beam's spot size $\sigma_r \approx r_0$ is chosen such that the beam is matched, $\beta^* = \omega_\beta/c$, then for a matched beam

$$\frac{E_{rad}}{E_{acc}} \approx \frac{1}{\frac{eE_{acc}}{mc\omega_p}} 3.75 \times 10^{-3}(\frac{\gamma mc^2}{250GeV})^{\frac{3}{2}}(\frac{n}{10^{16}cm^{-3}})(\frac{\varepsilon_n}{10^{-6}m}), \tag{4.17}$$

where ε_n is the normalized emittance. For example, in the E-167 experiment where $\gamma mc^2 = 42.5GeV$, $n \approx 2.7 \times 10^{17}cm^{-3}$, $r_0 \sim 10\mu m$, then $\frac{E_{rad}}{E_{acc}} \sim 0.15$ for $\frac{eE_{acc}}{mc\omega_p} \sim 1$. For a future collider with $\varepsilon_n \sim 10^{-6}m$, $n \sim 10^{17}cm^{-3}$ and $\gamma mc^2 \sim 500GeV$, then $\frac{E_{rad}}{E_{acc}} \sim 0.1$ for $\frac{eE_{acc}}{mc\omega_p} \sim 1$.

Applying (4.12) in the equation of motion in the code directly would retain most accuracy. However, since there is a term which includes the time derivative of the force, the implementation is not trivial. In the next 3 subsections, we will demonstrate that for our applications, a simple method using an effective electric

field in the longitudinal direction, $\mathbf{F}_{rad} = \hat{\mathbf{z}} P_{rad}/ec$, models the radiation drag accurately enough. In the last subsection, test results using this effective fields in QuickPIC will be shown.

4.2.1 Simplified form of the relativistic Larmor formula

In this section, we provide more detail in obtaining (4.15). We start from (4.14). Writing out these components explicitly gives

$$\begin{aligned} P_t &= -\frac{2}{3}\frac{e^2\gamma^2}{c}[(\frac{d\gamma}{dt})^2 - (\frac{d\bar{\mathbf{p}}_\perp}{dt})^2 - (\frac{d\bar{p}_z}{dt})^2] \\ &= \frac{2}{3}\frac{e^2\gamma^2}{c}[(\frac{d\bar{\mathbf{p}}_\perp}{dt})^2 + (\frac{d\bar{p}_z}{dt})^2 - \frac{\bar{p}^2}{1+\bar{p}^2}(\frac{d\bar{p}}{dt})^2] \\ &= \frac{2}{3}\frac{e^2\gamma^2}{c}[\underbrace{(\frac{d\bar{\mathbf{p}}_\perp}{dt})^2}_{[1]} + \underbrace{(\frac{d\bar{p}_z}{dt})^2}_{[2]} - \underbrace{\frac{1}{1+\bar{p}^2}(\bar{p}_\perp\frac{d\bar{p}_\perp}{dt} + \bar{p}_z\frac{d\bar{p}_z}{dt})^2}_{[3]}] \end{aligned} \tag{4.18}$$

where $\bar{p} = \frac{p}{mc}$ is the normalized momentum and the relation $\gamma = \sqrt{1+\bar{p}^2}$ as well as $\bar{p} = \sqrt{\bar{p}_\perp^2 + \bar{p}_z^2}$ have been used. We will show shortly that for beam particles in our PWFA applications, $[2] - [3] << [1]$, therefore only [1] contributes.

In order to make estimates of these 3 terms in a PWFA application, the following assumptions are made. Firstly, for all beam particles, $\frac{\bar{p}_z}{\bar{p}_\perp} >> 1$ and $\bar{p} \approx \bar{p}_z >> 1$, which are well satisfied in relevant PWFA parameters. Therefore

$$\frac{d\bar{p}_z}{dt} \approx -eE_z, \tag{4.19}$$

i.e., the magnetic force along $\hat{\mathbf{z}}$ is negligible. Secondly, the beam particles of interest reside within the ion channel. Without loss of generality, we consider an electron oscillating in one plane, e.g., the x-z plane. In what follows, let r represent x.

$$\frac{d\bar{p}_\perp}{dt} \propto E_{rmax} \cdot cos\omega_\beta t, \tag{4.20}$$

where $E_{rmax} = 2\pi e^2 n_0 r_{max}$ is the maximum transverse focusing field, which is proportional to the maximum oscillation radius r_{max}, and $\omega_\beta = \frac{\omega_p}{\sqrt{2\bar{\gamma}}}$ is the betatron frequency. Using (4.19) and (4.20), (4.18) becomes

$$\begin{aligned}[1] + [2] - [3] &\propto (E_{rmax} \cdot cos\omega_\beta t)^2 + E_z^2 - \frac{1}{1+\bar{p}^2}(\bar{p}_\perp E_{rmax} \cdot cos\omega_\beta t + \bar{p}_z E_z)^2 \\ &\propto \underbrace{\alpha^2 \cdot cos^2\omega_\beta t}_{[1]'} + \underbrace{1}_{[2]'} - \underbrace{\frac{1}{1+\bar{p}^2}(\bar{p}_\perp \alpha \cdot cos\omega_\beta t + \bar{p}_z)^2}_{[3]'} \end{aligned} \tag{4.21}$$

where $\alpha \equiv \frac{E_{rmax}}{E_z}$.

Because E_{rmax} is proportional to r_{max} and E_z depends on the z location of the beam particle as shown in Fig. 4.7 line E_z, α is a function of the location (r_{max}, z). Depending on the value of α, the beam can be divided into 3 regions as shown in Fig. 4.7 – (a) $\alpha < 1$ (b)$1 < \alpha << \frac{\bar{p}_z}{\bar{p}_\perp}$ (c) $\alpha >\sim \frac{\bar{p}_z}{\bar{p}_\perp}$. (Note: the particles in the beam head, where neither E_z nor E_r is established, are not of interest because they have minimal radiation).

In regions (b) and (c), it is straightforward to show that $[1]' >> [2]' - [3]'$ through

$$\frac{[1]'}{[2]' - [3]'} = \frac{\alpha^2 \cdot cos^2\omega_\beta t}{1 - \frac{1}{1+\bar{p}^2}(\bar{p}_\perp \cdot \alpha cos\omega_\beta t + \bar{p}_z)^2}, \tag{4.22}$$

$$(\frac{[1]'}{[2]' - [3]'})_b \approx \frac{\alpha^2 \cdot cos^2\omega_\beta t}{1 - \frac{1}{1+\bar{p}^2}\bar{p}_z^2} >> 1, \tag{4.23}$$

$$(\frac{[1]'}{[2]' - [3]'})_c \approx \frac{\alpha^2 \cdot cos^2\omega_\beta t}{1 - \frac{1}{1+\bar{p}^2}(\sim \bar{p}_\perp \cdot \alpha cos\omega_\beta t)^2} = \frac{cos^2\omega_\beta t}{\frac{1}{\alpha^2} - \frac{1}{1+\bar{p}^2}(\sim \bar{p}_\perp \cdot cos\omega_\beta t)^2} >> 1. \tag{4.24}$$

Here, the overall effect averaged over one betatron oscillation is considered (i.e. $\langle cos^2\omega_\beta t\rangle \sim 1$). However, since there are particles very close to the axis in region (a), more careful treatment needs to be used. For these particles ($\alpha \to 0$), we

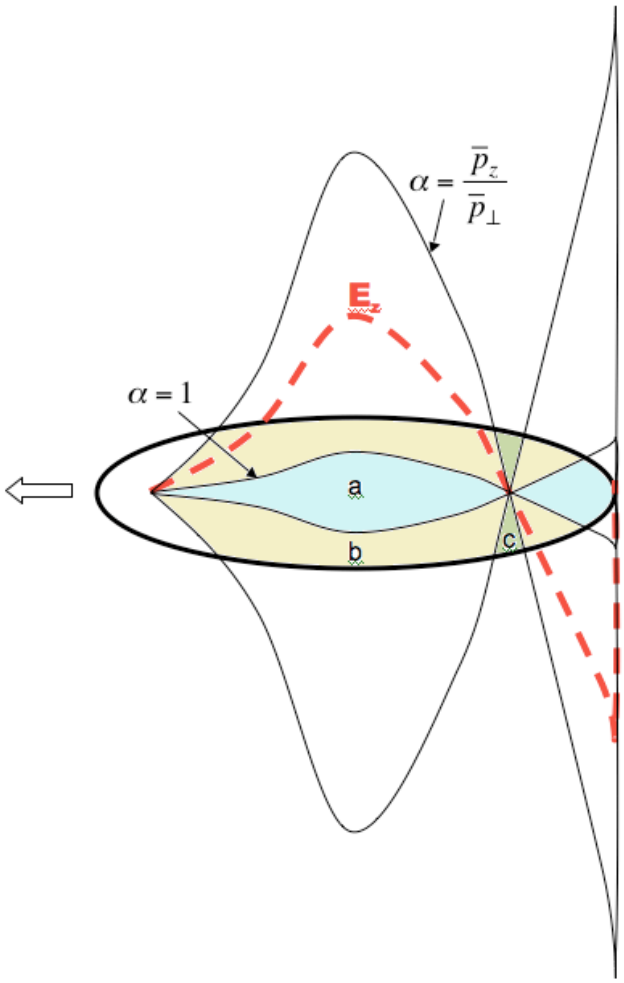

Figure 4.7: Three regions of the beam particles according to the value of $\alpha = \frac{E_{rmax}}{E_z}$ (a)$\alpha < 1$ (blue) (b)$1 < \alpha << \frac{\bar{p}_z}{\bar{p}_\perp}$ (yellow) and (c) $\alpha >\sim \frac{\bar{p}_z}{\bar{p}_\perp}$ (green)

have

$$\begin{aligned}\lim_{\alpha\to 0}|\frac{[1]'}{[2]'-[3]'}|_a &= \lim_{\alpha\to 0}|\frac{\alpha^2\cdot cos^2\omega_\beta t}{1-\frac{1}{1+\bar{p}^2}(\bar{p}_\perp\cdot\alpha cos\omega_\beta t+\bar{p}_z)^2}|\\ &= \lim_{\alpha\to 0}\frac{2\alpha\cdot cos^2\omega_\beta t}{\frac{2}{1+\bar{p}^2}(\bar{p}_\perp\cdot\alpha cos\omega_\beta t+\bar{p}_z)\cdot\bar{p}_\perp\cdot cos\omega_\beta t}\\ &= \lim_{\alpha\to 0}\frac{2cos^2\omega_\beta t}{\frac{2(\bar{p}_\perp\cdot cos\omega_\beta t)}{1+\bar{p}^2}\bar{p}_\perp\cdot cos\omega_\beta t}\\ &= \frac{1+\bar{p}^2}{\bar{p}_\perp^2} >> 1 \end{aligned} \tag{4.25}$$

which means that even for particles very close to the axis, the inequality $[1]' >> [2]' - [3]'$ still holds.

The previous paragraph shows that for all beam particles of interest in a PWFA application, (4.18) can reduce to the following simplified form with very good accuracy.

$$P_t = \frac{2}{3}\frac{e^2\gamma^2}{c}(\frac{d\bar{\mathbf{p}}_\perp}{dt})^2 \tag{4.26}$$

This is in agreement with the argument used in sec. 4.2.

4.2.2 Direction of the radiation reaction force

In reference [72], it was shown that for a partice executing a zeroth order betatron oscillation in one plane (x-z) without any axial accelerating field, $F_z = 0$, then the radiation reaction force can be written as,

$$F_{radx} = -c^3\tau_e K^2\gamma m v_x(1+K^2\gamma x^2) \tag{4.27}$$

$$F_{radz} = -mc^3\tau_e\gamma^2 K^4 x^2 \tag{4.28}$$

where $K^2 = k_p^2/2$. The ratio of F_{radx}/F_{radz} can be written as

$$\frac{F_{radx}}{F_{radz}} = \frac{v_x}{c}\frac{1+K^2\gamma x^2}{K^2\gamma x^2}. \tag{4.29}$$

The quantity $\frac{v_x}{c} \approx \theta$ where θ is the instantaneous angle of the particle's trajectory in the x-z plane. Therefore if $K^2\gamma x^2 >> 1$, the radiation reaction force is parallel to $\mathbf{v}$. This can be rewritten as $k_p^2\sigma_r^2\gamma/2 >> 1$ which is easily satisfied in the SLAC experiments. For matched beams where $\beta^* \approx \frac{1}{k_\beta}$, then $k_p^2\sigma_m^2\gamma/2 = k_p\varepsilon_n\sqrt{2\gamma}$. In a future collider at the TeV energy range $k_p\varepsilon_n \sim 1/50$ and $\sqrt{2\gamma} \sim 10^3$, so it is still $>> 1$.

In this section, we estimate how the relative direction of $\mathbf{F_{rad}}$ might change when F_z and $\frac{dF_z}{dt} \neq 0$.

In order to compare the parallel and perpendicular components of $\mathbf{F}_{rad}$ for $F_z, \frac{dF_z}{dt} \neq 0$, we once again assume that the beam particle oscillates in the x-z plane ($y = v_y = 0$)under a linear focusing force $F_x = -kx$, where $k = 2\pi n_p e^2 \equiv K^2$ (See Fig. 4.8). The perpendicular and parallel components of $\mathbf{F}_{rad}$ then can be written out as, (note that // and $\perp$ are not defined with respect to the particle's instantaneous trajectory, but are defined with respect to the ion column, i.e. $\hat{//} \equiv \hat{\mathbf{z}}$).

$$F_{radx} = \tau_e\{\gamma\frac{dF_x}{dt} - \frac{\gamma^3}{c^2}[\frac{dv_z}{dt}(v_xF_z - v_zF_x)]\}, \tag{4.30}$$

$$F_{radz} = \tau_e\{\gamma\frac{dF_z}{dt} - \frac{\gamma^3}{c^2}[\frac{dv_x}{dt}(-v_xF_z + v_zF_x)]\}. \tag{4.31}$$

Before proceeding, we note that if one starts from (4.30) and (4.31), it is very straightforward to show that if $F_z = 0$ then $\frac{F_{radx}}{F_{radz}} = \frac{v_x}{v_z}\frac{1+\gamma K^2x^2}{\gamma K^2x^2}$, recovering the results from [72].

Next, we estimate the importance of the F_z by considering at the two locations – oscillation peak, point A, where $x = a$, $p_x = v_x = 0$; and where the particle crosses the axis, point B, where $x = 0$, $F_x = \frac{dp_x}{dt} = 0$ and $v_x = v_{xmax} = a\omega_\beta = \frac{2\pi ac}{\lambda_\beta}$, where $\lambda_\beta = \sqrt{\frac{2\pi\gamma mc^2}{n_pe^2}}$.

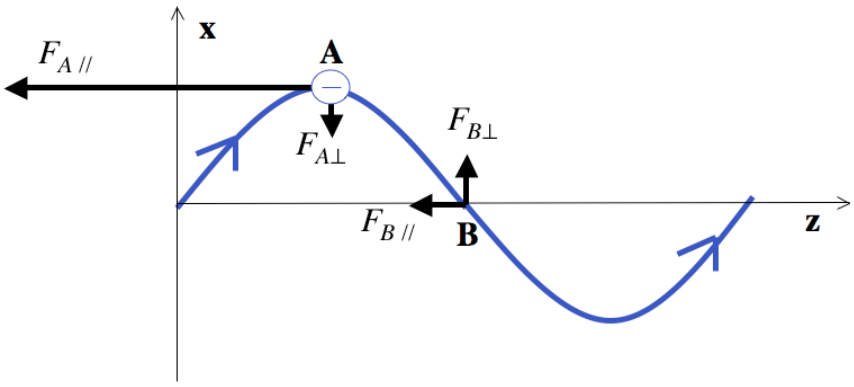

Figure 4.8: Direction of the radiation reaction force for a particle oscillating in the x-z plane

Before we proceed, we write out several terms in (4.30) and (4.31).

$$\frac{dF_x}{dt} = -K^2 v_x \tag{4.32}$$

$$\frac{dF_z}{dt} \approx -e\frac{dE_z}{dt} \tag{4.33}$$

where $v_z >> v_\perp$ is assumed in (4.33). Using $p = \gamma m v$, we have

$$\frac{dv_{x,z}}{dt} = \frac{1}{\gamma m}\frac{dp_{x,z}}{dt} - \frac{v_{x,z}}{\gamma}\frac{d\gamma}{dt}. \tag{4.34}$$

Since $\gamma = \sqrt{1 + \frac{p_x^2}{m^2c^2} + \frac{p_z^2}{m^2c^2}}$, $\frac{d\gamma}{dt} = \frac{1}{\gamma m^2 c^2}(p_x\frac{dp_x}{dt} + p_z\frac{dp_z}{dt})$. At both A ($p_x = 0$) and B($\frac{dp_x}{dt} = 0$), $(\frac{d\gamma}{dt})_{A,B} = \frac{p_z}{\gamma m^2 c^2}\frac{dp_z}{dt}$. Therefore,

$$(\frac{dv_z}{dt})_{A,B} = \frac{1}{\gamma m}(1 - \frac{v_z^2}{c^2})\frac{dp_z}{dt} \approx \frac{1}{m\gamma^3}\frac{dp_z}{dt} = -\frac{1}{m\gamma^3}eE_z \tag{4.35}$$

$$(\frac{dv_x}{dt})_A = \frac{1}{\gamma m}\frac{dp_x}{dt} = \frac{1}{\gamma m}F_x = -\frac{1}{\gamma m}ka \equiv -\frac{1}{\gamma m}eE_{rmax} \tag{4.36}$$

$$(\frac{dv_x}{dt})_B = -\frac{v_{xmax}}{\gamma}\frac{d\gamma}{dt} \tag{4.37}$$

The key assumption for (4.35) is that $v_z >> v_x$ at point B.

Since $v_x = 0$ at A, $\mathbf{F}_{rad}$ at A can be written out as

$$F_{radxA} = \tau_e(\cancel{-\gamma k v_x} + \underbrace{0}_{} + \underbrace{\frac{\gamma^3}{c^2}\frac{dv_z}{dt}v_z F_x}_{\text{[a]}}) \tag{4.38}$$

$$F_{radzA} = \tau_e(\underbrace{-\gamma e\frac{dE_z}{dt}}_{\text{[b]}} - \underbrace{\frac{\gamma^3}{c^2}\frac{dv_x}{dt}v_z F_x}_{\text{[c]}}) \tag{4.39}$$

Using (4.35) and (4.36)

$$\frac{[a]}{[c]} = \frac{\frac{dv_z}{dt}}{\frac{dv_x}{dt}} \approx \frac{1}{\gamma^2}\frac{\frac{dp_z}{dt}}{\frac{dp_x}{dt}} = \frac{1}{\gamma^2}\frac{E_z}{E_{rmax}} = \frac{1}{\gamma^2\alpha} \tag{4.40}$$

As discussed in the previous section, it is obvious that for almost all particles in the beam, $\alpha >> \frac{1}{\gamma^2}$ (except those traveling exactly on axis which has a negligibly small number). Therefore $[a] << [c]$.

In order to compare [b] and [c], we rewrite [c] using (4.36)

$$[c] = \frac{\gamma^2}{mc^2}v_z F_x^2 \approx \frac{\gamma^2 k^2 a^2}{mc}. \tag{4.41}$$

Here $v_z \approx c$ is assumed. Because E_z barely changes during the a betatron oscillation (i.e. there is little phase slippage), it is reasonable to assume that $\frac{dE_z}{dt}$ is negligibly small and this can be confirmed quantitatively as described later. In order for $[b] << [c]$ to be true, $\frac{dE_z}{dt}$ needs to satisfy the following relation.

$$\frac{dE_z}{dt} << \frac{\gamma k^2 a^2}{emc} \tag{4.42}$$

This means, the change of E_z due to phase slippage within one betatron oscillation needs to satisfy

$$(\Delta E_z)_{1\beta tron} << \frac{\gamma k^2 a^2}{emc}\frac{\lambda_\beta}{c} = (2\pi)^{\frac{5}{2}}(n_p\gamma)^{\frac{3}{2}}\frac{e^2}{\sqrt{mc}}a^2. \tag{4.43}$$

For typical afterburner or PWFA parameters, e.g. $n_p = 3\times10^{17}cm^{-3}$ and $\gamma = 6\times10^4$, (4.43) gives $(\Delta E_z)_{1\beta tron} << 1.8\times10^7 a^2(\mu m)GV/m$. This is well satisfied for typical beams with $\sigma_r \sim 1-10\mu m$.

To summarize, at the point A, $[b] << [c]$, and [c] can be written as in (4.41). The ratio of the perpendicular and longitudinal components of $\mathbf{F}_{rad}$ is

$$\frac{F_{\perp A}}{F_{//A}} = \frac{[a]}{[c]} = \frac{1}{\gamma^2 \alpha} << 1. \tag{4.44}$$

Note that it is not exactly zero. However, $\mathbf{F}_{rad}$ is dominantly in the $\hat{\mathbf{z}}$ direction at A.

Since $F_x = 0$ at point B, $\mathbf{F}_{rad}$ can be written out as

$$F_{radxB} = \tau_e(-\underbrace{\gamma k v_x}_{[a']} - \underbrace{\frac{\gamma^3}{c^2}\frac{dv_z}{dt}v_x F_z}_{[b']}) \tag{4.45}$$

$$F_{radzB} = \tau_e(-\underbrace{\gamma e \frac{dE_z}{dt}}_{[c']} + \underbrace{\frac{\gamma^3}{c^2}\frac{dv_x}{dt}v_x F_z}_{[d']}), \tag{4.46}$$

and using (4.35), we can get

$$|\frac{[b']}{[a']}| = \frac{e^2 E_z^2}{mc^2 \gamma k} = \frac{E_z^2}{2\pi n_p mc^2 \gamma} \tag{4.47}$$

For $n_p = 3 \times 10^{17} cm^{-3}$ and $\gamma = 6 \times 10^4$, this gives $|\frac{[b']}{[a']}| = 1.2 \times E_z^2(GV/m) \times 10^{-8}$, which is $<< 1$ for a typical PWFA case where $E_{zmax} \sim 10GV/m$. Using $v_{xB} = v_{xmax} = \frac{2\pi ac}{\lambda_\beta}$, [a'] can be rewritten as

$$[a'] = \gamma k \frac{2\pi ac}{\lambda_\beta} \tag{4.48}$$

Using (4.37),$v_{xmax} = \frac{2\pi ac}{\lambda_\beta}$ and $\frac{d\gamma}{dt} \approx \frac{eE_z}{mc}$. [d'] can be rewritten as

$$[d'] = \frac{4\pi \gamma^2 a^2 e^2 E_z^2}{mc\lambda_\beta^2} \tag{4.49}$$

and the ratio between [c'] and [d'] is then

$$\frac{[c']}{[d']} = \frac{mc\lambda_\beta^2 \frac{dE_z}{dt}}{4\pi^2 a^2 e \gamma E_z^2} \tag{4.50}$$

A similar analysis can be carried out to compare [c'] and [d'] as was done to compare [b] and [c] at point A. Here, in order for $[c'] << [d']$, $(\Delta E_z)_{1\beta tron}$ needs to satisfy

$$(\Delta E_z)_{1\beta tron} << \frac{4\pi^2 a^2 E_z^2 e\gamma}{mc^2\lambda_\beta} = (2\pi)^{\frac{3}{2}}(n_p\gamma)^{\frac{1}{2}}(eaE_z)^2(mc^2)^{-\frac{3}{2}} \tag{4.51}$$

For $n_p = 3\times10^{17}cm^{-3}$ and $\gamma = 6\times10^4$, this gives $(\Delta E_z)_{1\beta tron}(GV/m) << 0.22a^2(\mu m)E_z^2(GV/m)$, which is satisfied by most beam particles in typical PWFAs with $\sigma_r \sim 1-10\mu m$ and $E_{zmax} \sim 10GV/m$, except those that travel right on the axis or where $E_z = 0$, which have a negligibly small number.

To summarize, at B, $[a'] >> [b']$ and $[d'] >> [c']$. [a'] and [d'] can be written as in (4.48) and (4.49) respectively. Therefore the ratio of the perpendicular and parallel components at B is

$$\frac{F_{\perp B}}{F_{//B}} = \frac{[a']}{[d']} = \frac{kmc^2\lambda_\beta}{2\pi\gamma ae^2E_z^2} = \frac{(mc^2)^{\frac{3}{2}}}{eaE_z^2}\sqrt{\frac{2\pi n_p}{\gamma}} \tag{4.52}$$

For $n_p = 3\times10^{17}cm^{-3}$ and $\gamma = 6\times10^4$, this gives $\frac{F_{\perp B}}{F_{//B}} = \frac{78}{a(\mu m)E_z^2(GV/m)}$ which could be on the order of 1 for $\sigma_r \sim 1-10\mu m$ and $E_z \sim 10GV/m$. However this relatively large angle of the radiation reaction force only occurs when the particle is crossing the axis (at point B), and does not change the fact that during most of the betatron oscillation period, the force remains mostly in the longitudinal direction. This can be seen by comparing $F_{\perp B}$ and $F_{//B}$ with $F_{//A}$.

$$\frac{F_{//B}}{F_{//A}} = \frac{4\pi^2e^2E_z^2}{k^2\lambda_\beta^2} = \frac{E_z^2}{2\pi mc^2\gamma n_p} \tag{4.53}$$

$$\frac{F_{\perp B}}{F_{//A}} = \frac{2\pi mc^2}{\gamma ka\lambda_\beta} = \frac{1}{ea}\sqrt{\frac{mc^2}{2\pi\gamma^3 n_p}} \tag{4.54}$$

With $n_p = 3\times10^{17}cm^{-3}$ and $\gamma = 6\times10^4$, these give $\frac{F_{//B}}{F_{//A}} = 1.2\times10^{-8}E_z^2(GV/m) << 1$ and $\frac{F_{\perp B}}{F_{//A}} = \frac{9.3\times10^{-7}}{a(\mu m)} << 1$ for typical a and E_z values.

Together with the fact that $F_{\perp A} << F_{//A}$ (from (4.44)),we can argue that for parameters of interest for the PWFA application, the radiation reaction force $\mathbf{F}_{rad}$ is mostly in the longitudinal direction during the betatron oscillation.

The question remains, in what direction should one apply the radiation reaction force, $\hat{\mathbf{z}}$, $\frac{\mathbf{v}}{|\mathbf{v}|}$, or in another direction. We can get a hint by considering the $F_z(E_z) = 0$ case. So long as $K^2\gamma x^2 >> 1$, then the force is along $\frac{\mathbf{v}}{|\mathbf{v}|}$. However, from (4.29), it is clear that as the particle approaches the $x = 0$ axis, the force is no longer along $\frac{\mathbf{v}}{|\mathbf{v}|}$. In addition, as shown above, this comparison is further complicated by the effects of the F_z. For current experiments at SLAC, radiation reaction only effects the energy spread and not the emittance. Therefore, we add the radiation reaction force along $\hat{\mathbf{z}}$. We have placed it along $\frac{\mathbf{v}}{|\mathbf{v}|}$ and seen no difference. However, for conditions expected in a future TeV collider, the direction of $\mathbf{F}_{rad}$ wil matter. In [72], the coupling between the motion in the x-z and y-z planes (e.g. the angular momentum in the rz plane) was neglected. An area for future work is to include the coupling between the two planes, and the corrections due to F_z.

In the next section, we examine the energy spread caused by radiation reaction for SLAC parameters by simply applying $\mathbf{F}_{rad}$ along $\hat{\mathbf{z}}$.

4.2.3 Effective electric field

From the previous two sections we found that for PWFA applications, the total radiated power can be expressed using (4.26) and the radiation reactive force is dominantly in the longitudinal direction. Therefore, it will be accurate enough to model the radiation reaction effect using an effective electric field in

the longitudinal direction which satisfies the following relation

$$\mathbf{E}_{eff} = -\frac{P_t}{qv_z}\hat{\mathbf{z}} \approx -\frac{P_t}{qc}\hat{\mathbf{z}} \tag{4.55}$$

where the particle velocity is assumed to be $+c\hat{\mathbf{z}}$. Under this assumption, (4.26) can be rewritten as

$$P_t = \frac{2}{3}\frac{e^2\gamma^2}{c}\frac{\mathbf{F}_\perp^2}{m^2c^2} \approx \frac{2}{3}\frac{e^2\gamma^2q^2}{m^2c^3}[(E_x - B_y)^2 + (E_y + B_x)^2] \tag{4.56}$$

Therefore the effective electric field is

$$\mathbf{E}_{eff} = -\frac{2}{3}\frac{e^2\gamma^2q}{m^2c^4}[(E_x - B_y)^2 + (E_y + B_x)^2]\hat{\mathbf{z}}. \tag{4.57}$$

In QuickPIC, this effective electric field is calculated for each beam particle at every 3D update, and added to the total electric field inside a particle pusher (total electric fields outside the particle pusher remain unchanged).

It is worth noting that using the above method requires the consistency of the radiation reaction force formula (4.12) and the relativistic Larmor formula. As noted earlier, this has been confirmed by checking $\mathbf{F}_{rad} \cdot \mathbf{v} = -P_t$[74].

4.2.4 Energy spectrum broadening – code test

The major effect of the radiation reaction in current PWFA experiments is the broadening of the energy spectrum due to the energy loss of particles undergoing betatron oscillation at large radii. Fig. 4.9 compares the $p_z - z$ phase space of a beam with and without the radiation reaction. The parameters used here are $N_b = 1.87\times10^{10}$, $\sigma_r = 10\mu m$, $\sigma_z = 32\mu m$, $\varepsilon_{Nx} = 50mm{\cdot}mrad$, $\varepsilon_{Ny} = 5mm{\cdot}mrad$, $\gamma_0 = 55800$, $n_p = 2.8 \times 10^{17}cm^{-3}$ and the beam has been propagating in the plasma for $s \approx 55cm$. It's worth noting here that these plots use a log scale and the number of particles at the lowest energy are actually very few. From this

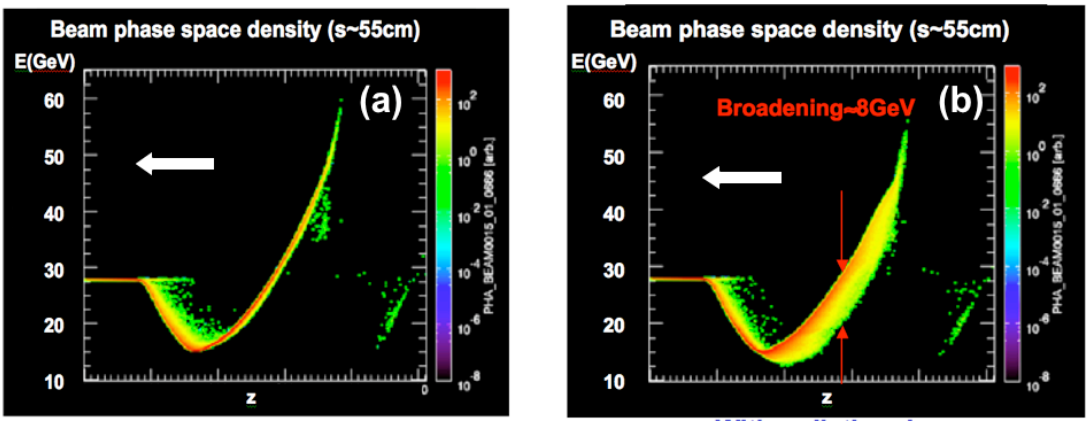

Figure 4.9: Beam density in phase space pz-z at s=55cm (a) with radiation reaction turned off (b) with radiation reaction turned on.

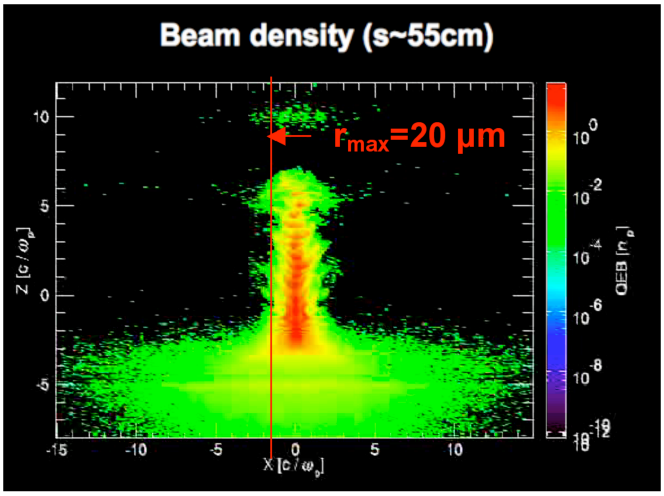

Figure 4.10: Beam density in configuration space x-z at s=55cm with radiation reaction turned on.

plot, the energy broadening is around, $\Delta E = 8GeV$, in this case. This is $\sim 50\%$ of the energy gain/loss of these electrons.

To check the plausibility of this value of broadening, we estimate the energy radiated by the particles at the largest radius ($r \approx 20\mu m$ as shown in Fig. 4.10) using the formula derived in [75] appendix B (where $P = \frac{2e^2\gamma^4}{3c^3}\dot{\mathbf{v}}^2$, i.e. $\mathbf{v} \perp \dot{\mathbf{v}}$ is assumed).

$$\Delta E_{rad} = N \int P dt = \frac{s}{\lambda_\beta} 7.08 \times 10^{-42} \times \gamma^{2.5} \times n_p^{1.5}(cm^{-3}) \times a^2(\mu m)(GeV) = 7.6GeV \tag{4.58}$$

where $\lambda_\beta = 2.11cm$ and $a = 20\mu m$ are used. One could also use (4.16) by rewriting it as

$$\frac{\Delta E_{rad}}{GeV} \approx 1.5 \times 10^{-6} (\frac{\gamma mc^2}{50GeV})^2 (\frac{n}{10^{16} cm^{-3}})^2 (\frac{r}{1\mu m})^2 \times \Delta s(cm). \tag{4.59}$$

For $\Delta s = 55cm$, $r = 20\mu m$, $n = 2.8 \times 10^{17} cm^{-3}$ and $\gamma mc^2 = 28.5GeV$, this gives $\Delta E = 8.4GeV$. These values agree with the simulation observation.

4.3 Realistic beam/plasma parameters

Modeling afterburner relevant experiments requires some realistic beam/plasma parameters that was not already built in the code. Several changes were made to meet these requirements.

4.3.1 Twiss-initialized beams

Since the beams are normally focused several centimeters into the plasma oven (instead of at the entrance), they need to be initialized using twiss parameters in the transverse direction. The phase space coordinates are generated using the Monte Carlo method based on the action-angle variables[76]. Another equivalent

method and one that is used in OSIRIS is to initialize them at the focus and then free stream them to the desired entrance point. This can be done independently for each plane. In order to minimize noise (quiet-start), particles are generated in pairs that are symmetric about (0,0) in phase space. Fig. 4.11 shows an example of a twiss-initialized beam propagating in vacuum. The parameters used here are $\gamma = 82192$, $\varepsilon_x = 124$, $\varepsilon_y = 13$, $\sigma_{rx0} = \sigma_{ry0} = 10\mu m$ ($\sigma_{rx0}, \sigma_{ry0}$ are beam spot sizes at waist). Therefore at $15cm$ before the waist, the twiss parameters are, $\alpha_x = 2.26$, $\alpha_y = 0.237$, $\beta_x = 40.6cm$, $\beta_y = 66.8cm$. The beam has a current profile as shown.

With the ability of twiss-initializing the beam, the effect of the beam waist location was studied. It was found that focusing the beam closer to the plasma oven entrance results in further propagation distance into the plasma before head erosion (see Chapter 7) disintegrates the beam and higher energy gain can be obtained at the beam tail[77].

4.3.2 Loading phase space data

For even more realistic beam parameters, 6D phase space data from a beam transport code (e.g. Elegant) can be loaded and redistributed to initialize the beam. Fig. 4.12 is an example for the future FACET (Facilities for Accelerator Science and Experimental Test Beams) beam parameters at SLAC. Here, the distribution function in each dimension is generated from the Elegant data and redistributed to appropriate number of simulation particles using the rejection-acceptance method [78]. It is assumed that there are no correlation between the 6D coordinates.

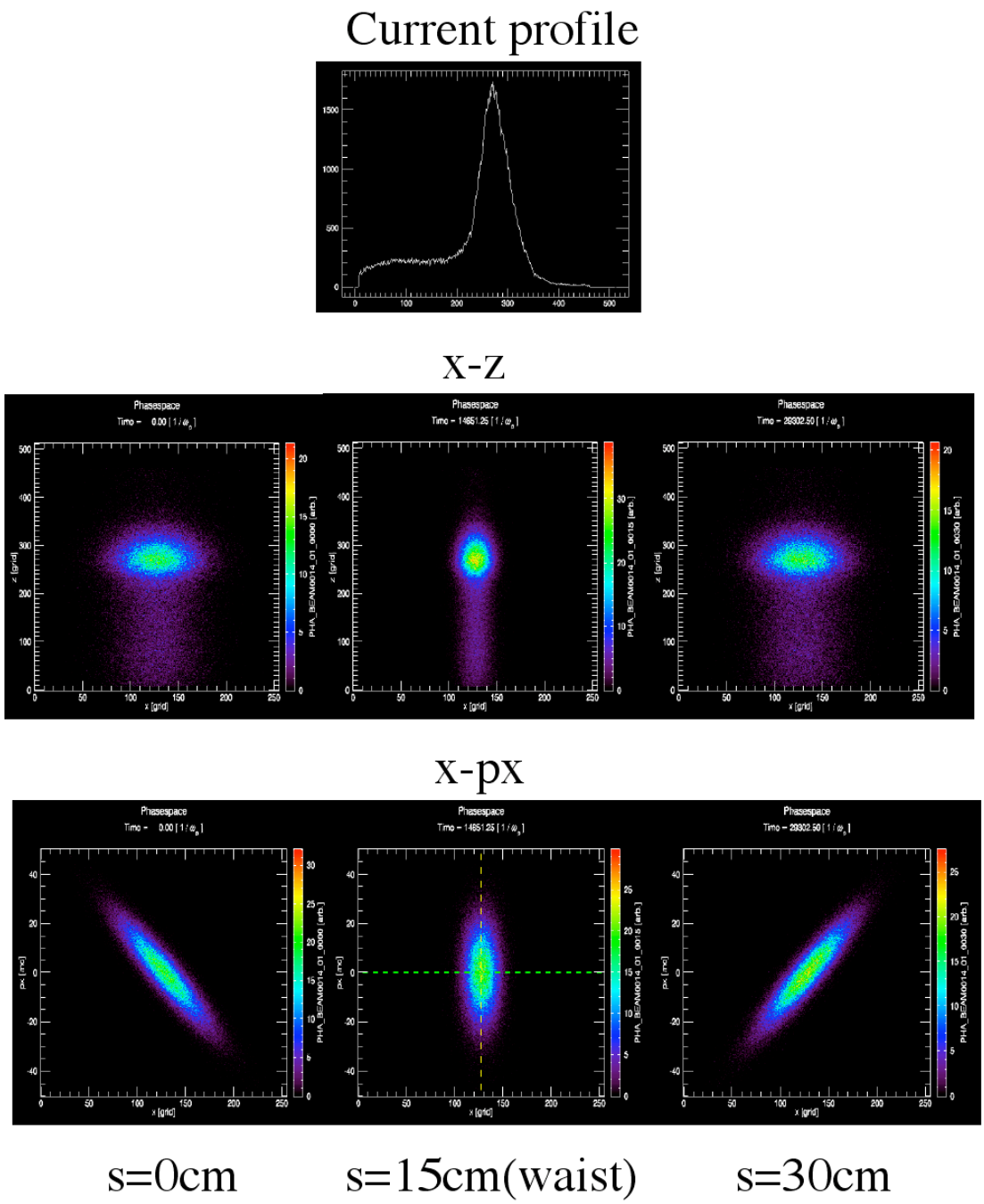

Figure 4.11: Vacuum propagation of a twiss-initialized beam

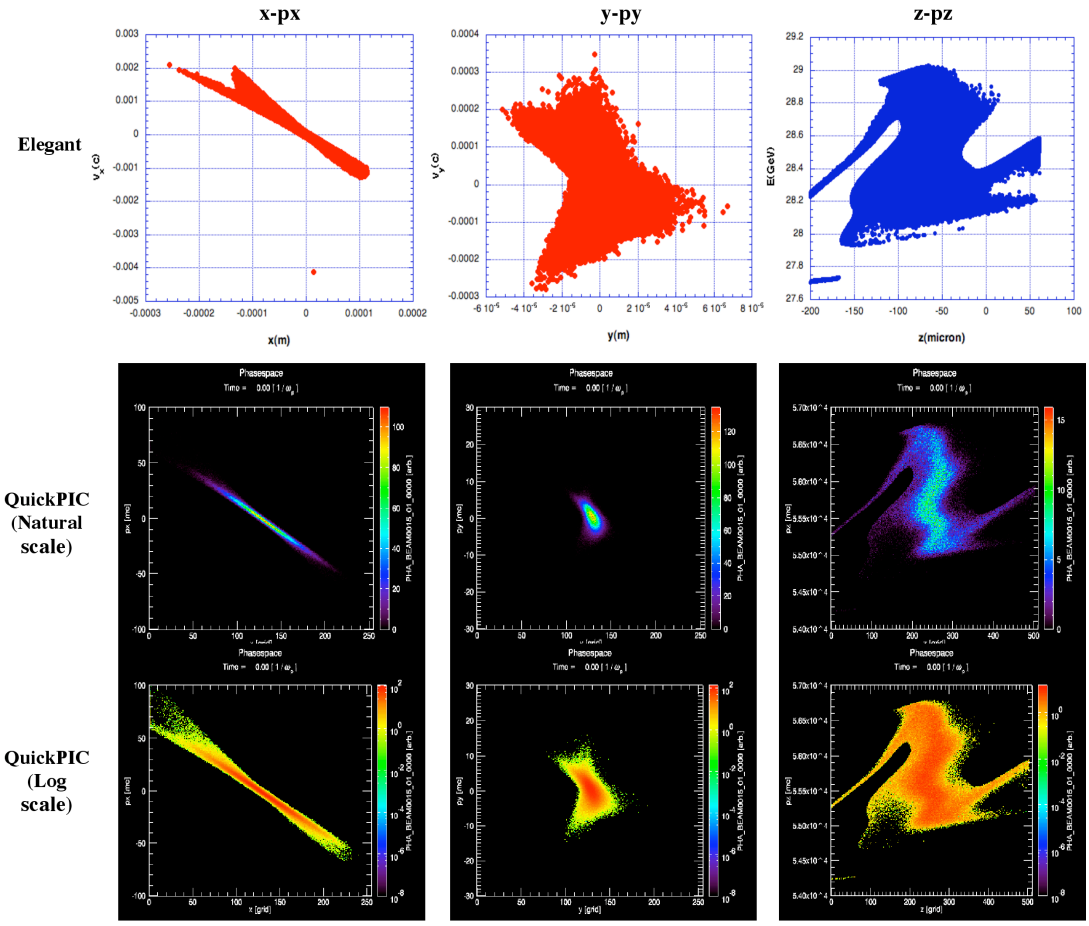

Figure 4.12: Initial beam phase space density in QuickPIC for FACET beam parameters by loading and redistributing data from Elegant

4.3.3 Plasma densities

As has been mentioned in the section 4.1, the code was changed so that the normalizing density can be arbitrarily chosen instead of being fixed to the pre-ionized plasma density. Moreover, multiple species of both neutral gases and pre-ionized plasmas (needed when modeling large contrast densities in different regions to maintain number of particles per cell) are implemented. These actual densities can be set independently. Each of these densities can vary as a function of propagation distance (which is the case in the experiment) and can have different transverse profiles, such as uniform, hollow channel, round column, half-space (plasma-vacuum boundary).

In the case of multiple neutral species, since the degree of ionization can be different for each type of gas, a power of contribution to the numerical diffusion coefficient can be assigned for each species. For example, in the transition region of the plasma oven where buffer gas helium confines the lithium vapor in the E167 experiments, the major contribution of wake formation is from lithium (helium is only ionized near the end of the wake bucket where the electric fields are largely enhanced due to the wake). In this case, since the actual plasma density is closer to the lithium density, the coefficient of the numerical diffusion coefficient of lithium can be set as 1 while that for helium can be set as 0. This indicates some pre-knowledge of ionization degree for each species which needs to be obtained from theoretical estimates or a few test runs.

4.4 Trapped particles

Due to the implementation of the quasi-static approximation, QuickPIC is not able to correctly model the trapped particles as 'plasma particles' since they

no longer satisfy $\frac{\partial}{\partial s} << \frac{\partial}{\partial \xi}$. One idea to remedy this is to 'promote' a plasma particle to a beam particle once it obtains a large enough velocity. However, how this promotion criteria is chosen (i.e. how large this 'large enough velocity' should be) requires careful consideration. Here we describe a simple criteria of promotion as a first attempt to implement this idea. Although the results are not satisfactory in terms of the accuracy of the wake, the code construction (which involves numerous additions and modifications) was completed. When the promotion criteria is refined and improved in the future, they can easily be implemented.

It is worth noting that the criteria of promoting a plasma particle to a beam particle (promotion criteria) is different from that of whether this particle is trapped (trapping condition). The trapping condition can be described by $v_{//} \geq v_\phi$, where $v_{//}$ is the axial velocity of the plasma particle and v_ϕ is the phase velocity of the wake. In order for a plasma particle to be accelerated from stationary to this trapped velocity, the propagation distance L_{trap} needed can be determined by $E_z \cdot L_{trap} = (\gamma_\phi - 1)mc^2$, where $\gamma_\phi \equiv \frac{1}{\sqrt{1-v_\phi^2/c^2}}$ and E_z is the accelerating wakefield (assumed to be constant, i.e. zero phase slippage). For a typical afterburner relevant experiment, $E_z \approx 50GV/m$ and $\gamma_\phi \approx 60,000$, this gives $L_{trap} \approx 60cm$. For comparison, the typical betatron wavelengths in these experiments are $\sim 2cm$, and the 3d time step (beam update) is typically $\sim 1mm$. This suggests that in order to model these trapped particles, they need to be tracked long before their velocity reaches v_ϕ. The most straightforward way to determine whether a plasma particles should be tracked (promoted) is whether it will stay in the moving simulation window in the next 3d time step according to its velocity. From Fig. 4.13, the promotion criteria can be expressded as $z^{n+1} = z^n + (c - v_{//}) \cdot \Delta t_{3d} < z_{max}$.

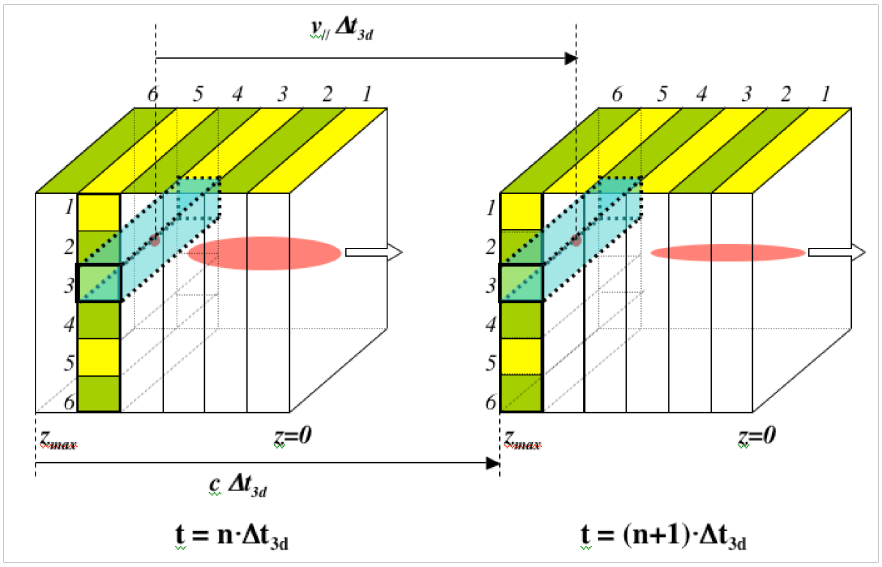

Figure 4.13: Criteria of 'promoting' a plasma particle to a beam particle.

The flowchart with this promoting algorithm is shown in Fig. 4.14. It should be noted here that the deposition of the 'trapped' particles from the previous 2d time step uses a similar method as depositing beam particles (direct deposition using area weighting) which is different from normal plasma species deposition (with the $\frac{1}{1-v_z/c}$ correcting term).

Due to the fact that the 2D and 3D part of the code are mixed together in this promoting algorithm, a significant number of changes in the code structure was involved. Some parameter sharing is required between the 2 parts of the code, e.g. the 3D part needs to know which of the plasma species include a 'promoting' algorithm so it can assign the correct number of 'beam' species; and the 2D part needs to know how large a 3D time step is in order to calculate the promotion criteria. Therefore, the method of preprocessing the input parameters (including broadcasting parameters between processors) needed to be changed. Another example of the complexity is that the plasma particles need to be moved to the

correct processor when being promoted to a beam particle because the 3D part is decomposed in the longitudinal direction (z) while the 2D part is 1D decomposed in one of the transverse directions (y) as shown in Fig. 4.13.

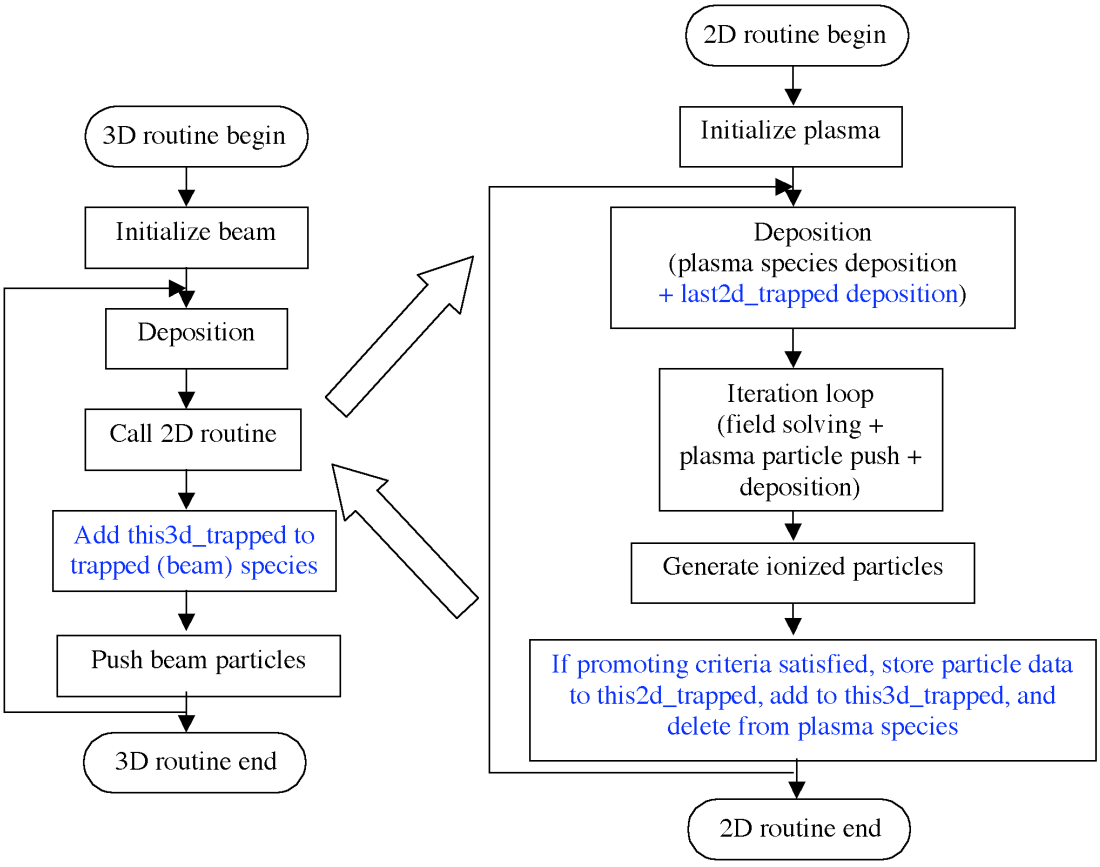

Figure 4.14: QuickPIC flowchart with added promoting algorithm (shown in blue)

Using the algorithm described above, several test runs were performed. The preliminary results were not satisfactory enough in terms of the accuracy of the wake structure. Those plasma electrons which are being promoted to beam electrons no longer come back to axis and the high density peak near the end of the bucket is absent in these simulations. This suggests that the promotion criteria is not selective enough (i.e. promoting these electrons too early). In the future

an improved criteria will be needed in order to better model trapped electrons.

CHAPTER 5

Electron Beam Wake Exciation in Field-ionized Plasmas

With the ability to model field-ionization using QuickPIC, we first explore the properties of the field-ionized wakes by comparing them with the pre-ionized ones. In this chapter, we examine the optimal densities in both cases and then find the criteria for a field-ionized wake to be similar to that of a pre-ionized one.

5.1 Optimal plasma/neutral density for wake excitation

To study the wakefield excitation in both pre-ionized and field-ionized regimes, the optimal plasma or neutral gas density that generates the largest wake is a fundamental and practical question of interest. Linear fluid theory in the wide beam limit gives the largest wake when $k_p\sigma_z = \sqrt{2}$. In non-linear regimes, this is not necessarily true even for pre-ionized wakes.

Here we examine this optimal density for a typical SLAC beam ($N_b = 1.87 \times 10^{10}$, $\sigma_r = 10\mu m$, $\sigma_z = 31\mu m$). Fig. 5.1 shows the peak accelerating field versus the plasma density (pre-ionized case) or the neutral lithium density (field-ionized case). In this plot, in order to avoid the arbitratriness when choosing the value of the useful field at the first accelerating peak, the spike values are plotted. Although this can be much larger than the useful field, the optimal density ob-

tained should be similar. We can see from the plot that for this beam, the optimal densities are larger than the linear theory prediction ($5.82 \times 10^{16} cm^{-3}$) in both pre-ionized and field-ionized cases. It is $\sim 4 \times 10^{17} cm^{-3}$ for the pre-ionized wake and $\sim 3 \times 10^{17} cm^{-3}$ for field-ionized wake. The later result agrees very well with the E164X experiment where the largest acceleration was observed.

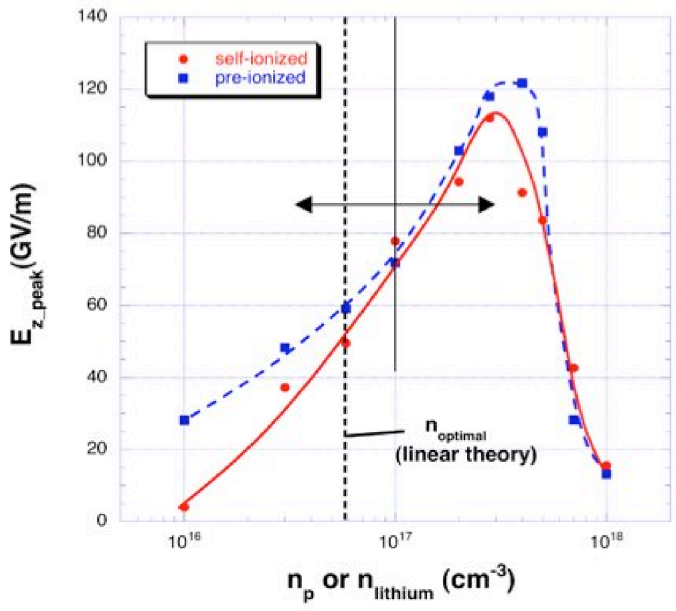

Figure 5.1: Peak accelerating field under different plasma/neutral densities for an electron beam with $N_b = 1.87 \times 10^{10}$, $\sigma_r = 10\mu m$, $\sigma_z = 31\mu m$.

5.2 Pre-ionized wakes versus field-ionized wakes

When considering the differences between field-ionized wakes and pre-ionized wakes, we first examine the beam space charge field E_{rmax}. If this value is not significantly above the ionization threshold E_{th}, the neutrals will not be fully ionized around the beam and it is not surprising that the wake will degrade

compared with a pre-ionized one (as has been observed in some simulations[67]). However, $E_{rmax} \gg E_{th}$ still does not guarantee a wake similar to a pre-ionized one. This can be seen from Fig. 5.1. For this beam, with $E_{rmax} = 31GV/m \gg E_{th} \approx 5GV/m$, the field-ionized wakes are much smaller than the pre-ionized ones for the low densities while they are similar to the pre-ionized ones for the higher densities.

Wakes in field-ionized and pre-ionized plasmas can be similar or different for the same beam depending on the relative size of the blow out radius $R_{blowout}$ compared to the ionized plasma column radius R_{ionize} (represented by the density of the immobile ions). For a given beam, the ionized plasma shape is always similar near the beam head although it can widen later at different positions due to the enhanced electric fields of the plasma wakes (as schematically shown in Fig. 5.2). However, the blow-out radius varies a lot with the plasma density. The lower the plasma density, the higher the nonlinearity, thus the larger the blow-out radius. Figure. 5.3 plots both the pre-ionized and field-ionized plasma electron densities on top of the ionized column (from the field-ionized case) for density $1 \times 10^{16} cm^{-3}$ and $2.8 \times 10^{17} cm^{-3}$, respectively. In the low density case (Fig. 5.3(a)(b)), the blow-out radius exceeds the plasma column, preventing the blown-out electrons from forming a narrow sheath as in the pre-ionized case. Their different trajectories and resulting trajectory crossing leads to a much smaller density concentration when they come back to axis. Therefore, the wake is much smaller than for a pre-ionized case as shown in Fig. 5.4(a). In the higher density case (Fig. 5.3(c)(d)), since the blow-out radius is smaller than the ionized plasma column, the field-ionized wake is very similar to the pre-ionized one as shown in Fig. 5.4(b).

Figure. 5.5 compares the $R_{blowout}$ in the pre-ionized wakes and R_{ionize} at the

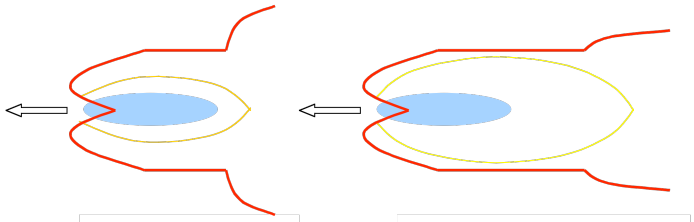

Figure 5.2: Schematic of widening of ion column due to wakefield

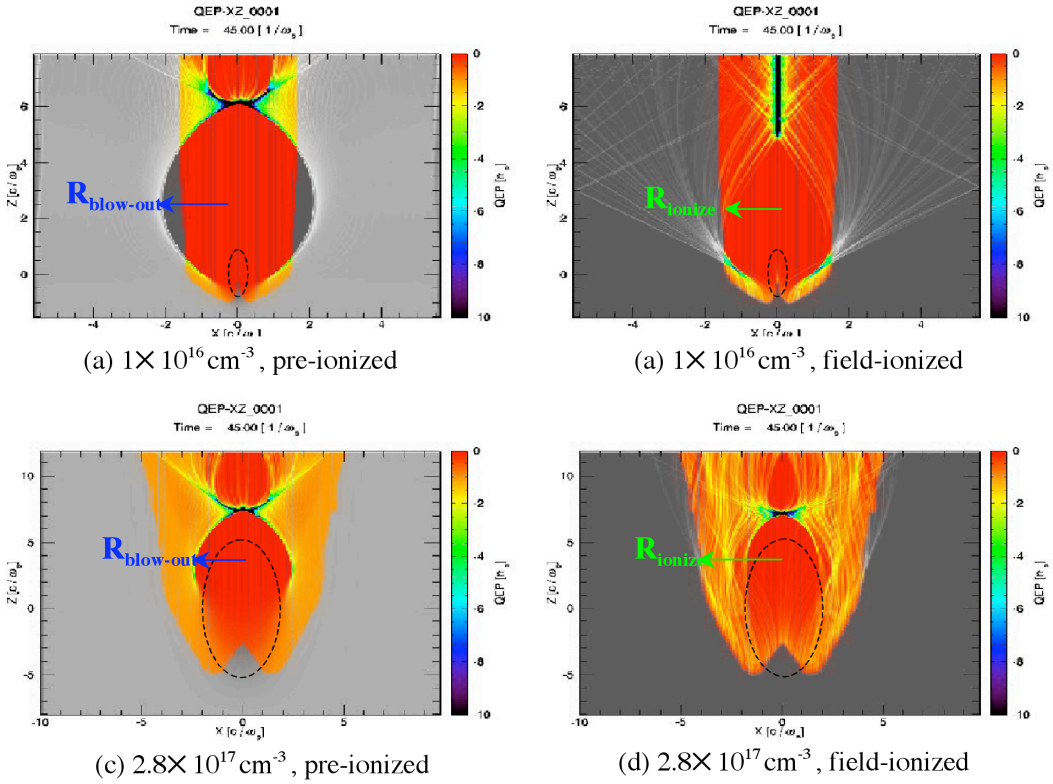

(a) $1\times10^{16}\,\mathrm{cm}^{-3}$, pre-ionized

(a) $1\times10^{16}\,\mathrm{cm}^{-3}$, field-ionized

(c) $2.8\times10^{17}\,\mathrm{cm}^{-3}$, pre-ionized

(d) $2.8\times10^{17}\,\mathrm{cm}^{-3}$, field-ionized

Figure 5.3: Plasma electron density and ionized column (a) low density, pre-ionized; (b) low density, field-ionized; (c) high density, pre-ionized; (d) high density, field-ionized

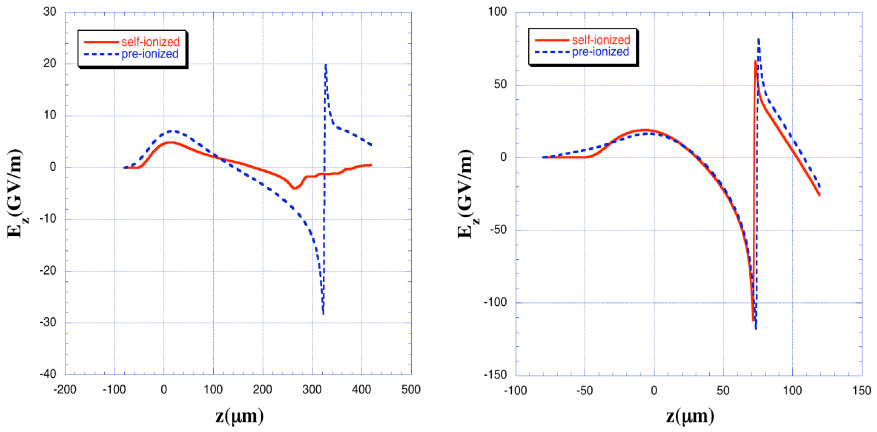

Figure 5.4: Comparison of pre-ionized and field-ionized wakes under (a) low plasma/neutral densitiy and (b) high plasma/neutral density

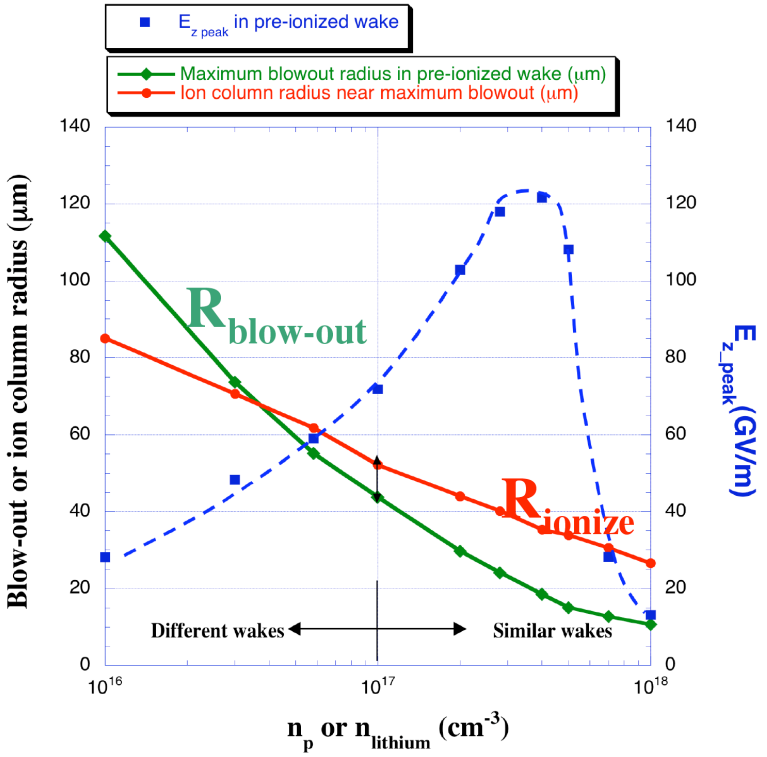

Figure 5.5: Ion column radius (red), pre-ionized blow-out radius (green) and pre-ionized peak wake amplitude (blue) for the E167 simulation beam

maximum blow-out position for different densities. As discussed above, R_{ionize} is a weaker function of the density (should be independent of the density if ionization due to the wake is ignored) while $R_{blowout}$ decreases rapidly with the density. When R_{ionize} exceeds $R_{blowout}$ by a certain amount (safety factor), the field-ionized wake should be similar to the pre-ionized one. Therefore, for a certain beam, there is a threshold density for similar pre-ionized and field-ionized wakes. Comparing Fig. 5.5 with Fig. 5.1, we can see the threshold density for this beam is around $1 \times 10^{17} cm^{-3}$. Since this density is smaller than the optimal density for the pre-ionized wake excitation ($4 \times 10^{17} cm^{-3}$), it is possible for this beam to achieve the maximum wake possible in pre-ionized cases through field-ionization.

In summary, in order to excite a field-ionized wake similar to a pre-ionized one, the ionized column needs to be not only larger than the beam size (i.e. $E_{rmax} \gg E_{th}$), but also the blow-out radius. For a certain beam with $E_{rmax} \gg E_{th}$, there is a threshold density n_{th} where this can be satisfied. If this n_{th} is smaller than the optimal density for pre-ionized wake excitation, then it is possible for this beam to achieve the largest pre-ionized wake through field-ionization.

CHAPTER 6

Modeling Afterburner Relevant Experiments

With field-ionization and radiation reaction modeled, as well as the ability to apply realistic beam/plasma parameters, QuickPIC is able to model the afterburner relevant experiments at SLAC. These simulations provide quantitative comparisons as well as important physical insights into the experiment. In this chapter, we will describe the details of the simulations that modeled the energy doubling experiment which was published in [2].

6.1 Experimental observations compared with simulation results

In this energy doubling experiment, the nominally 50-femtosecond-long electron beam containing 1.8×10^{10} particles is focused to a spot size of $10\mu m$ at the entrance of an 85-cm-long column of lithium vapour with a density of $2.7\times10^{17}cm^{-3}$. The nominally 42 GeV beam has a correlated energy spread of approximately $1.5GeV$, with electrons in the front of the beam at higher energies than those at the back. The beam energy exiting the plasma are measured as described in chapter 2. Fig. 6.1 shows one example of the electron energy distribution between 35 and 100GeV after traversing the plasma. The exiting angle at the plasma exit for this particular event was calculated to be smaller than $100\mu rad$, which is negligible; therefore energy relates directly to position. The highest electron energy

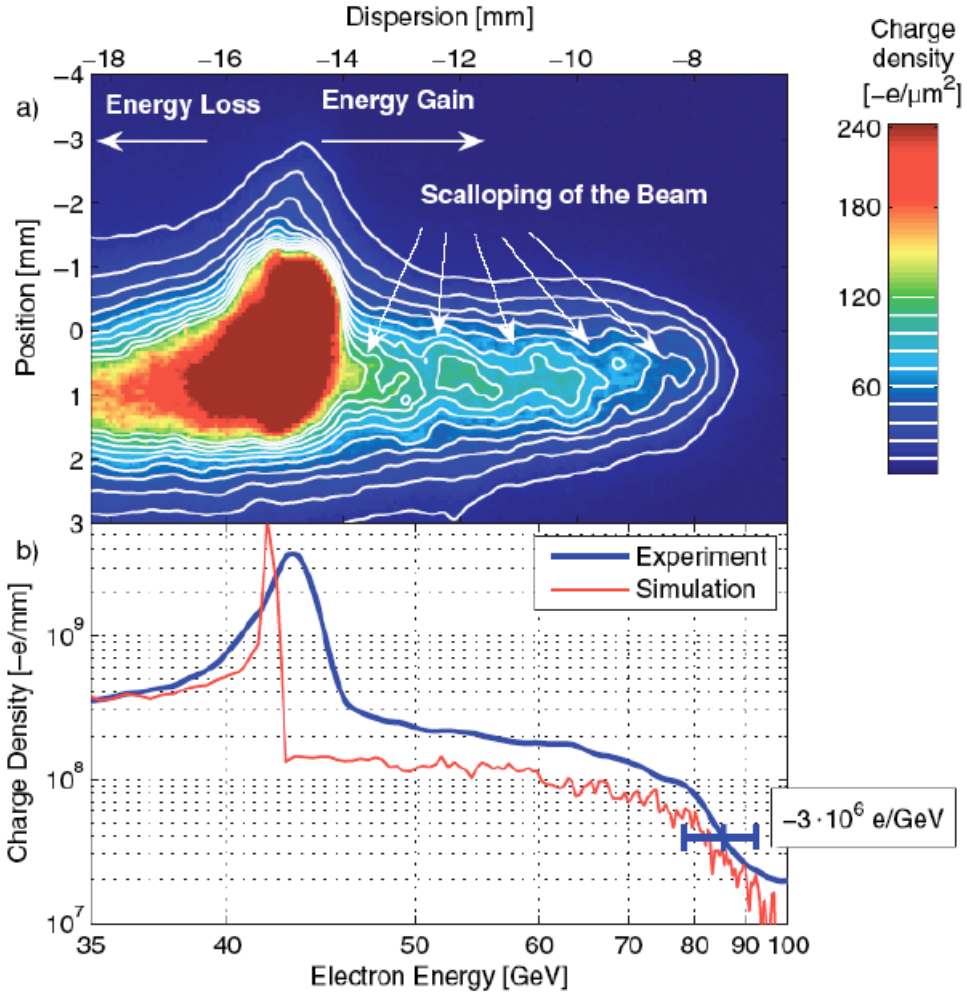

Figure 6.1: (a) Energy spectrum of the electrons in the 35 $\sim$ 100 GeV range as observed in the experiment. The dispersion (shown on the top axis) is inversely proportional to the particle energy (shown on the bottom axis). The head of the pulse, which is unaffected by the plasma, is at 43 GeV. The core of the pulse, which has lost energy driving the plasma wake, is dispersed partly out of the field of view of the camera. Particles in the back of the bunch, which have reached energies up to 85 GeV, are visible to the right. The pulse envelope exits the plasma with an energy-dependent betatron phase advance, which is consistent with the observed scalloping of the dispersed beam. (b) Projection of the image in (a), shown in blue. The simulated energy spectrum is shown in red. The differences between the measured and the simulated spectrum near 42 GeV are due to an initial correlated energy spread of 1.5 GeV not included in the simulations. The horizontal error bar is due to the uncertainty in estimating the deflection angle and the spot size of the beam.

is $85 \pm 7GeV$(as shown in Fig. 6.2), indicating that some electrons in the tail of the beam with an initial energy of $41GeV$ have more than doubled their initial energy. The implied peak accelerating field of $52GV/m$ is consistent with the fields previously measured in a 10-cm-long plasma[44], indicating that the energy gain is scalable by extending the length of the plasma at least up to $85cm$. With this plasma length, in a series of 800 events, 30% showed an energy gain of more than $30GeV$. Variations in the measured energy gain were correlated to fluctuations in the peak current of the incoming electron beam.

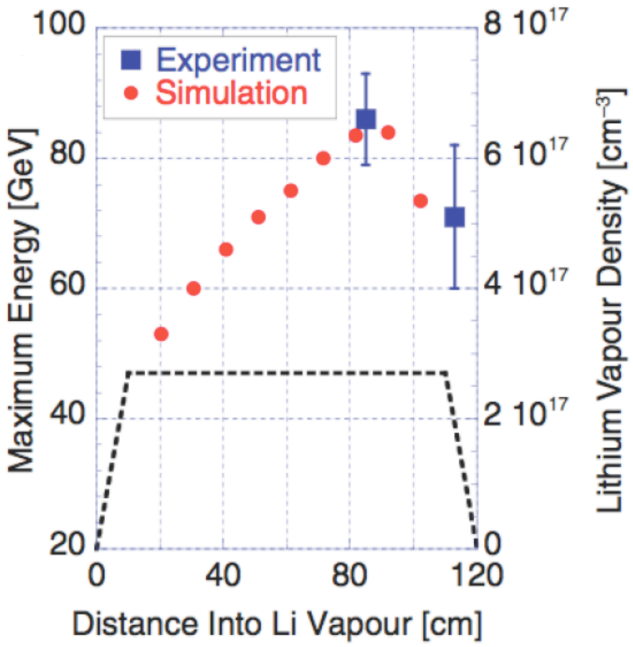

Figure 6.2: The maximum observed energy in the experiment (blue squares) for two different plasma lengths is compared to the energy of the particle bin containing 3×10^6 electrons per GeV (approximately the experimental detection threshold) in simulations (red dots) as a function of distance in the laboratory frame. Also shown is the lithium density profile used for the simulations (dashed line). Vertical error bars are due to the uncertainty in estimating the deflection angle and the spot size of the beam.

When the length of the lithium vapour column was extended from 85cm to

113cm, the maximum energy in an event with a similar incoming current profile was measured to be $71 \pm 11 GeV$ (as shown in Fig. 6.2). Less than 3% of a sample of 800 consecutive events showed an energy gain of more than 30GeV.

QuickPIC simulations were performed to model this experiment. The beam is initialized so that in vacuum, it would focus 15 cm beyond the start of the lithium vapour with a $\sigma_r = 10\mu m$ spot size (Fig. 6.3(a)). The longitudinal current profile is extracted from the LiTrack simulation that matches the experimentally measured beam spectrum produced by the SLAC accelerator. The resulting current profile approximates a gaussian ($\sigma_z \approx 15\mu m$) with a small tail (as shown in Fig. 6.3(b)). The computational grid forms a box xyz ($240\mu m \times 240\mu m \times 260\mu m$) in size. The number of grid points is $256 \times 256 \times 512$, respectively. We use 8.4 million particles for the beam and 2.6×10^5 particles for each 'slice' of lithium (i.e. 4 particles per cell). The beam electrons are advanced every $1.0mm$, which is 1/26th of a betatron wavelength for 42 GeV electrons in the flat density region.

Fig. 6.1(b) shows a comparison of the experimentally measured energy spectrum with one derived from the simulation. The quantitative agreement between the two spectra is good. In the simulation spectrum of Fig. 6.1(b), electrons are accelerated beyond 95GeV. In the experiment, the maximum detectable energy is determined by the spot size at the detection plane, and the highest detected energy is 85GeV. For the present case, this corresponds to a detection threshold of 3×10^6 electrons per GeV. The mean electron energy of the highest energy bin containing 3×10^6 electrons per GeV in the simulation is shown as a function of position along the plasma in Fig. 6.2. Also shown are maximum energies measured in the experiment at 85 and 113cm for similar electron current profiles.

In the following sections, we will discuss the details of modeling this experi-

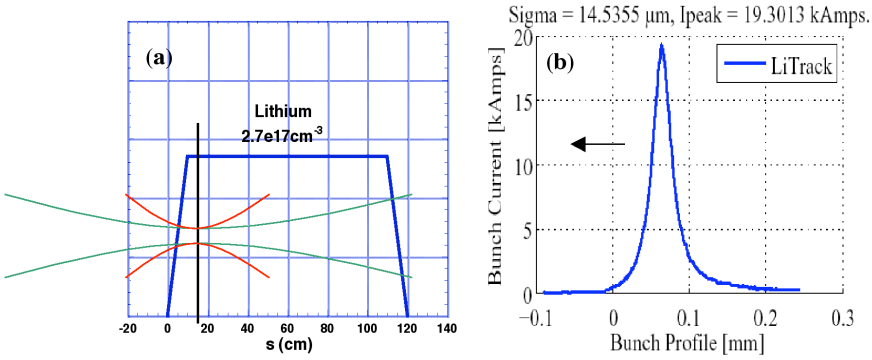

Figure 6.3: (a). Lithium density profile, beam waist at $s = 15cm$, (b). Beam current profile

ment, including the beam scalloping, beam head erosion, energy saturation, particle deflection, asymmetric emittance and the beam/plasma energy transfer.

6.2 Beam scalloping

In the Cerenkov image as shown in Fig. 6.1(a), scalloping of the beam body was observed. This is due to the different betatron phase advance for different longitudinal slices of the beam because their different energies. This feature has been predicted and explained by previous simulations but was clearly observed in the experiment for the first time due to the unprecedented energy gain. In this section, we will use a simple model to quantify the number of scalloping features observed.

As shown in Fig. 6.4, we assume at $s = L$, particles at $z = z_0$, z_1, z_2, ..., z_n are the adjacent locations that have the same betatron phase, and they have reached energis γ_0, γ_1, γ_2, ... γ_n, respectively. The shape of γ along z resembles the opposite of the wake E_z. Location z_0 is where $E_z = 0$ and γ_0 is the initial beam energy and keeps constant; other γ_ns are functions of propagation distance,

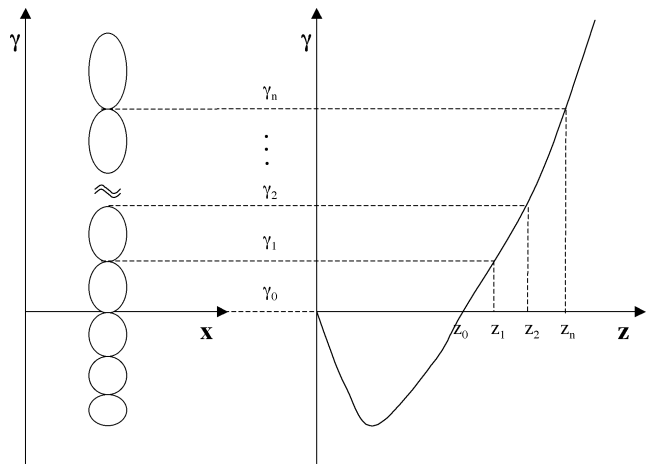

Figure 6.4: Schematic for beam scalloping due to different betatron advance.

i.e. $\gamma_n(s)$. Since the betatron wavenumber is related to γ through, $k_\beta \propto \frac{1}{\sqrt{\gamma}}$, then

$$k_{\beta n} = k_{\beta 0}\sqrt{\frac{\gamma_0}{\gamma_n(s)}} = k_{\beta 0}\sqrt{\frac{\gamma_0}{\gamma_0 + \alpha_n \cdot s}}, \tag{6.1}$$

where $\alpha_n = \frac{\gamma_n - \gamma_0}{L}$ is the rate of γ increase at z_n and is assumed to be independent of s. Then, the number of envelope oscillations at z_0 is

$$N = \frac{1}{2\pi}\int_0^L k_{\beta 0} ds \cdot 2 = \frac{k_{\beta 0} L}{\pi} \tag{6.2}$$

and that at z_n is

$$N - n = \frac{1}{2\pi}\int_0^L k_{\beta n}(s) ds \cdot 2 = \frac{1}{\pi} k_{\beta 0}\sqrt{\gamma_0}\frac{2}{\alpha_n}[\sqrt{\gamma_n} - \sqrt{\gamma_0}] = \frac{2\sqrt{\gamma_0}N}{\sqrt{\gamma_n} + \sqrt{\gamma_0}} \tag{6.3}$$

Therefore, γ_n is related to γ_0 through

$$\gamma_n = (\frac{N+n}{N-n})^2 \gamma_0, \tag{6.4}$$

where $N = k_{\beta 0} L/\pi$. From this, we know that the spacing between adjacent 'scallop's is

$$\gamma_n - \gamma_{n-1} = [(\frac{N+n}{N-n})^2 - (\frac{N+(n-1)}{N-(n-1)})^2]\gamma_0, \tag{6.5}$$

and this increases with n.

For the energy doubling experiment, at $s = 85cm$, N is around 30 (for $n_p = 2.7 \times 10^{17} cm^{-3}$ and $\gamma_0 = 82192$, $\lambda_{\beta 0}$ is $2.6cm$. An equivalent s is chosen to be 80 cm to take into account of the 10 cm density ramp). According to Eq.(6.4), the energy at the 5th scallop above γ_0 should be $\gamma_5 = 1.96\gamma_0$, which agrees well with the Fig. 6.1(a) observation. This agreement confirms that the scalloping features observed are in fact due to the different betatron advance at different longitudinal slices.

6.3 Head erosion and energy gain saturation

The energy gain saturation observed in the experiment as shown in Fig. 6.2 can have several possible reasons, such as pump depletion or the hosing instability. However, the observed lowest energy of $5 \sim 7GeV$ and the absence of hosing from the Cerenkov image eliminates these possibilities. The simulation suggests that a new phenomena in the field-ionized plasma – ionization induced head erosion – is the limiting factor for this energy gain saturation.

Fig. 6.5(a) and (b) shows the simulation output at two different positions in the plasma. At a distance of 12.3 cm, the wake produced by the motion of the plasma electrons resembles that produced in a preformed plasma, because the ionization occurs near the very head of the beam. After 81.9 cm one can see the effect of beam head erosion is that the ionization front now occurs further back along the pulse. The reason for this ionization front recession is that the head of the beam expands because there is an insufficient focusing force, and as a result, the self-field of the beam drops below the ionization threshold at this location. It is worth noting that even though the wake is formed further back, the peak

accelerating field still occurs at approximately the same position along the pulse. The transverse size of the pulse ahead of the ionization front is so large that the local beam density has dropped below the useful range in the color table.

Fig. 6.6 shows the evolution of the plasma density and the longitudinal wake at several different distances. We can see that due to head erosion, there is no significant wake left after 102 cm when the whole beam is eroded away and no filed-ionization happens any more.

The beam energy spectra binned to number of electrons per GeV are plotted in Fig. 6.7 at different propagation distances. The experimental detection threshold of 3×10^6 electrons per GeV (shown in black line) was used to determine the highest detectable energy plotted in Fig. 6.2. It can be seen that the highest energy was achieved between 82 to 92 cm. The energy loss stopped beyond 102 cm, agreeing with the disappearance of the wake. However, the number of particles continued to drop due to particles leaving the simulation window (see next section).

An identical simulation except with a pre-ionized plasma was performed to check the effect of beam head erosion. Fig. 6.8 compares the beam/wake evolution of these two cases. We can see that these two simulations share some common features such as similar blowout structure and wakes (Fig. 6.9). However, beam head erosion is absent in the pre-ionized plasma in this case. Fig. 6.10 shows the energy measured at the detection threshold for both cases. The overall lower value in the field-ionized case is due to the slightly narrower accelerating field at the very peak. It is obvious that beam head erosion in the field-ionized plasma is the limiting factor for further energy gain from the wake.

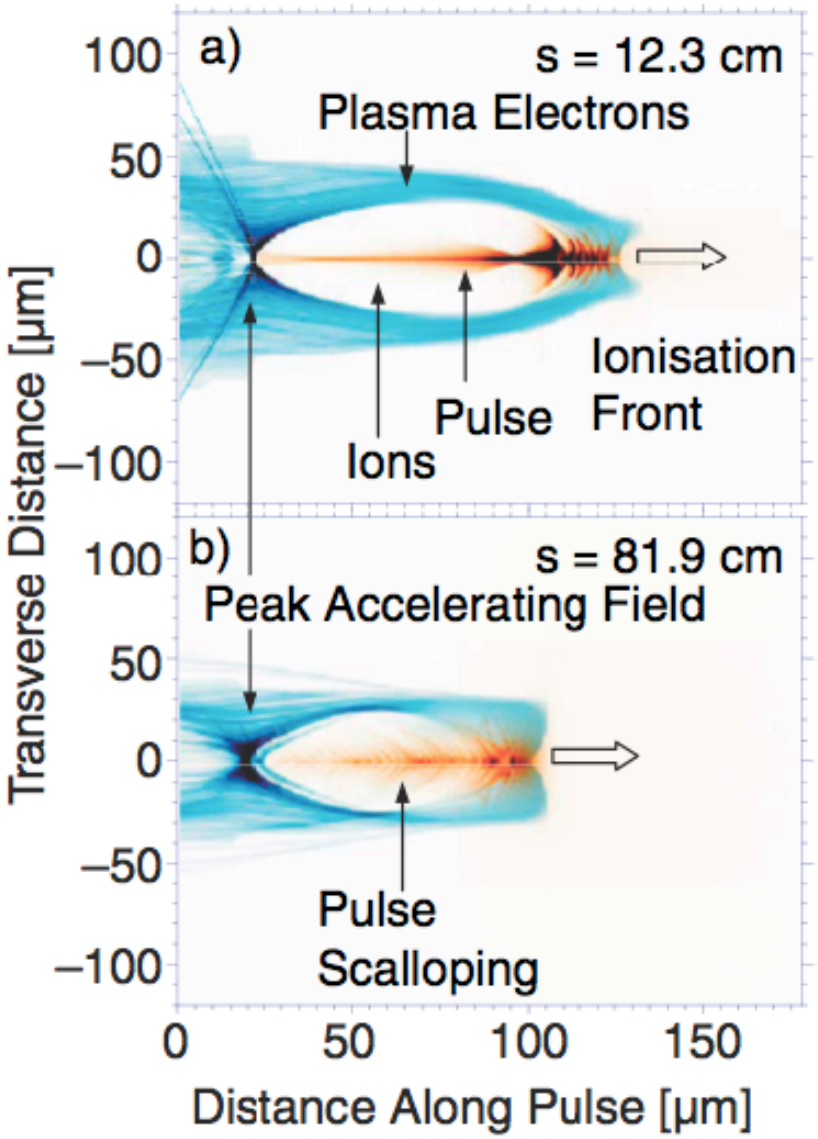

Figure 6.5: The density of the electron pulse (brown) and the plasma electrons (blue) at the distance the beam pulse has propagated s = 12.3 cm (a) and 81.9 cm (b) into the plasma on a plane (y = 0) through the center of the simulation box. The pulse travels from left to right. Recession of the ionization front is observed in (b).

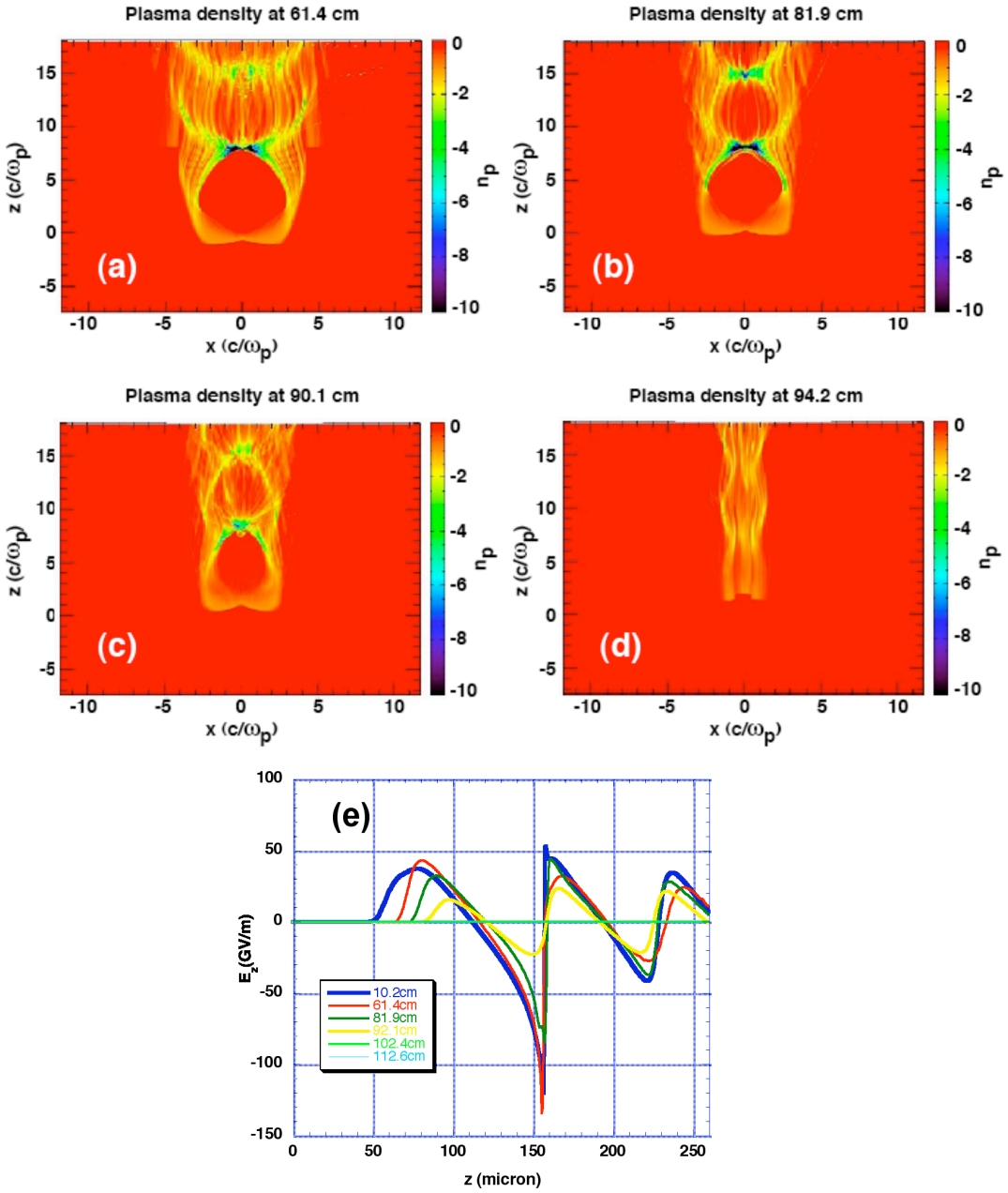

Figure 6.6: Plasma densities near the end of the lithium-vapour column. Color-scale images of the electron density in unit of the background plasma density ($n_p = 2.7 \times 10^{17} cm^{-3}$) on the y=0 plane (center of the moving, 3D simulation box) at distances towards the end of the lithium vapour column: (a) s = 61.4 cm; (b) 81.9 cm; (c) s = 90.1 cm; and (d) 94.2.9 cm. (e) Evolution of the longitudinal wakefield on axis.

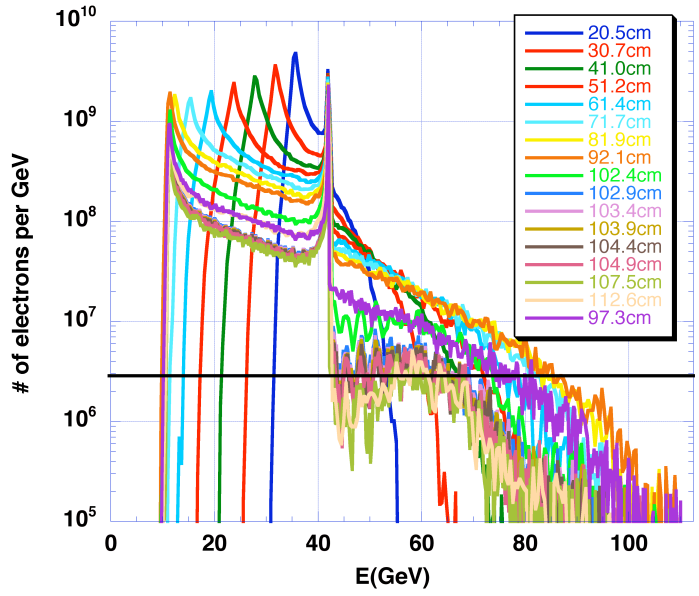

Figure 6.7: Beam energy spectrum at different propagation distances. 3×10^6 electrons per GeV (the rough experimental detection threshold) is shown in the black line.

6.4 Deflection of particles

From the previous section, we noticed the drop of the integrated number of particles in the energy spectra. The total number of electrons inside the simulation window is plotted in Fig. 6.11. The initial drop within the first $20cm$ is due to the deflection of electrons in the defocusing region, which moves forward behind the beam when the plasma density gradually increases. After the constant plasma density is reached (at $s = 15cm$), the total number keeps relatively constant. The drop starting around $s = 60cm$ is mainly due to the electrons at beam head diffracting and leaving the simulation window. This s distance roughly agrees with the beam $\beta_x^* = 8.2cm$ ($< \beta_y^* = 41cm$) and the box size in the x direction, i.e. $\sigma_{x0}\sqrt{1 + \frac{s^2}{\beta_x^{*2}}} \approx L_x$.

It is worth noting that the electrons immediately in front of the density peak at

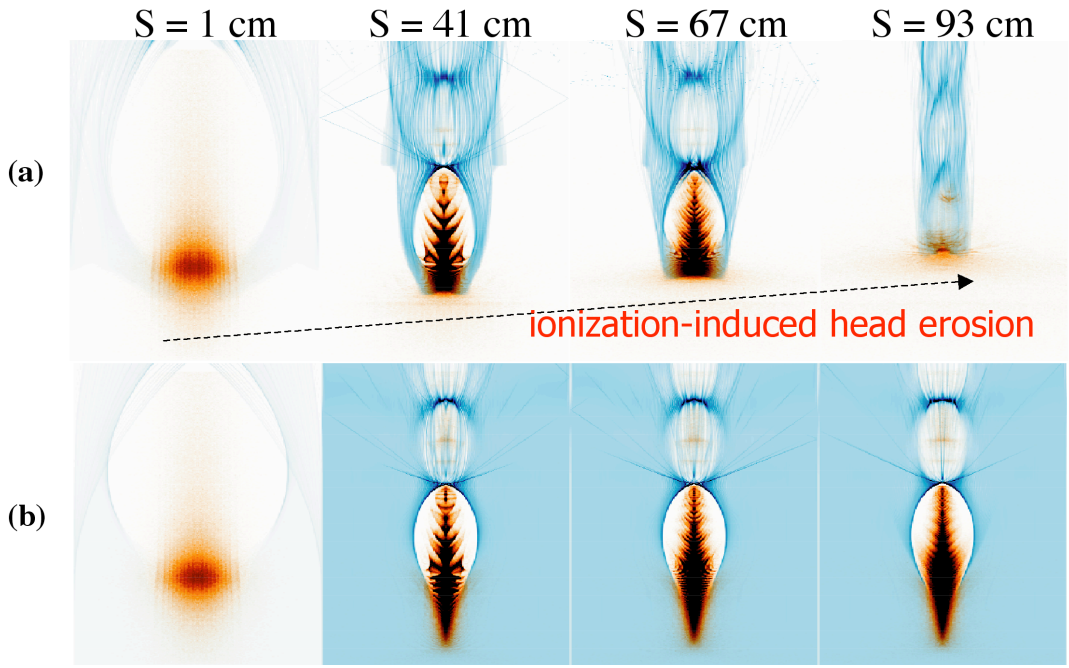

Figure 6.8: Beam and plasma density comparison for fied-ionized plasma (a) and pre-ionized plasma (b) for the energy doubling simulation.

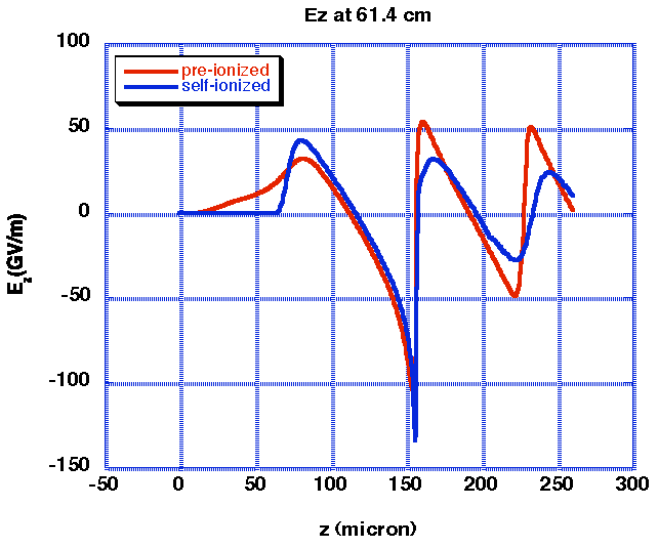

Figure 6.9: Comparison of longitudinal wakes on axis from pre-ionized and field--ionized plasmas before head erosion plays an important role.

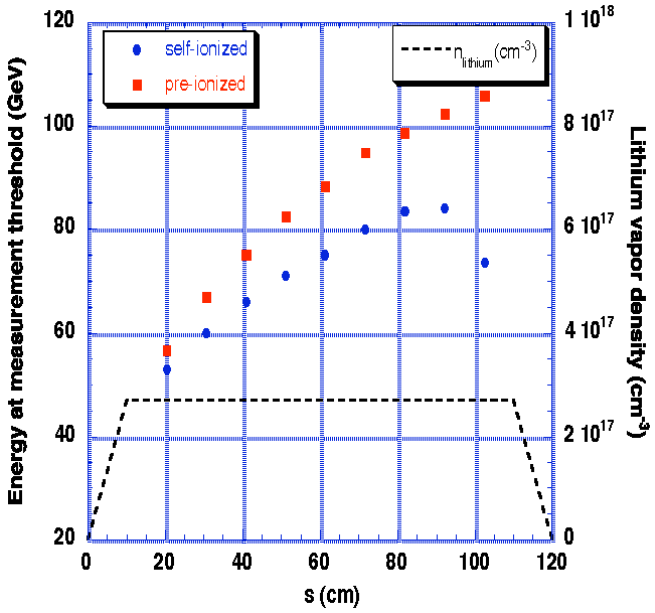

Figure 6.10: Comparison of energy gain (measured at 3×10^6 electrons per GeV) between pre and field ionized plasmas.

the end of the first bucket can be deflected after a certain distance of propagation and leave the simulation box too. Fig. 6.12 shows the beam density at $s = 81.9cm$ as an example (color in log scale). This deflection is due to the phase mixing of electrons resulting from the modified ionization front after the head erosion occurs.

Fig. 6.13 shows the details of this deflecting effect. Fig. 6.13(a) and Fig. 6.13(b) are the plasma densities at $s = 12.3cm$ and $81.9cm$, respectively. We can see that at $81.9cm$, the modified ionization front that resulted from head erosion has caused phase-mixing of electrons to occur. Quantities measured at the locations indicated by the colored lines are plotted in Fig. 6.13(c) to Fig. 6.13(f) in corresponding colors. The blue and red lines are at the same location which is right in front of the density peak; the purple and green lines are also at the same location and is about 1 micron away from the axis. Fig. 6.13(c) shows that

at $81.9cm$, a density peak from the phase-mixing electron is about $2 \times 10^{18} cm^{-3}$ (compared to the $2.7 \times 10^{17} cm^{-3}$ background plasma density) while at $12.8cm$, the density is zero indicating they are still inside an ion channel. Fig. 6.13(d) shows the defocusing field due to the phase-mixed electrons at $81.9cm$ and the linear focusing field at $12.3cm$ at these locations. Fig. 6.13(e) and (f) shows the effect of a small region which contains the highest energy particles transiting from the focusing region to the defocusing region after the phase-mixing of electrons occurs. (The spike of the purple line is due to the asymmetric blow-out channel, see next section).

Although the number of these deflected electrons is small, it is still an effect from the head erosion worth noting because these are the electrons that have been accelerated to the highest energies in the wake.

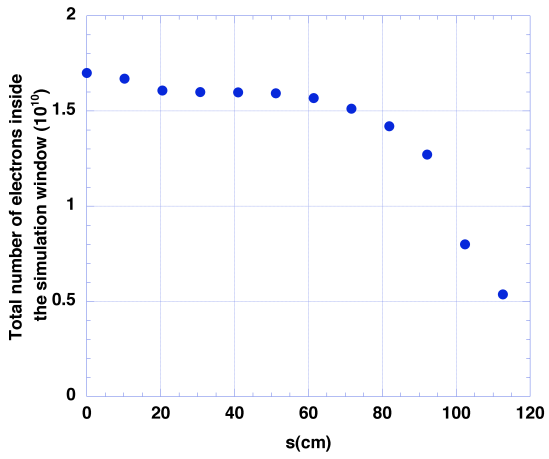

Figure 6.11: Evolution of the total number of electrons inside the simulation window.

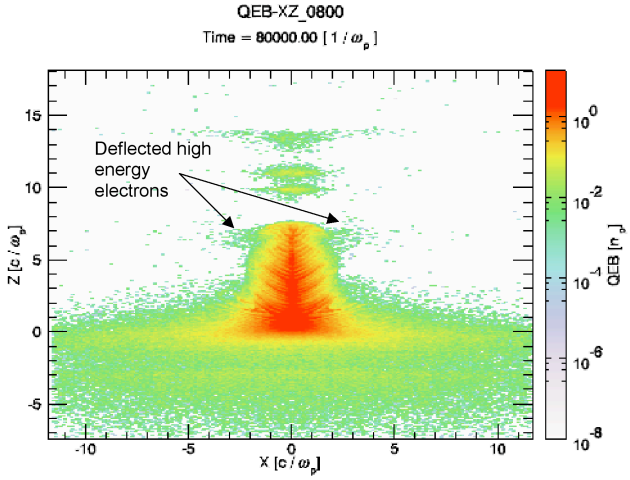

Figure 6.12: Beam density in x-z plane at y=0 slice (color in log scale) at s=81.9cm.

6.5 Influence of the asymmetric emittance

According to the nonlinear blow-out theory[23], the blow-out radius for a narrow beam ($k_p\sigma_r << 1$) is determined by the normalized charge per unit length of the beam. Therefore, asymmetric beam spot size does not necessarily lead to an asymmetric channel. However, when the beam spot size is not narrow enough, the channel can become asymmetric. Fig. 6.14 shows an example of such a wide beam. In this case, the plane with a wider spot size, $\sigma_x = 20\mu m$(left column), has a larger blow-out radius and the focusing field is smaller ($< 0.5\frac{mc\omega_p}{e}$) compared to that in the other plane ($> 0.5\frac{mc\omega_p}{e}$) with a smaller spot size of $\sigma_y = 5\mu m$. There is a spike in the focusing field at the focusing-defocusing transition region for the wider spot size plane and smooth transition angle for the narrower spot size plane (circled in Fig. 6.14(d) and (f)). As a comparison, for a same beam but with symmetric spot sizes ($\sigma_x = \sigma_y = 10\mu m$), the focusing field is symmetric ($\sim 0.5\frac{mc\omega_p}{e}$) and the transition region has an right angle (not shown).

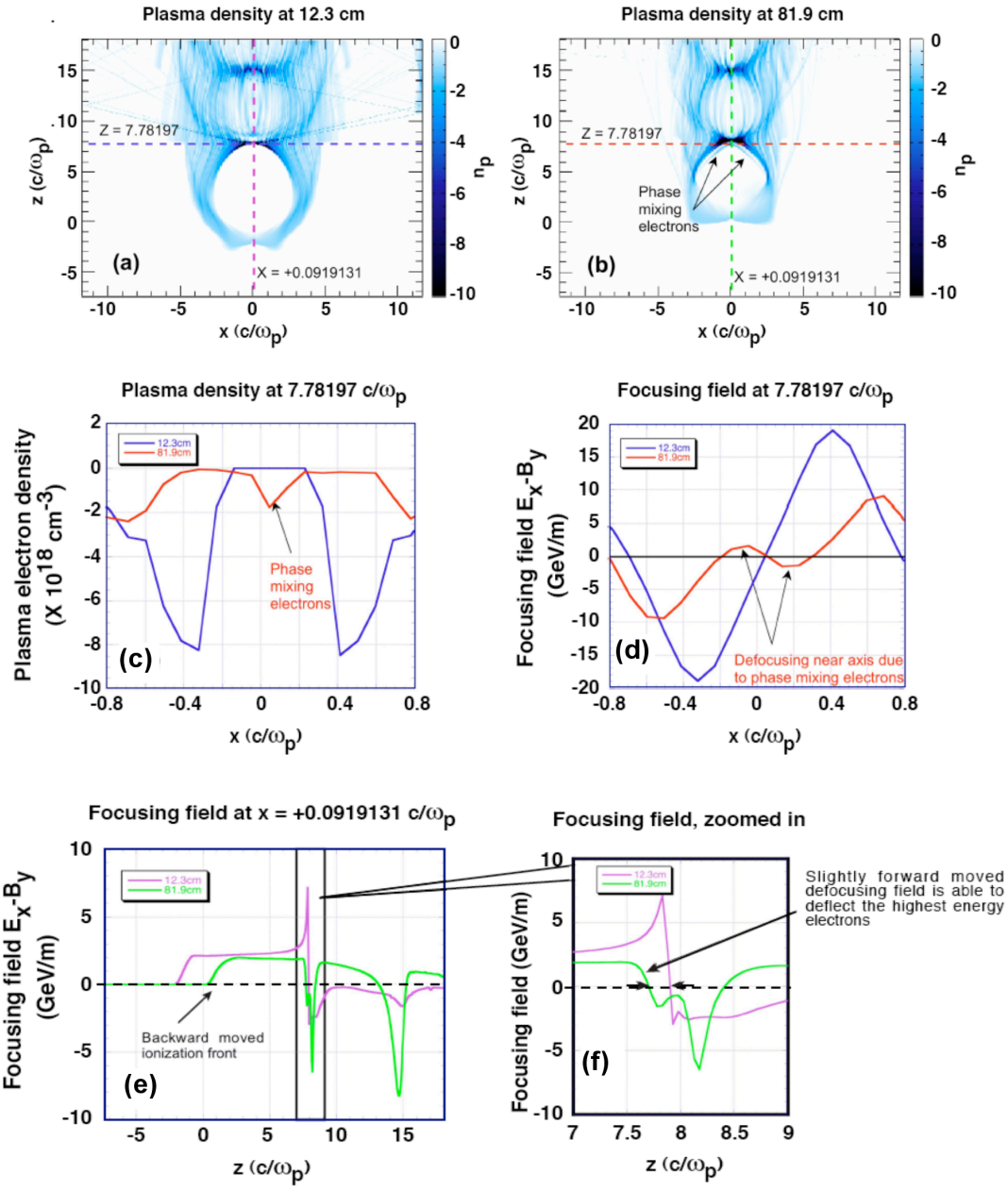

Figure 6.13: Beam density in x-z plane at y=0 slice (color in log scale) at s=81.9cm.

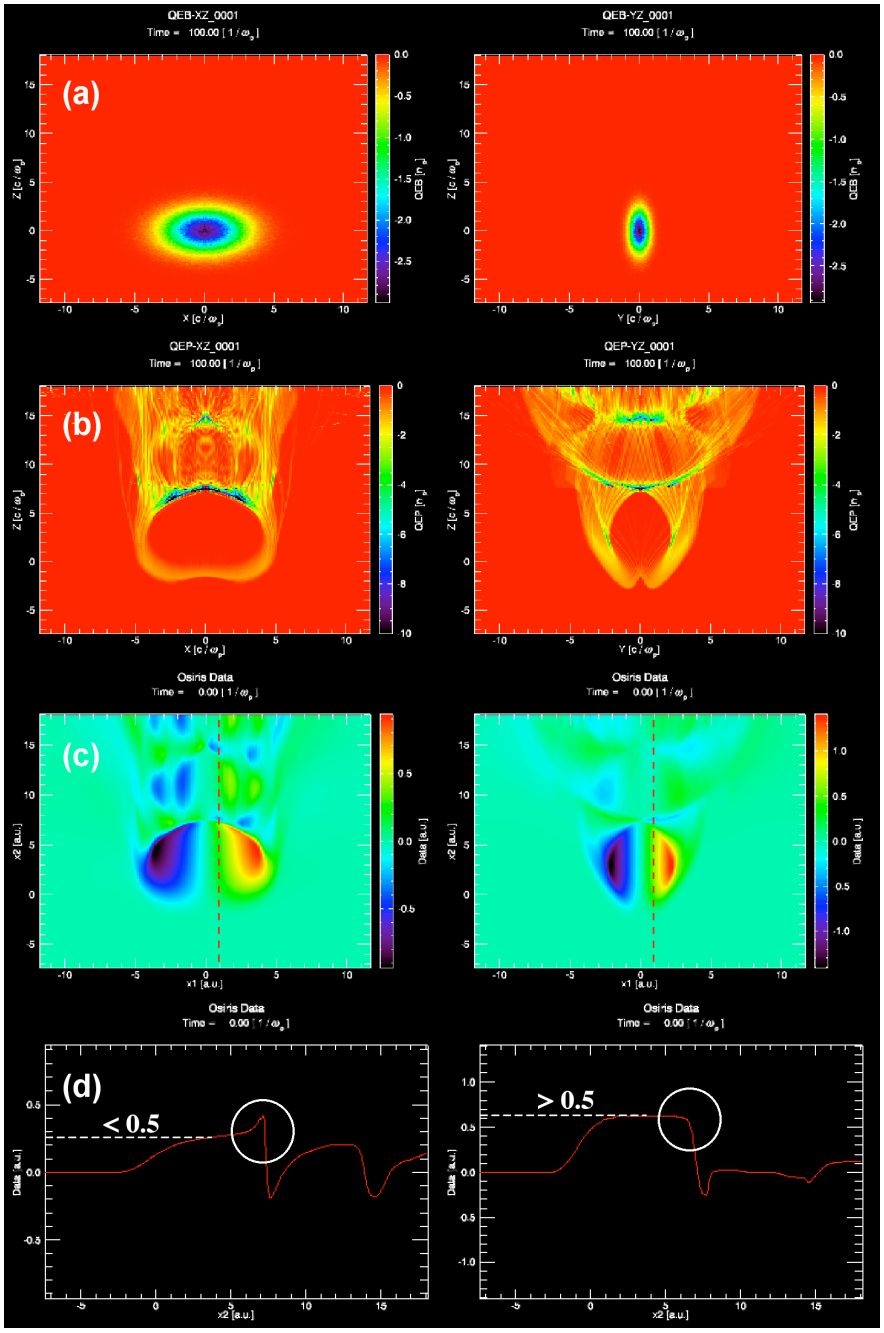

Figure 6.14: Example of asymmetric focusing beam $\sigma_x = 20\mu m$, $\sigma_y = 5\mu m$ (a) Beam density; (b) Plasma density; (c) Focusing field ($E_r - B_\theta$); (d) Lineout of focusing field at position shown in (c). The left column is the x-z plane and the right column is the y-z plane.

The spike in Fig. 6.13(e) suggests that there is an asymmetry in the blow-out channel for the energy doubling experiment simulation. This is due to the different emittances in x and y ($\varepsilon_{nx} = 100mm \cdot mrad$, $\varepsilon_{ny} = 20mm \cdot mrad$). Although the spot size at the beam waist is symmetric ($\sigma_{x0} = \sigma_{y0} = 10\mu m$), beam spot size in the x direction is in general larger due to the larger emittance. Fig. 6.15 compares the evolution of the r.m.s value of x and y for the beam center slice (i.e. z=0 in Fig. 6.13(a)(b)). Due to the focusing from the plasma ramp, the beam spot sizes pinch down to about $7\mu m$ and $3\mu m$ in x and y respectively. These spot sizes are small compared to the blow-out radius, therefore they only result in slight asymmetry of the ion channel. Fig. 6.16 shows the slightly larger channel radius in x direction at two different distances ($s = 12.3cm$ and $s = 81.9cm$). The focusing fields in the X-Z and Y-Z planes at $s = 12.3cm$ are shown in Fig. 6.17. The features are in agreement with the discussion from the previous paragraph.

Although there is only slight asymmetry in the focusing field, the effect does accumulate and show up over time. Fig. 6.18 compares the beam density ($x - z$, $y - z$) and phase space density ($x - p_z$, $y - p_z$) at $s = 41cm$. It can be seen that at this distance, more scalloping features due to the slightly larger focusing field in the y plane is already observable.

6.6 Beam plasma energy transfer

In this section, we discuss the energy transfer between the plasma and the beam in this simulation. Fig. 6.19 plots the percentage of total energy the beam lost as a function of the propation distance. We can see that at $s = 85cm$, the loss is about 50% of the initial beam energy (42GeV times 1.7×10^{10} electrons). This 50% can be attributed to two aspects, the beam synchrotron radiation and pump depletion into the plasma wake. The synchrotron radiation should not

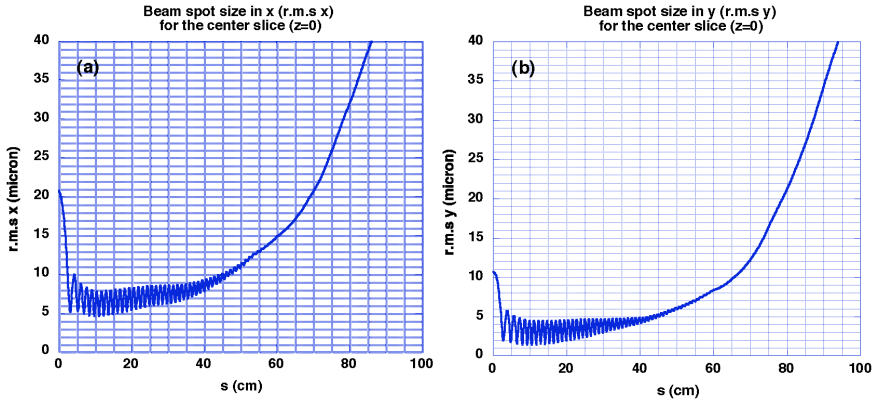

Figure 6.15: Evolution of beam spot size (r.m.s. value) in (a) x and (b) y direction at the beam center slice (z=0 in Fig. 6.12).

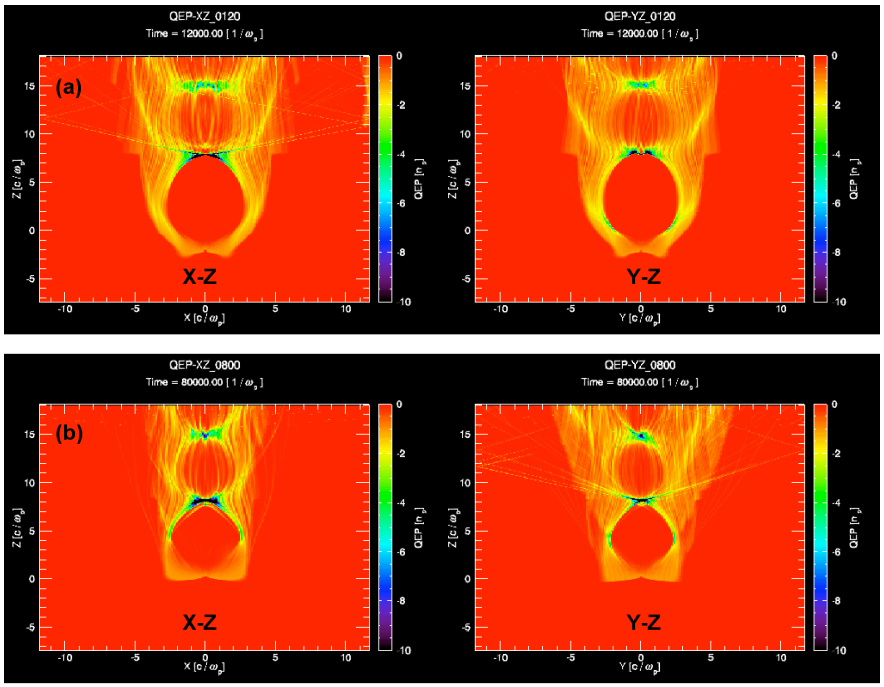

Figure 6.16: Plasma density in center X-Z plane and center Y-Z plane at (a) s=12.3 cm; (b) s=81.9cm.

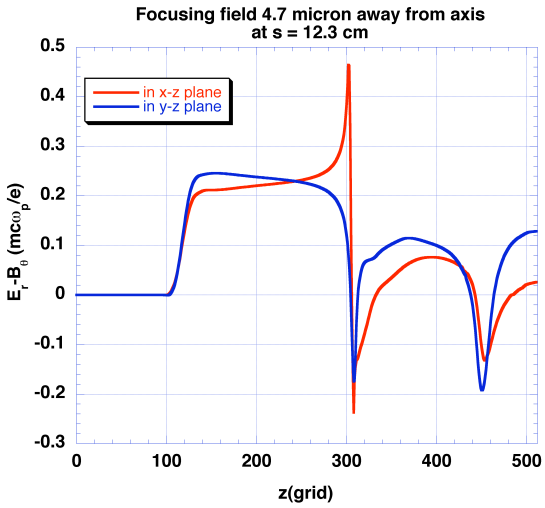

Figure 6.17: Lineout of focusing field $E_r - B_\theta$ at 4.7 micron away from axis in center X-Z plane and center Y-Z plane at s=12.3cm.

exceed $1 \sim 2GeV$ if averaged over all beam particles. (For a 42GeV electrons oscillating at 10 micron radius under $2.7 \times 10^{17} cm^{-3}$ density, radiated energy in $85cm$ is around $6GeV$). Therefore, synchrotron radiation loss is about $2 \sim 4\%$ of the initial total energy. The rest of the energy has been converted into the plasma wave. From energy conservation, this part of the energy should be $\sim 40 + \%$ of the initial energy.

main

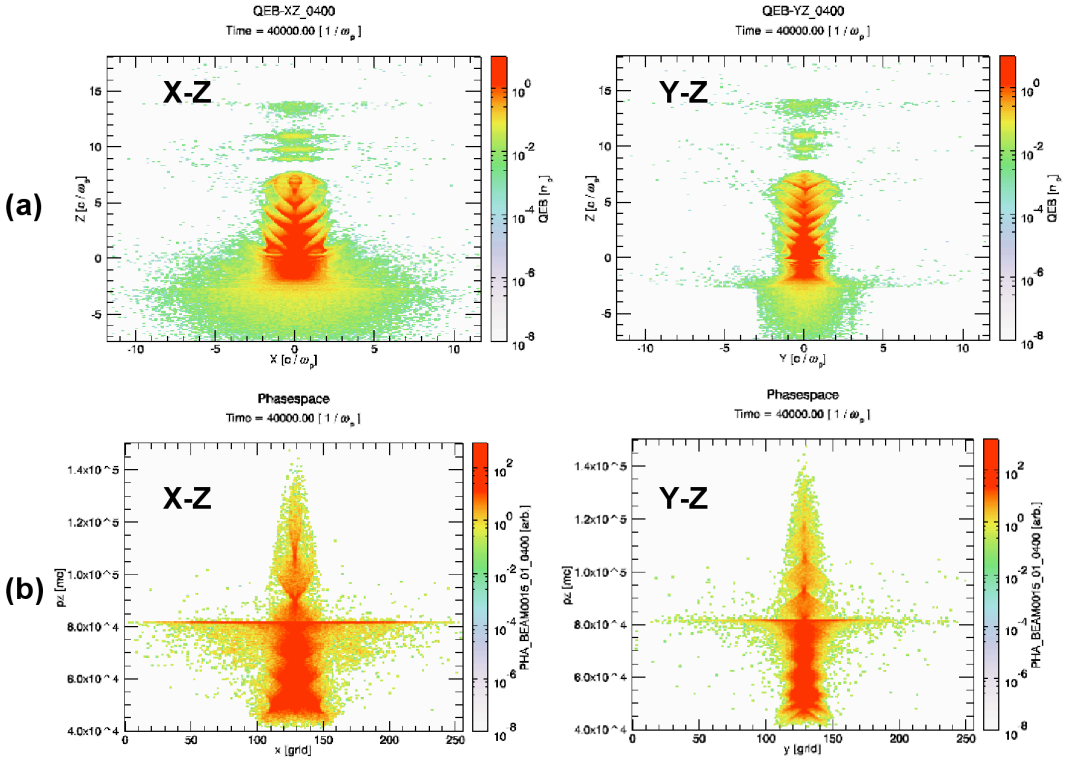

Figure 6.18: (a) Beam density at center X-Z plane and (b) beam phase space density in p_z v.s x plane. Both at $s = 41cm$.

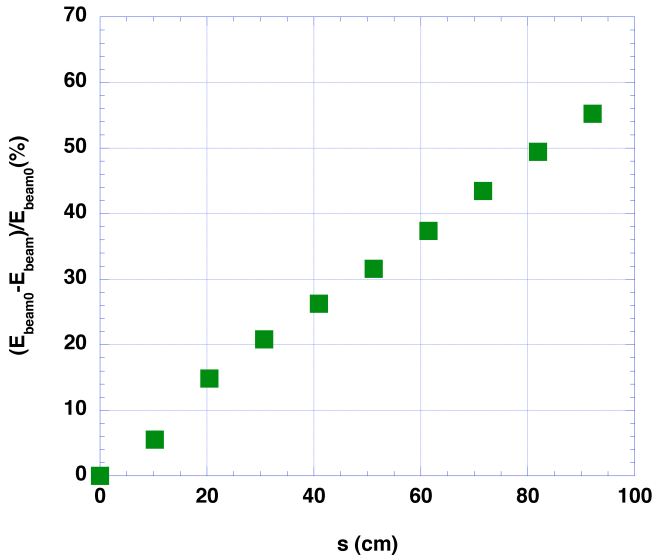

Figure 6.19: Percentage of total energy the beam lost as a function of the propation distance.

CHAPTER 7

Electron Beam Head Erosion in Field-ionized Plasmas

From the previous chapter, beam head erosion in the field-ionized plasma has been suggested by simulation to be the factor that limits further energy gain in the wakefield acceleration experiment. In this chapter, we will further study the mechanism and rate of this erosion through a theoretical model and simulations.

7.1 Beam head erosion study in literatures

Beam head erosion under different circumstances has been described in the literature. There are three categories for the erosion mechanism. They are the emittance driven erosion[79][80][81][82] due to the finite beam emittance; the ohmic dissipation erosion (or inductive erosion)[79][80][83] due to the beam energy loss in the wake; and the magnetic induced erosion [83] due to an external magnetic field. In some cases, more than one of these mechanisms occurs simultaneously. Under the conditions relevant to plasma wakefield acceleration where short and narrow bunches are used (the blow-out regime), the decelerating wakefield is not established yet at where the beam head expands, therefore, there is no inductive erosion. In current experimental conditions where there is no external magnetic field, the magnetic induced erosion is not of concern either. Therefore,

the only relevant mechanism of interest is the emittance driven erosion.

All the above mentioned work ([79] to [82]) are studied in pre-ionized plasmas. As we have seen, the erosion is exacerbated in field-ionized plasmas, and the rate is different. Reference [84] studies the inductive erosion and emittance driven erosion in an un-ionized or weakly ionized gas. However, in the study of ref. [84], even the beam body is under the charge neutralization regime ($n_b < n_p$), which is not the case of interest here and the conclusion that the emittance driven erosion slows down as the head radius becomes large under this condition is not true in the blow-out regime (see section 7.3). For the above reasons, it is necessary to establish a model and understand the emittance driven head erosion in a field-ionized plasma in the blow-out regime.

In the following sections, we will first examine the numerical parameters necessary for the erosion rate to converge. Then we will introduce a theoretical model, which is useful in estimating the erosion rate. Last, the estimates from this model will be compared with simulation results.

7.2 Head erosion simulation convergence test

A convergence test was performed to check the requirement of time resolution, Δs, in order to correctly model the erosion process. Fig. 7.1 plots the plasma density evolution under different time resolutions. The result suggests that resolving the betatron oscillation is necessary. In this test, updating the electron beam in a distance so that there are 10 steps per betatron oscillation for particles inside the ion channel gives almost identical erosion rate to that of 40 steps per oscillation. While under-resolving the betatron oscillation (e.g. 2.5 steps per oscillation) gives spuriously higher erosion rates. This is a reasonable

result since the erosion process involves the transition region where the focusing field increases from zero to ion channel focusing, which corresponds to the characteristic evolution distance from β^* (large) to λ_β (small). In all the simulations presented hereafter, the beams are updated at least 12 steps per λ_β.

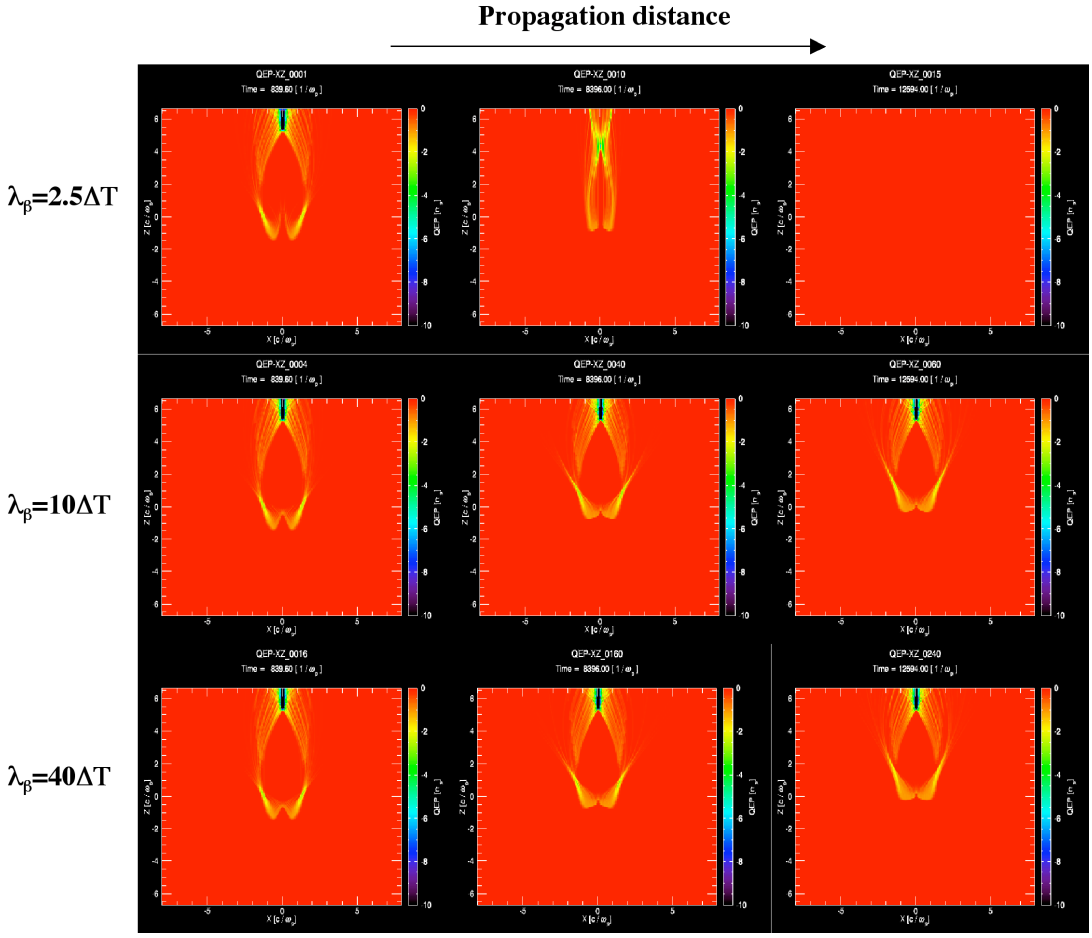

Figure 7.1: Plasma density evolution using different 3D update frequency in QuickPIC (λ_β is the betatron wavelength and ΔT is the 3D time step).

7.3 Erosion rate – the theoretical model

In this section, we will establish the physical picture of beam head erosion in field-ionized plasmas, derive a formula for the erosion rate which depends on the beam/plasma parameters and compare it with simulation results.

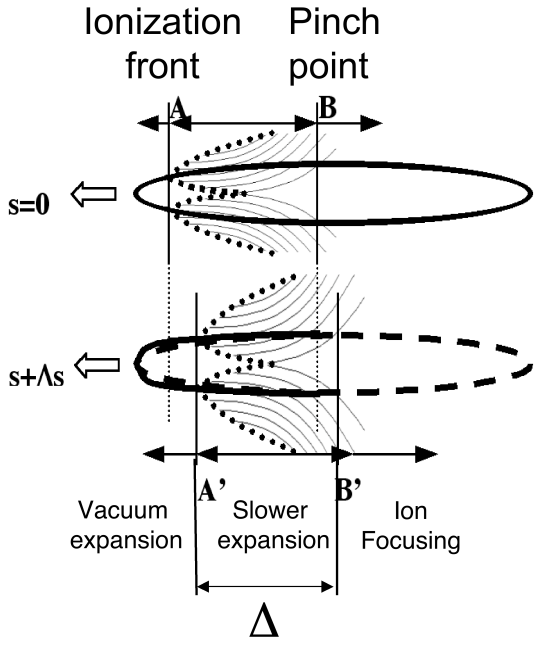

Figure 7.2: Schematic of the ionization front recession.

Fig. 7.2 shows the schematic of the beam head evolution. At s = 0, the ionization front is at A and the ion channel is completely formed at the "pinch point" B. (For a bi-gaussian beam, the ionization front has a "W" shape due to the field structure around it (4.4)). If the beam has a finite emittance, the part before A will undergo vacuum expansion, while that between A and B will expand at a lower rate due to the partially formed ion channel. This spot-size increase between A and B will lead to the position of the ionization slipping backward to a location A' at a later time $s + \Delta s$. We call the distance between A and B the

"blowout time" Δ. Next, we calculate the head erosion rate, which is defined as the rate of the moving ionization front A, $[\xi(A) - \xi(A')]/\Delta s$.

First, we determine the condition for a certain beam slice to become the ionization front. At the ionization front, the maximum beam space charge field equals the ionization threshold (i.e. $E_{rmax} = E_{th}$). By writing out E_{rmax} using the beam parameters, we obtain a beam spot size. This spot size is the maximum possible value for a certain beam slice ξ to ionize the neutral gas, which we call the "ionization spot size" σ_{ri}. It can be written out as follows for flat-top beam and bi-gaussian beams respectively,

$$\sigma_{ri-flat} = 26010 \times \frac{\frac{N}{2\times 10^{10}}}{L_z(\mu m) \cdot E_{th}(GV/m)}(\mu m) \tag{7.1}$$

$$\sigma_{ri-gaussian}(\xi) = 10360 \times \frac{\frac{N}{2\times 10^{10}}}{\sigma_z(\mu m) \cdot E_{th}(GV/m)} \times e^{-\frac{\xi^2}{2\sigma_z^2}}(\mu m) \tag{7.2}$$

In order to calculate the erosion rate, we make the following two assumptions: (1) The "pinch point" spot size σ_{rp} is always equal to the initial beam spot size σ_{r0}. (This is later verified in series of simulations). (2) The spot size increase between the ionization front A and "pinch point" B satisfies a vacuum expansion slowed down by a factor of α $(0 < \alpha < 1)$.

Therefore, σ_{ri} can now be written as

$$\sigma_{ri} = \sigma_{rp}\sqrt{1 + (\frac{\alpha \cdot \frac{\Delta}{V_{etch}}}{\beta^*})^2} \approx \sigma_{r0}\sqrt{1 + (\frac{\alpha \cdot \frac{\Delta}{V_{etch}}}{\beta^*})^2}, \tag{7.3}$$

where V_{etch} is the erosion rate and $\alpha \cdot \frac{\Delta}{V_{etch}}$ is the effective distance for a "pinch point" slice to expand till it becomes the ionization front. From this, the erosion rate can be written out as

$$V_{etch} = \frac{\alpha \cdot \Delta}{\beta^*\sqrt{(\sigma_{ri}/\sigma_{r0})^2 - 1}} = \frac{\alpha \cdot \Delta \cdot \varepsilon_n}{\gamma\sigma_{r0}^2\sqrt{(\sigma_{ri}/\sigma_{r0})^2 - 1}}. \tag{7.4}$$

7.3.1 Erosion of flat-top beams

For a flat-top beam, both Δ and σ_{ri} remain relatively constant as the beam head erodes (i.e. not a function of ξ). Therefore, the erosion rate, V_{etch}, should also be a constant. A series of simulations were carried out to test the scaling with different parameters based on (7.4). The "base" simulation parameters chosen are: $N = 1.8 \times 10^{10}$, $\sigma_{r0} = 10\mu m$, $L_z = 50\mu m$, $\gamma = 82192(42\text{GeV})$, $\varepsilon_n = 410.96mm \cdot mrad$ and $n_{lithium} = 2.7 \times 10^{17} cm^{-3}$. The beam charge N, energy γ, normalized emittance ε_n and lithium density $n_{lithium}$ are varied from 1/4 to 4 times the "base" value respectively, and the initial spot size, σ_{r0}, is varied from 1/2 to 2 times its "base" value.

Fig.7.3 shows the ionization front location as a function of the propagation distance for different emittances and different energies. Fig.7.4 shows that the erosion rate derived from Fig.7.3 has the correct scaling with the emittance and energy (i.e. $V_{etch} \propto \varepsilon_n$ and $V_{etch} \propto \frac{1}{\gamma}$) as predicted by (7.4). In fact, the coefficient in front of the scaling was verified too. For example, in the series where emittance is varied, if we use $\alpha \approx 1/2$ and $\Delta = 30\mu m$(as was observed in simulations), (7.4) gives $V_{etch}(\mu m$ per cm)$\approx 0.00275\varepsilon_n(mm \cdot mrad)$. This agrees with the simulation results, where Fig.7.4(a)'s linear fit gives $V_{etch}(\mu m$ per cm)$\approx 0.00265\varepsilon_n(mm \cdot mrad)$). Simulations (Fig.7.5) also verified the decrease of V_{etch} with an increasing N, as well as V_{etch}'s weak dependence on both σ_{r0} (when $\sigma_{ri} >> \sigma_{r0}$) and $n_{lithium}$.

Last, it is worth noting that for a flat-top beam, the blow-out time can be estimated using $\Delta \sim 4\frac{c}{\omega_{pbpeak}}$ according to these simulations.

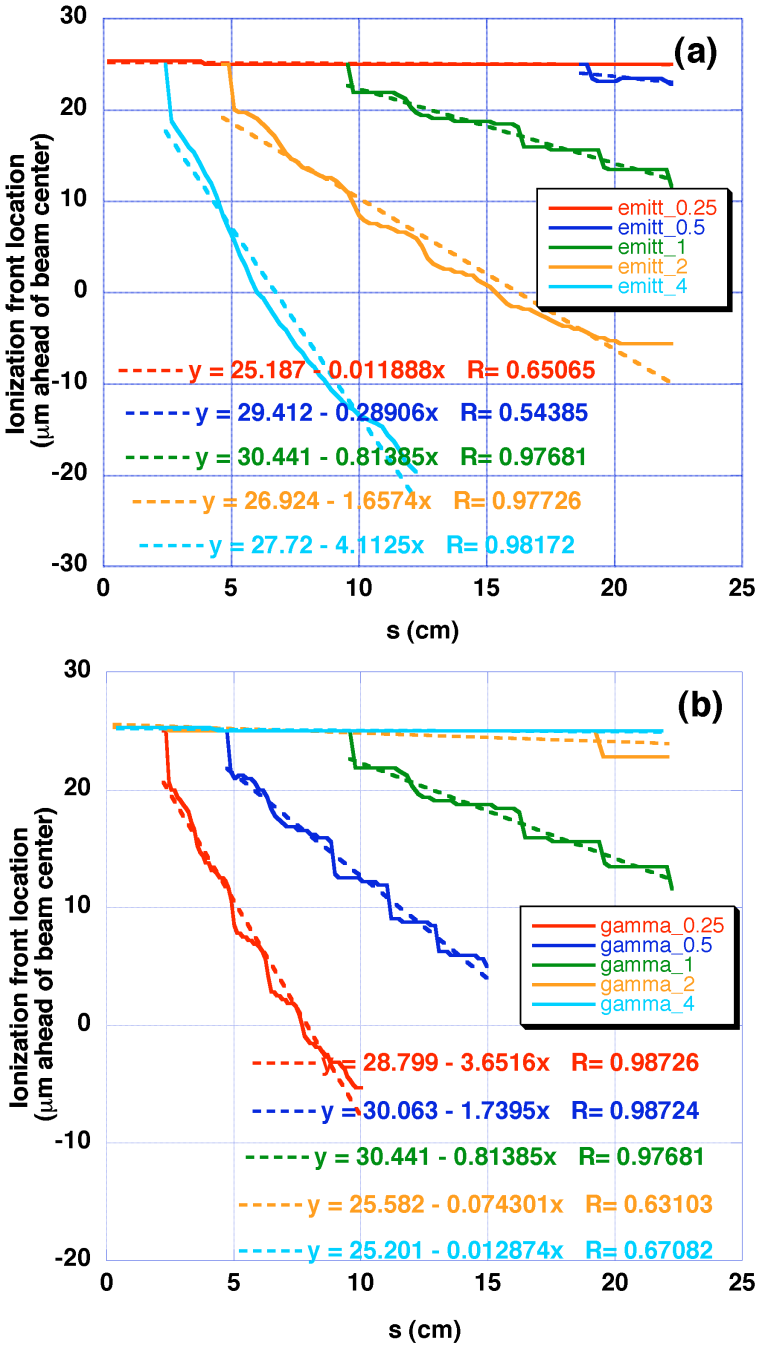

Figure 7.3: Time evolution of the location of the ionization front for (a) different emittances and (b) different beam energies, for flat-top beams

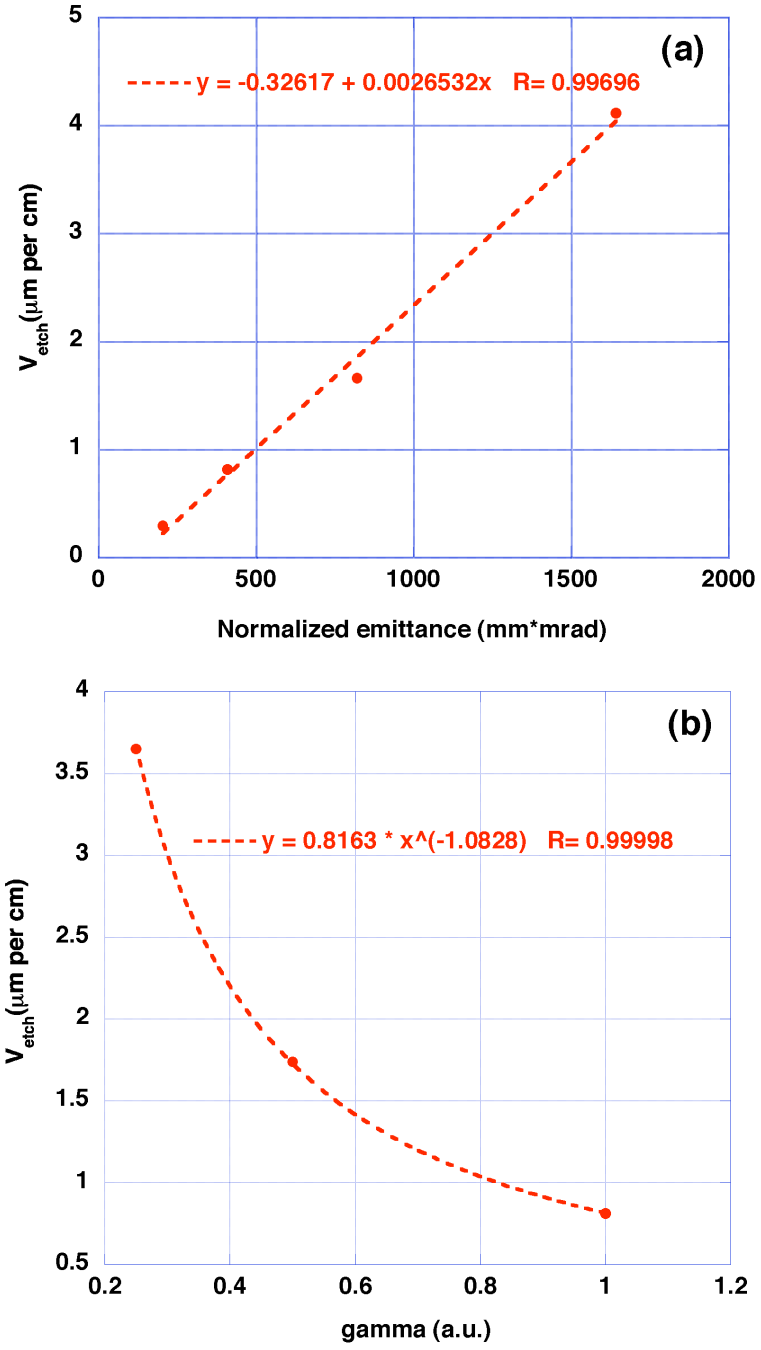

Figure 7.4: Erosion rate scaling with (a) beam emittance (b) beam energy. Dots: data obtained from Fig.7.3 (Points with minimal erosion excluded).Dashed lines (a) linear fit (b) power fit of the data.

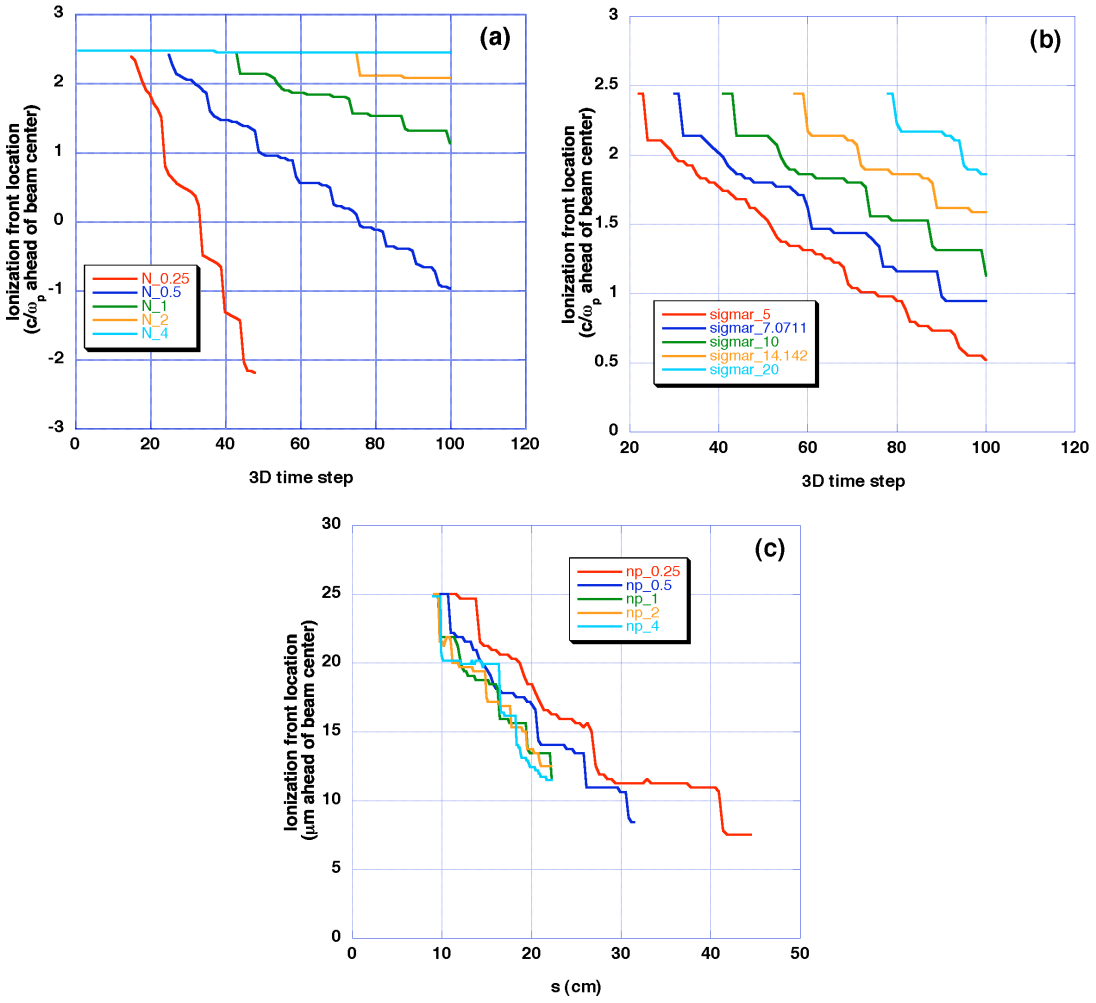

Figure 7.5: Time evolution of the location of the ionization front for different (a) beam charge, (b) initial spot sizes, and (c) lithium densities for flat-top beams.

7.3.2 Erosion of gaussian beams

For bi-gaussian beams, both Δ and σ_{ri} change along the beam (i.e. are functions of ξ). In order to make an estimate of the average V_{etch} (from the beam head to the beam center), we use the Δ and σ_{ri} values at one σ_z ahead of the beam center. (i.e. $\sigma_{ri} \sim \sigma_{ri}(\xi = -\sigma_z) = 0.607\sigma_{ri}(\xi = 0)$, $\Delta \sim 4\frac{c}{\omega_{pb}(\xi=-\sigma_z)} = 5.1\frac{c}{\omega_{pbpeak}}$). For example, for a beam similar to the one used in Chapter 6 (except symmetric with the larger emittance), i.e. $N = 1.7 \times 10^{10}$, $\sigma_{r0} = 10\mu m$, $\sigma_z \approx 15\mu m$, $\beta^* = 8.2cm$, the above estimate gives $V_{etch} \sim 0.4\mu m$ per cm (assuming $\alpha = 1/2$ and $E_{th} = 7GV/m$). This value is in surprisingly good agreement with the simulation observation of the ionization front recession of $\sim 26\mu m$ in 70 cm (s=10 to s=80 cm).

For a certain propagation distance s, in order for the head erosion not to become detrimental, the eroded part should be less than a fraction of the beam length (e.g. $1\sigma_z$). Therefore, $V_{etch} \cdot s < \sigma_z$ needs to be satisfied. Using (7.4), this can be written as

$$\alpha \cdot \frac{\Delta}{\sigma_z} \cdot \frac{\sigma_{r0}}{\sigma_{ri}} \cdot \frac{s}{\beta^*} < 1, \tag{7.5}$$

where $\sigma_{ri} >> \sigma_{r0}$ was assumed. If we further assume $\alpha = 1/2$ and use the $\xi = -\sigma_z$ as location for determining Δ and σ_{ri}, this condition becomes

$$\frac{1}{2466}\frac{c}{\omega_{pbpeak}}(\mu m)\frac{\sigma_{r0}(\mu m)E_{th}(GV/m)}{\frac{N}{2\times 10^{10}}}\frac{s}{\beta^*} < 1. \tag{7.6}$$

This is a useful tool in estimating the influence of head erosion for certain beam/plasma parameters. For example, for the E167 SLAC experiment parameters, i.e. $N = 1.7 \times 10^{10}$, $\sigma_{r0} = 10\mu m$, $\sigma_z = 15\mu m$ in lithium ($E_{th} \approx 7GV/m$), this gives $s < 4.8\beta^* \sim 50cm$ (use the larger emittance in x direction $\varepsilon_n \sim 100mm \cdot mrad$). In this case, the pump depletion length is $\sim 1m$ (42.5GeV, $E_{dec} \sim 50GV/m$). Therefore, for this 42.5GeV stage, beam head erosion is im-

portant since the characteristic erosion distance is similar to the pump depletion length. On the other hand, for a 250GeV stage for future collider parameters, i.e. $N = 4 \times 10^{10}$, $\sigma_{r0} = 3\mu m$, $\sigma_z = 15\mu m$, $\varepsilon_n \sim 1mm \cdot mrad$ in lithium ($E_{th} \approx 7GV/m$), this gives $s < 190\beta^* \sim 800m$. This characteristic erosion distance is much larger than the dump depletion distance of $\sim 5m(E_{dec} \sim 50GV/m)$. Therefore, at this stage, the effects from head erosion may not be a major concern.

CHAPTER 8

Accelerating Ultra-Short Positron Bunches

For the collider application of PWFA, it is also desirable to accelerate positrons in the plasma. In principle, a positron beam may be accelerated in the wakes driven by a positron beam, an electron beam, or a laser beam. Due to the inavailability of intense positron beams (such beams can only be studied at SLAC), their interaction with plasmas has received very little attention compared to that for electron beams. Some work have been done to study the wakes and beam dynamics using a positron driver through simulations[85][86] and experiments[87][48][43][49]. A recent paper also explored the possibility of accelerating positrons in the electron wake[88].

In this chapter, we will first review the properties of the non-linear wakefield produced by a bi-gaussian positron beam, and show the effect of enhancing the transformer ratio by using a hollow channel plasma. Then two simulations (one pre-ionized and one field-ionized) will be used to show the properties of positron beam evolution for an extended propagation length, where a stabilization of the beam envelope is observed. This long propagation of a positron beam in a field-ionized plasma is the first such PIC simulation. At the end, the wakes for the upcoming FACET positron beam parameters will be discussed.

8.1 Wakes of a bi-gaussian positron beam

In the linear regime where the beam density is much smaller than the plasma density, there is no difference in principle between the wakes produced by electron or positron beams. There is just a change in sign (a phase shift). However, for high drive beam densities, the plasma response is nonlinear, and there is no symmetry between an electron driver and a positron driver. The reason is that the wake is also excited due to the motion of the plasma electrons. For electron beams, the plasma electrons are evacuated from the beam location and an ion channel with uniform density is formed (the "blow-out" regime). While for positron beams, the plasma electrons are attracted to the beam location, and overshoot (the "suck-in" regime). For such cases, the plasma density can have complicated structures as shown in Fig. 8.1.

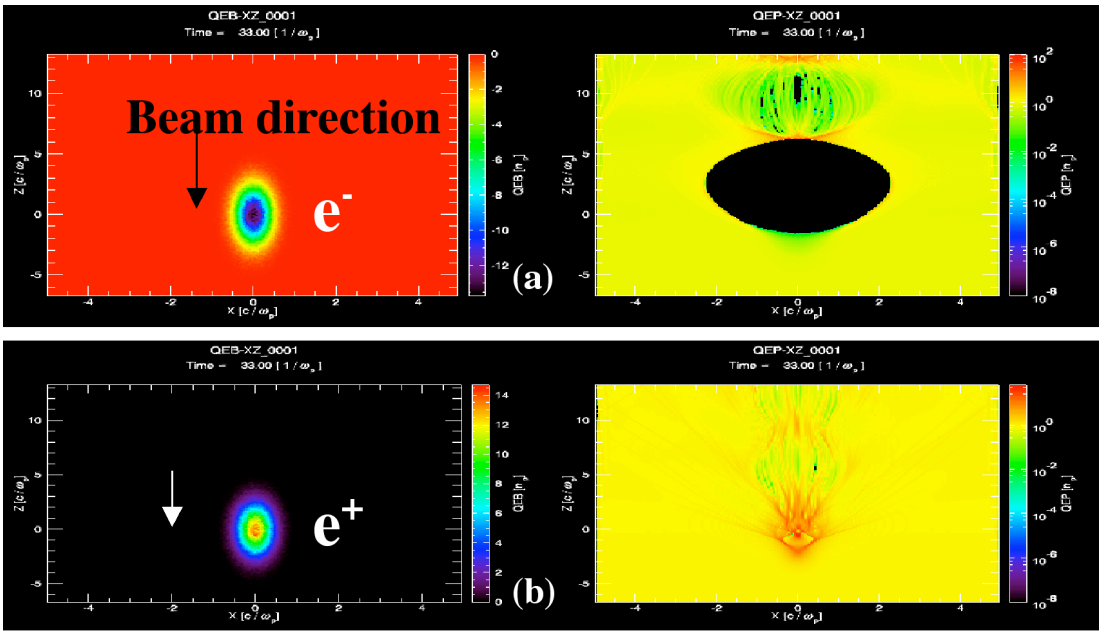

Figure 8.1: Beam density (left) and plasma density (right) for the (a) "blow-out" regime of an electron driver and (b) "suck-in" regime of a positron driver.

It has been found that for similar electron and positron drivers, the nonlinear positron wakes are in general smaller and less ideal than nonlinear electron wakes. This is due to the phase mixing effect[85] in the "suck-in" regime, where plasma electrons from different radii flow in and reach the axis at different locations, resulting in a smaller density concentration as compared to the high density peak at the end of the electron wake bucket. Sometimes, this phase mixing effect also results in an accelerating peak that is off the axis[85].

Besides the smaller amplitude of the wake, the transverse focusing fields are also very different for a positron beam. As shown in Fig. 8.2 (left), in the electron wake, the focusing field ($E_r - B_\theta$) is uniform along z (the beam propagation direction) and linear with r (transverse direction), while in the positron wake(right), it is neither uniform along z, nor linear with r.

It has been suggested that using a plasma in the shape of a hollow cylinder may reduce the phase mixing effect and therefore increase the accelerating wake for a positron driver[85]. QuickPIC simulations were performed to reexamine this idea, and it was found that a more pronounced effect from the hollow channel plasma was the greatly enhanced transformer ratio. Fig. 8.3 compares the wake from a uniform plasma and that from a plasma with a hollow channel of radius c/ω_p. The parameters used here are the same as in [85], i.e. $N_b = 2.0 \times 10^{10}$,$\sigma_r = 75\mu m$, $\sigma_z = 45\mu m$, and $n_p = 4.3 \times 10^{14} cm^{-3}$. It is obvious that the hollow channel reduces the phase mixing effect and plasma electrons do concentrate to a smaller spot size on axis. The channel radius is varied to search for the optimal wake, and Fig. 8.4 plots the maximum accelerating peak and the transformer ratio versus the channel radius. Although the accelerating peak does increase as expected at some radius (e.g. $r = 0.5c/\omega_p$ in Fig. 8.4(a)), the factor is small. The increase of transformer ratio at some radius is much more obvious, e.g. when the channel

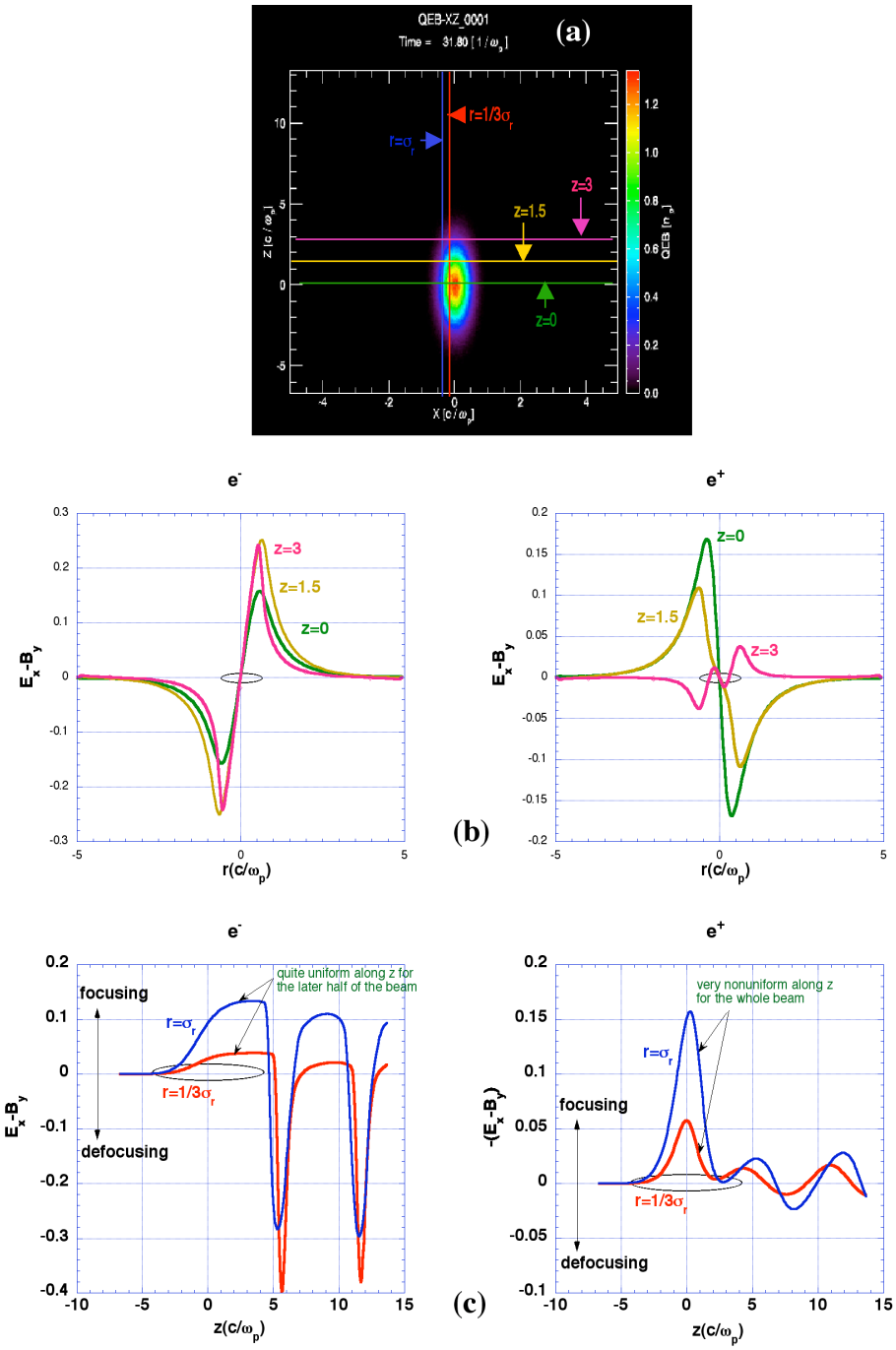

Figure 8.2: (a) Electron or positron beam density (beam propagating down); (b) Focusing field lineout at different z locations as shown in (a); (c) Focusing field lineout at different r locations as shown in (a). On the left are plots from an electron wake while on the right are plots from a positron wake.

radius is c/ω_p, the transformer ratio increased to 1.75 as compared to 1.2 in a uniform plasma. From Fig. 8.3 we can see, this can be mainly attributed to the reduction of the decelerating peak.

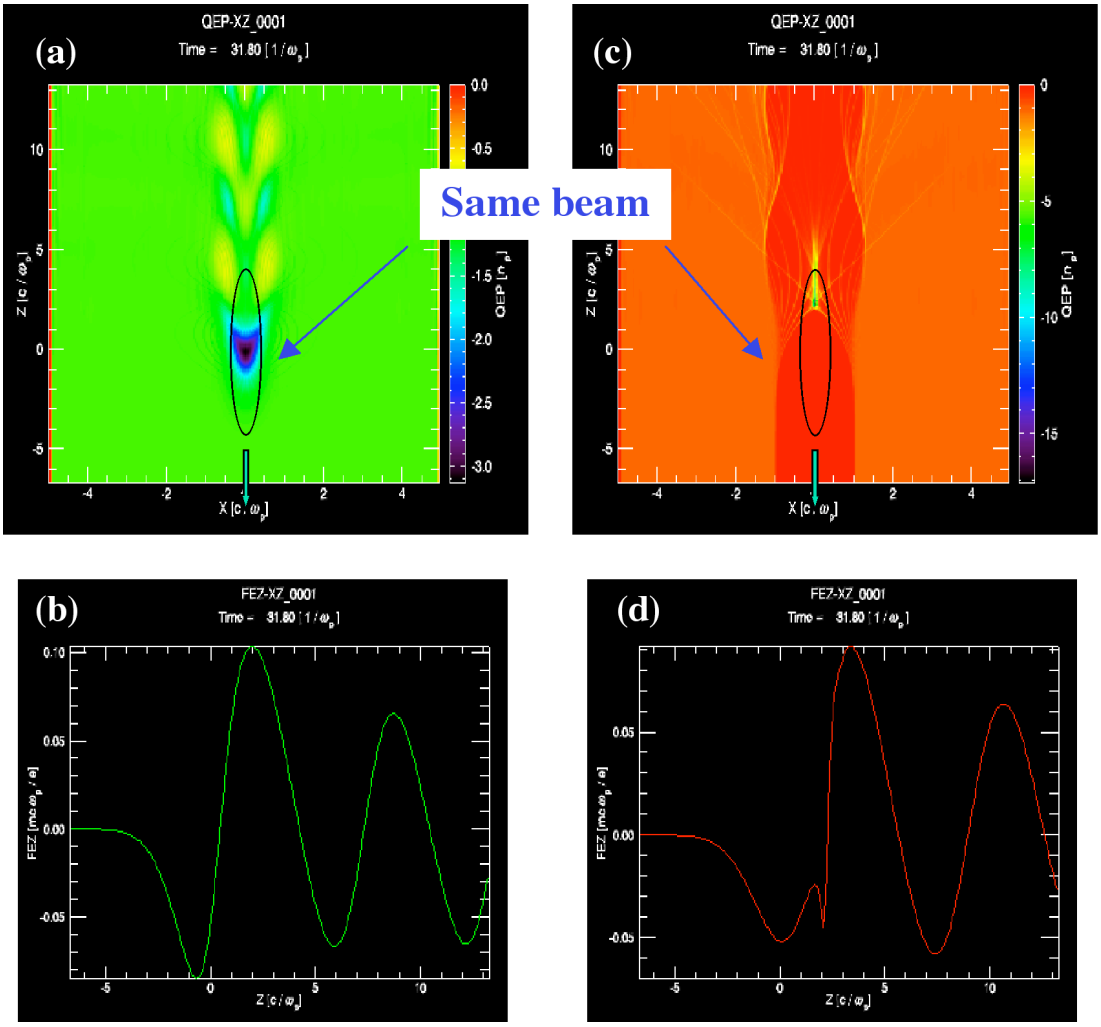

Figure 8.3: Plasma density and longitudinal wakefield lineout on axis of a uniform plasma (a and b) and a hollow channel plasma, with a radius c/ω_p (c and d).

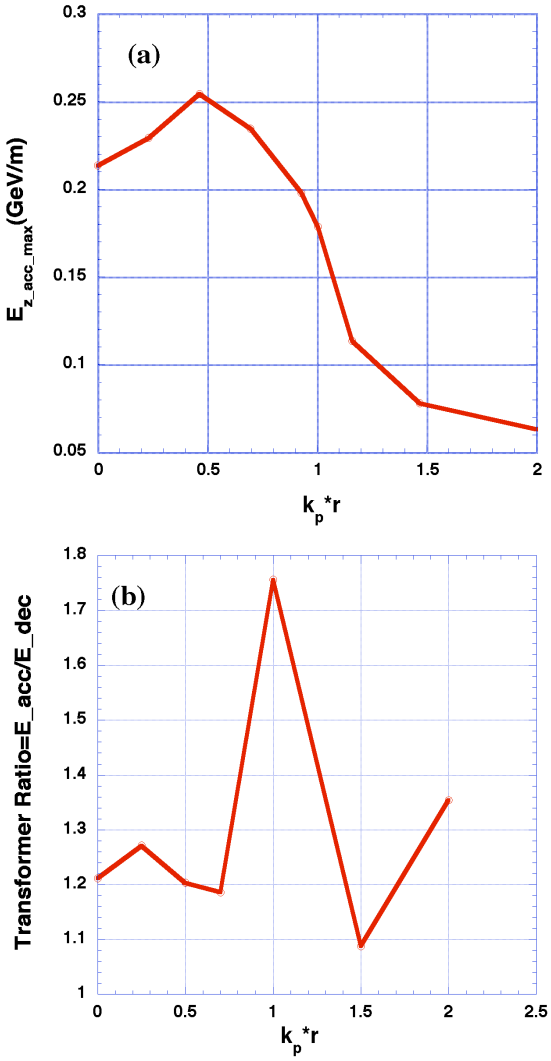

Figure 8.4: (a) Magnitude of maximum accelerating peak, and (b) Transformer ratio, of the positron wake as a function of the hollow channel radius.

8.2 Positron beam evolution in an extended plasma length

The previous section discussed the wakes from a bi-gaussian beam but has not considered how the beam evolves under its own wakefield. Experiments have been carried out to measure the beam acceleration[43], as well as the beam focusing, e.g. [87] in a short plasma ($\sim 3mm$) and [48],[49] in an extended-length($1.4m$). However, how the beam and wake evolves inside the plasma is not fully understood. In this section, two simulations will be shown where the stabilization of the positron beam envelope during propagation is observed. Although a field-ionized positron wake has been simulated using a PIC code before[86], it is the first simulation that evolved the beam in an extended length in a field-ionized plasma.

Fig. 8.5 shows the beam density evolution in a pre-ionized plasma. The parameters used here are a $28.5GeV$ beam with $N_b = 2\times10^{10}$, $\sigma_r = 11\mu m$, $\sigma_z = 58.7\mu m$, $\varepsilon_{nx} = 50mm \cdot mrad$, $\varepsilon_{ny} = 5mm \cdot mrad$ and the plasma density is $2 \times 10^{16}cm^{-3}$. It is obvious that the beam focuses to a much smaller spot size and modulates drastically during the first $15cm$ of propagation. After this, the beam envelope in the configuration space stabilizes, and keeps almost unchanged up to at least 100 centimeters. The initial longitudinal wakefield when the beam is still bi-gaussian and the stablized longitudinal wakefield when the beam has reached the "stable envelope" are plotted in Fig. 8.6. The stable wakefield is similar but slightly larger than the initial wake. The corresponding plasma densities are plotted in Fig. 8.7. We believe the physical mechanism that leads to the nonlinear equilibrium is related to nonlinear matching in accelerators and the nonlinear BGK modes in plasmas. The basic idea is that for any nonlinear focusing force, there is some transverse profile of the beam for which the beam is in equilibrium. In this case, the focusing force is a function of the beam's radial profile. Therefore,

the force also changes as the beam evolves. It seems that over the time this self-consistent equilibrium is reached. This is analogous to the formation of BGK waves in plasma waves where the plasma must find the equilibrium distribution function (a balance of trapped and untrapped particles for a given potential).

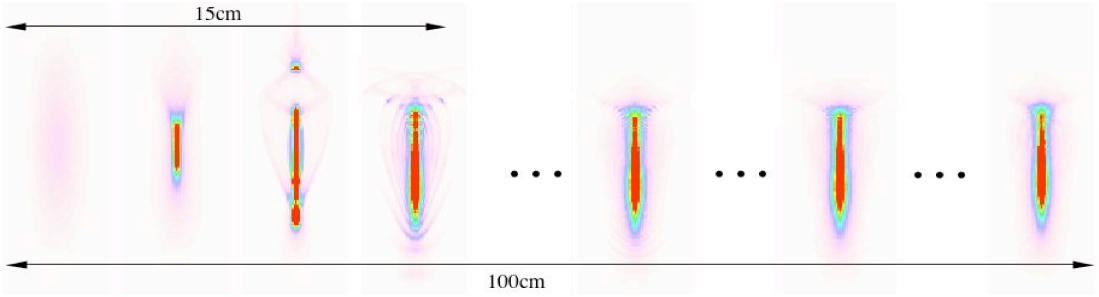

Figure 8.5: Positron beam density evolution in a pre-ionized plasma.

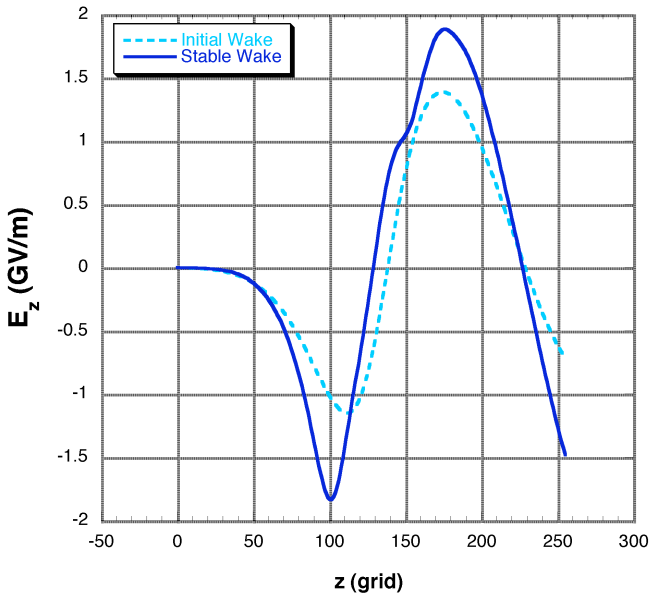

Figure 8.6: Initial and stable longitudinal wakefield of a positron beam in a pre-ionized plasma (beam propagating to the left).

Fig. 8.8 shows the beam density evolution in a field-ionized plasma. The

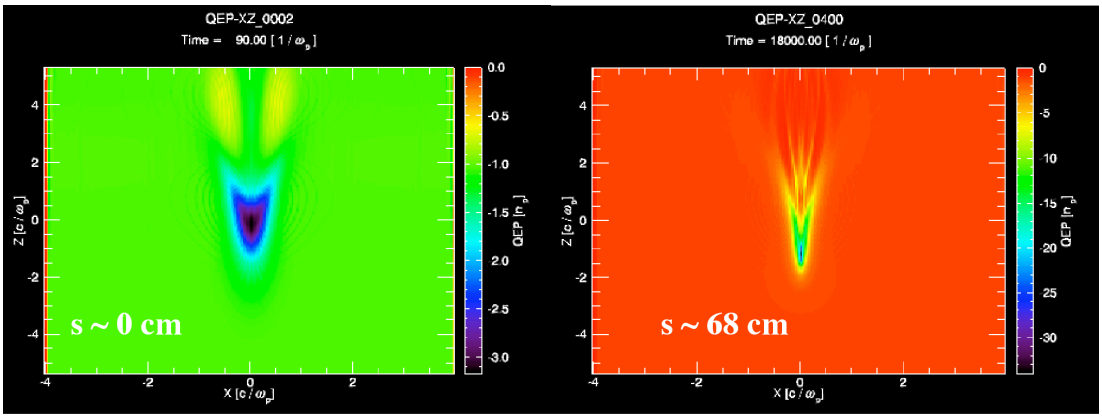

Figure 8.7: Initial ($s \sim 0cm$) and stable ($s \sim 68cm$) plasma densities in the wake of a positron beam in a pre-ionized plasma.

parameters used here are $28.5GeV$ beam with $N_b = 8.8 \times 10^9$, $\sigma_r = 11\mu m$, $\sigma_z = 19.6\mu m$, $\varepsilon_{nx} = 50mm \cdot mrad$, $\varepsilon_{ny} = 5mm \cdot mrad$ and the plasma density is $1.8 \times 10^{17} cm^{-3}$. These parameters are similar to the SLAC experiments except with about half the beam charge. Similar to the pre-ionized case, the beam also focuses and modulates drastically during the earlier part of its propagation ($\sim 6.7cm$), and it eventually reaches a "stable envelope". The only difference here is the head erosion occurs and shortens the beam. Similarly to that for an electron beam, the head erosion of a positron beam in field-ionized plasma is also due to the lack of focusing at the beam head and the resulting slippage of the ionization front, except that the focusing is from the plasma electrons that flow in to the axis. The initial and eventual stable longitudinal wake and the corresponding plasma densities are also plotted in Fig. 8.9 and Fig. 8.10 respectively. Interestingly, the erosion of the beam head before the ionization front leads to a flatter radial profile. This provides a force on the plasma electrons that is linear in r, causing the plasma electrons that originate within the beam to arrive on axis at the same time. The resulting tight density spot is seen in Fig. 8.10 $s \sim 14cm$. This high

density spot causes a spike in the decelerating field as shown in Fig. 8.9.

In order to understand the transverse behavior of the beam, we examine the focusing field near the beam. Fig. 8.11(a) shows that at the initial location when the beam is still gaussian, the focusing field is not linear across the beam as expected. While after the beam obtains the "stable envelope" as shown in Fig. 8.11(b), the focusing field is pretty linear which made conservation of the envelope shape possible. (Note: although the beam has focused to a very tight spot size, the transverse resolution was enough to resolve the linear focusing as shown in Fig. 8.11(b)(iv)).

In this simulation where the synchrotron radiation reaction force was turned on, $5.7GeV$ energy gain was observed for the rear part of the beam in $39cm$ of propagation distance as shown in Fig. 8.12. By comparing this simulation with an identical one without the radiation reaction force (not shown), we can conclude that the radiation effects here are negligibly small. This is likely to be true for most positron wakefield cases due to the tight spot sizes the beams develop under the strong focusing.

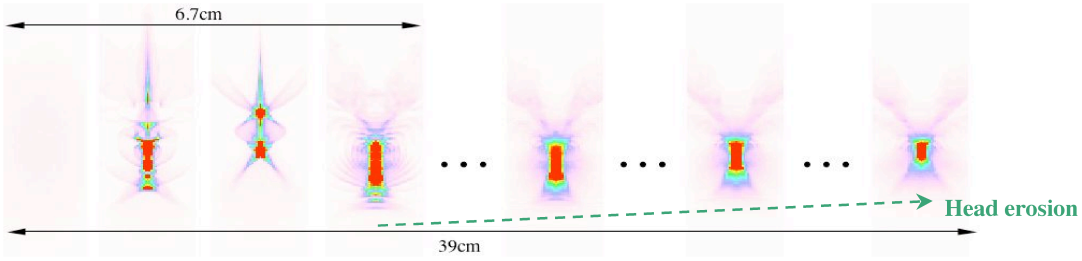

Figure 8.8: Positron beam density evolution in a field-ionized plasma.

Since the characteristic betatron frequency of the initial phase of the beam evolution is not known initially, we did a convergence test on the time step for resolving the evolution of the beam. This is shown in Fig. 8.13. The results

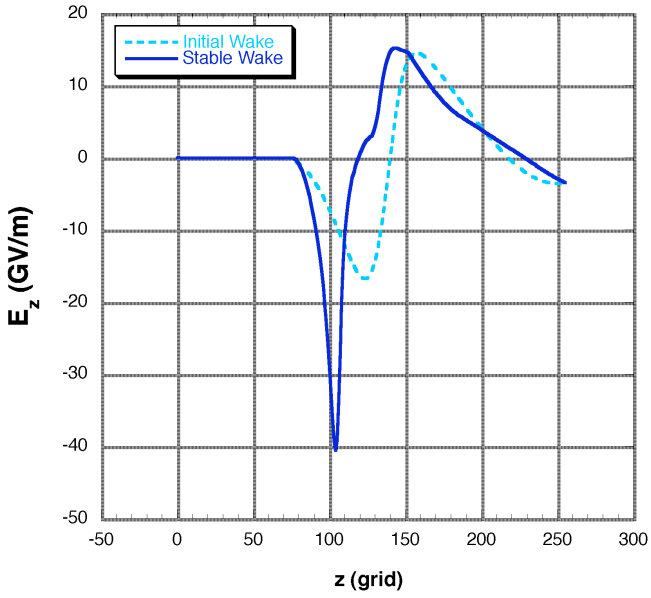

Figure 8.9: Initial and stable longitudinal wakefield of a positron beam in a self-ionized plasma (beam propagating to the left).

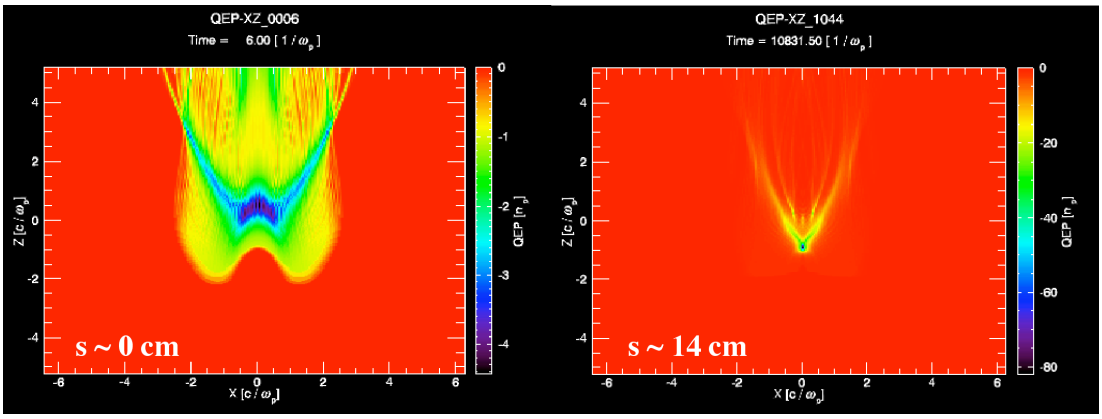

Figure 8.10: Initial ($s \sim 0cm$) and stable ($s \sim 14cm$) plasma densities in the wake of a positron beam in a self-ionized plasma.

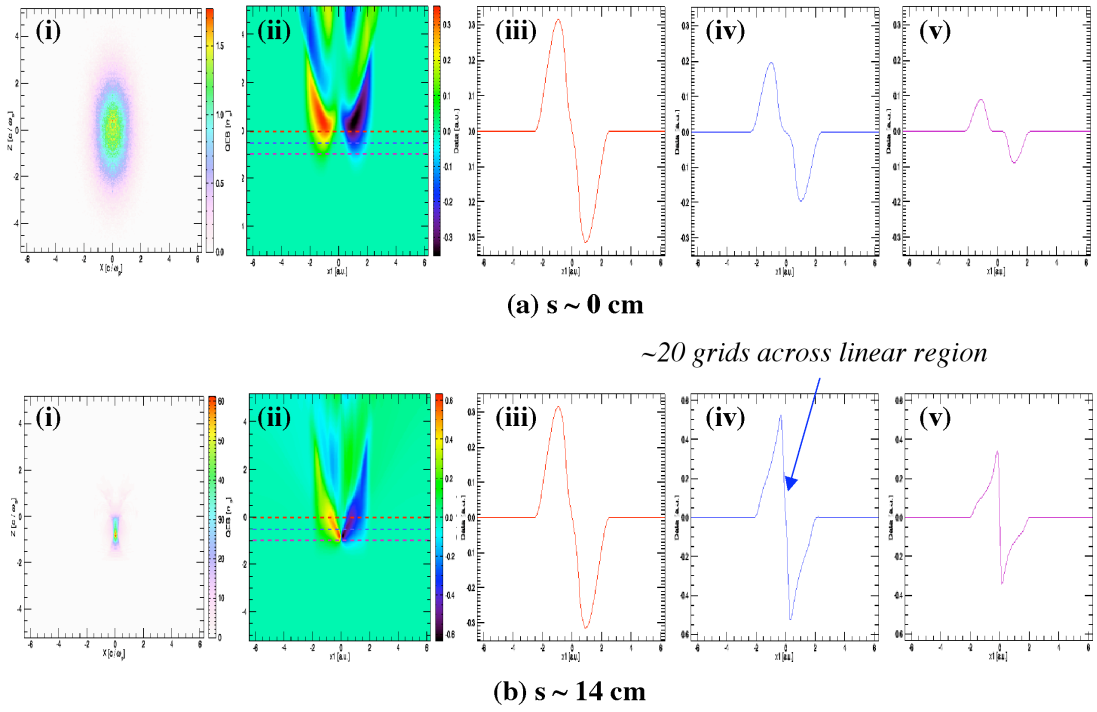

Figure 8.11: (a) Initial ($s \sim 0cm$) and (b) stable ($s \sim 14cm$) focusing fields in a field-ionized plasma wake (i) beam density (ii) focusing field $E_r - B_\theta$ (iii)-(v) lineout of the foucsing field as shown in (ii).

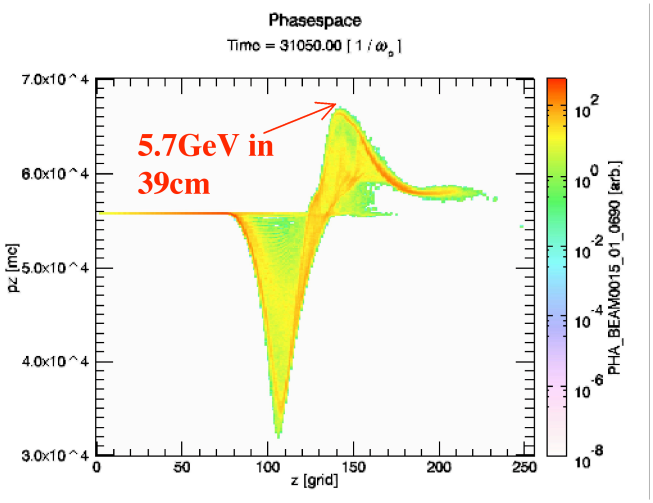

Figure 8.12: Phase space p_z vs. z density of a positron beam after propagation of $39cm$ in a self-ionized plasma.

suggest that resolving the betatron frequency of a corresponding electron beam in the ion channel (i.e. $20 \sim 30$ updates per betatron wavelength) is sufficient. The behavior of the initial modulation are similar to those with time steps small enough to resolve the plasma frequency. A convergence test on the transverse resolution was also performed as shown in Fig. 8.14. The results suggest that although the beam focuses to a tight spot size, the transverse resolution was sufficient to retain the major characteristics of the beam envelope.

8.3 Positron wakes for FACET relevant parameters

In order to obtain the optimal wake, a plasma density scan was done for the future FACET electron and positron beam parameters as shown in Fig. 8.15. As the first step, only the wake of the initial gaussian beam was examined and the beam parameters are $N_b = 2 \times 10^{10}$, $\sigma_r = 5.3\mu m$ and $\sigma_z = 26\mu m$. For electron beams, it is straightforward to pick the optimal density based on the largest

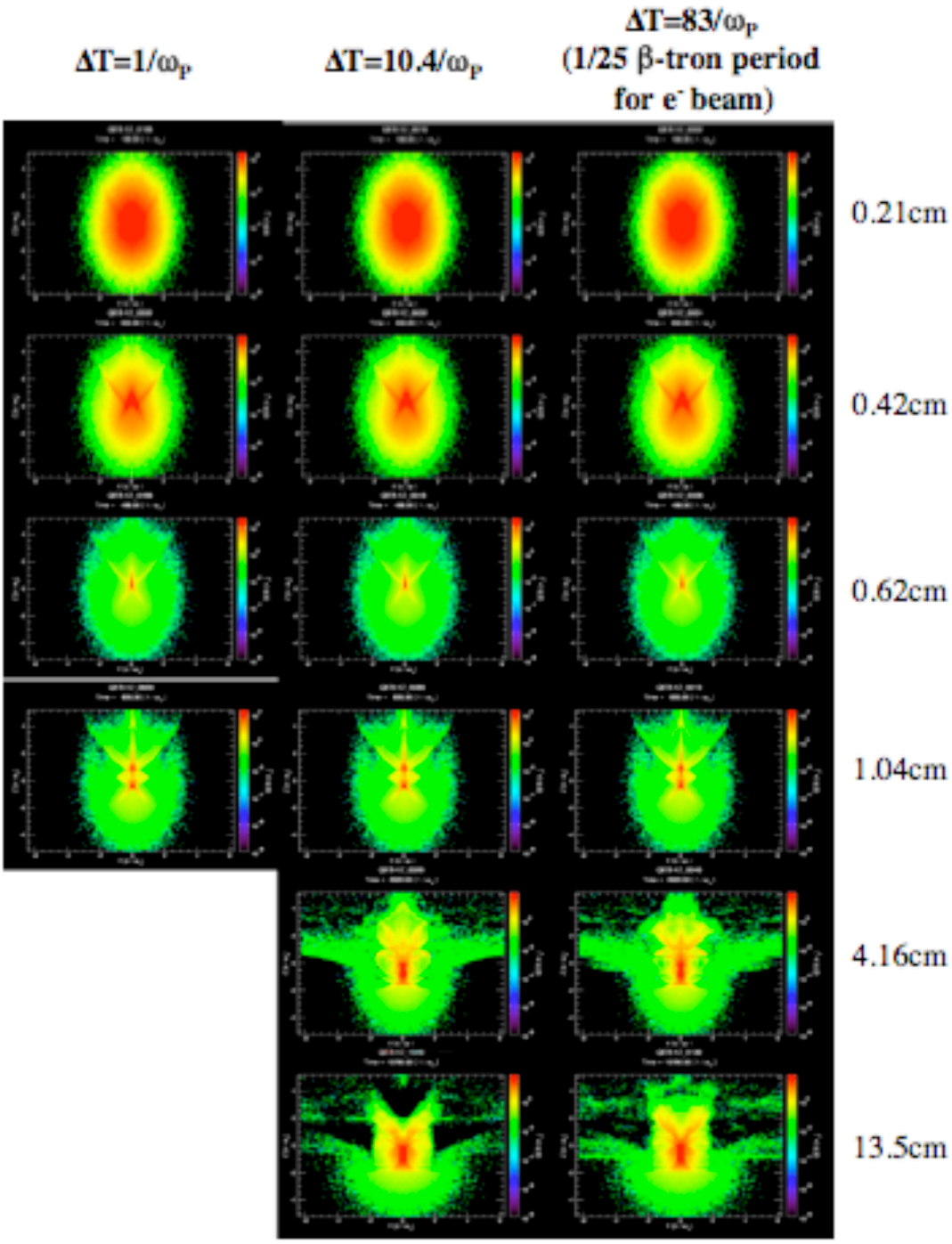

Figure 8.13: Convergence test of different beam updating frequencies.

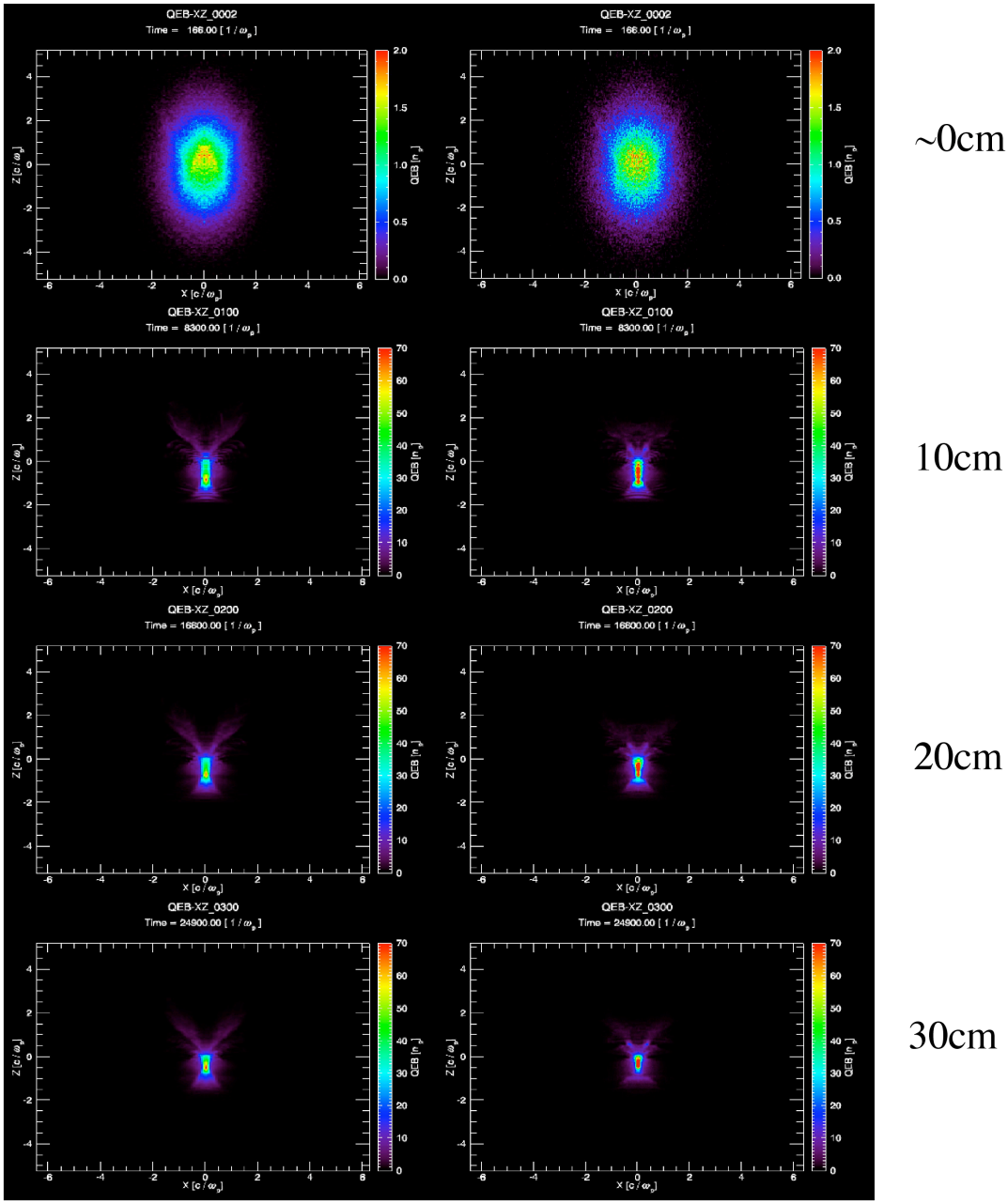

Figure 8.14: Convergence test of different transverse resolution.

wake and optimal peak location since the wake barely changes afterward. For a positron wake, longer simulations will be needed since the stable wake may differ from the initial wake.

Another complication of the positron wake is the high frequency part of the wake near the beam as shown in Fig. 8.15(b). This high frequency component is due to the local plasma frequency which is dominated by the beam when $n_b > n_p$. In this case, $n_{bpeak} = 1.7 \times 10^{18} cm^{-3}$ and this corresponds to a wavelength of $2\pi c/\omega_{pbpeak} = 24\mu m$, which agrees with the wavelength at the beam peak. The higher the plasma density (as long as $n_p < n_b$), the more this high frequency manifests itself because more plasma electrons are oscillating around the positron beam. Behind the beam, the real plasma frequency dominates.

Based on observations discussed in the previous section, the amplitude of the stable accelerating field is likely to be similar to that of the initial wake. Although further simulations need to be done, it is likely that the FACET positron beams will be able to achieve accelerating field on the order of $10GV/m$.

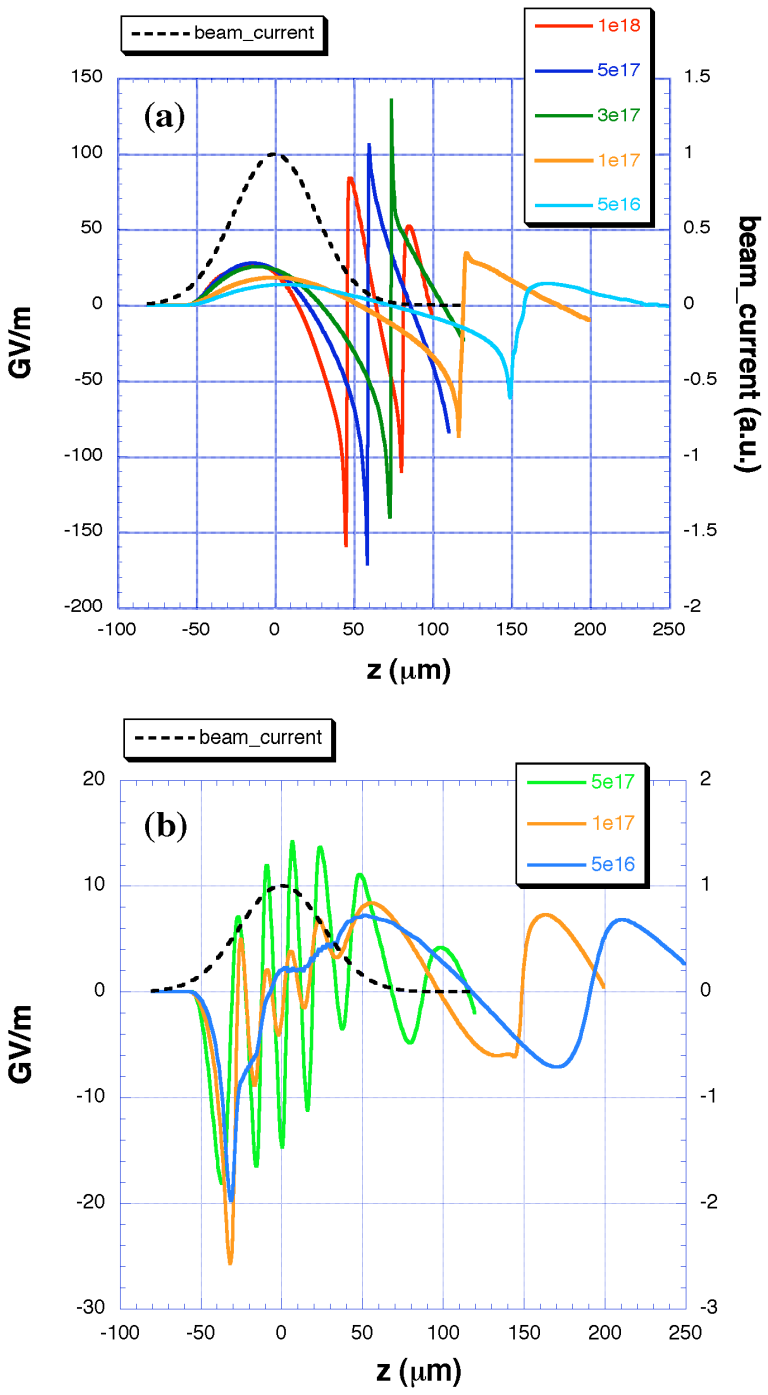

Figure 8.15: Longitudinal wakefields under different densities using FACET beam parameters for (a) electron driver and (b) positron driver.

CHAPTER 9

Summary

This dissertation has studied the acceleration of ultra-short electron/positron bunches in field-ionization produced plasmas using the parallel quasi-static PIC code QuickPIC. In order to model the afterburner relevant PWFA experiments at SLAC, where new physics emerged recently, several models were added into the code. These models include a field-ionization package based on the ADK model, where wake benchmark shows very good to excellent agreement with the results from full PIC code OSIRIS; a radiation reaction model, where an equivalent field is proved to be accurate enough to model the drag force; as well as the ability to initialize more realistic beam/plasma parameters. The implementation of a preliminary model that handles the trapped particles by "promoting" plasma particles into beam particles was also described. Improvement in the "promoting" criteria will be needed to get more accurate wakes.

Field-ionized wakes excited by an electron beam in the blow-out regime were studied by comparing them with the pre-ionized wakes. It was found that in order to achieve similar wakes as in pre-ionized plasmas, the ionization region needs to exceed the blow-out radius which is a plasma density dependent quantity. Based on this, the optimal plasma/neutral densities for wake excitation was discussed.

Detailed modeling of the recent energy doubling experiment at SLAC explained some of the experimental observations (such as beam scalloping) and helped to understand some aspects of the underlying physics (such as particle

deflection, influence of the emittance asymmetry, beam/plasma energy transfer). One major finding from the simulations was that the much faster beam head erosion rate in the field-ionized plasma is what limited further energy gain. There was quantitative agreement between QuickPIC results and the experimental observations for the saturated energies and the plasma lenth for which it saturated.

The head erosion rate in field-ionized plasmas for an electron beam was studied through theory and simulations. A theoretical model for the erosion rate was described and its estimates agreed with simulation observations. Convergence test was performed to make sure essential physics were resolved in the simulations.

The wakes producded by ultra-short positron beams was studied using QuickPIC simulations. In pre-ionized plasmas, an enhancement in transformer ratio was observed using a hollow channel plasma. The first simulation that models the propagation of a positron beam in a field-ionized plasma over many betatron oscillations was presented. Beam head erosion as well as the dynamic focusing followed by a stabilization of the beam envelope was observed. In this simulation, which has beam parameters in the same range as those can be produced at SLAC, part of the beam achieved multi-GeV energy gain in tens of centimeters. Positron wakes in field-ionized plasmas for future FACET parameters was also discussed and multi-GV/m accelerating gradients are likely to be achieved.

APPENDIX A

Conserved Quantity of Particle Motion (reproduced from [61])

In this appendix we will derive the conserved quantity of plasma electron's motion,

$$\frac{d}{dt}\left[\gamma_e - \tilde{p}_z - (1-\tilde{q}_e\tilde{\psi})\right] = 0 \tag{A.1}$$

where $\tilde{p}_z = p_z/mc = \gamma\beta_z$, $\tilde{q}_e = q_e/e$ and $\tilde{\psi} = \psi e/(mc^2)$ are the normalized parallel momentum, normalized charge and normalized "pinch potential" respectively. The dimensionless velocity becomes $\vec{\beta} = \vec{v}/c$.

We start from the momentum equation,

$$\frac{d\tilde{p}_z}{dt} = \frac{\tilde{q}_e e}{mc}\left[-\frac{\partial\phi}{\partial z} - \frac{\partial A_z}{c\partial t} + \beta_x \times (\frac{\partial A_x}{\partial z} - \frac{\partial A_z}{\partial x}) + \beta_y \times (\frac{\partial A_y}{\partial z} - \frac{\partial A_z}{\partial y})\right] \tag{A.2}$$

and energy equation,

$$\frac{d\gamma}{dt} = \frac{q_e}{mc^2}\vec{v}\cdot\vec{E} = \frac{\tilde{q}_e e}{mc}\left[-\vec{\beta}\cdot\nabla\phi - \vec{\beta}\cdot\frac{\partial\vec{A}}{c\partial t}\right] \tag{A.3}$$

Subtracting Eq.(A.2) from Eq.(A.3), we get,

$$\frac{d(\gamma-\tilde{p}_z)}{dt} = \frac{\tilde{q}_e e}{mc}\left[-(\frac{\partial}{c\partial t} + \vec{\beta}\cdot\nabla)(\phi - A_z) + (\frac{\partial}{c\partial t} + \frac{\partial}{\partial z})(\phi - \vec{\beta}\cdot\vec{A})\right] \tag{A.4}$$

The first term on the right hand side can be rewritten as

$$-\frac{\tilde{q}_e e}{mc}(\frac{\partial}{c\partial t} + \vec{\beta}\cdot\nabla)(\phi - A_z) = -\frac{d}{dt}(\tilde{q}_e\tilde{\psi}) \tag{A.5}$$

The second term can be rewritten in terms of the $\xi = ct - z$ and $s = z$ coordinates as

$$\frac{\tilde{q}_e e}{mc}(\frac{\partial}{c\partial t} + \frac{\partial}{\partial z})(\phi - \vec{\beta}\cdot\vec{A}) = \frac{\tilde{q}_e e}{mc}\frac{\partial}{\partial s}(\phi - \vec{\beta}\cdot\vec{A}) \tag{A.6}$$

Therefore,

$$\frac{d(\gamma - \tilde{p}_z + \tilde{q}_e\tilde{\psi})}{dt} = \frac{\tilde{q}_e e}{mc}\frac{\partial}{\partial s}(\phi - \vec{\beta}\cdot\vec{A}) \tag{A.7}$$

and in the spirit of the quasi-static approximation $\partial/\partial s \approx 0$, this becomes,

$$\frac{d(\gamma - \tilde{p}_z + \tilde{q}_e\tilde{\psi})}{dt} = 0 \tag{A.8}$$

If we assume that the plasma is at rest in front of the beam then,

$$\gamma - \tilde{p}_z + \tilde{q}_e\tilde{\psi} = (\gamma - \tilde{p}_z + \tilde{q}_e\tilde{\psi})|_{t=-\infty} = 1. \tag{A.9}$$

From Eq.(A.9) one can obtain a relationship between $\tilde{p}_z$ and $\tilde{p}_\perp$. In particular, squaring both sides of the relationship

$$\gamma = 1 + \tilde{p}_z - \tilde{q}_e\tilde{\psi}. \tag{A.10}$$

leads to

$$\tilde{p}_z = \frac{1 + \tilde{p}_\perp^2 - (1 - \tilde{q}_e\tilde{\psi})^2}{2(1 - \tilde{q}_e\tilde{\psi})}. \tag{A.11}$$

And similarly,

$$\gamma = \frac{1 + \tilde{p}_\perp^2 + (1 - \tilde{q}_e\tilde{\psi})^2}{2(1 - \tilde{q}_e\tilde{\psi})}. \tag{A.12}$$

References

[1] C. Huang et. al., "QUICKPIC: A highly efficient particle-in-cell code for modeling wakefield acceleration in plasmas" J. Compt. Phys., 217, 658-679, 2006

[2] I. Blumenfeld et. al., "Energy Doubling of 42GeV electrons in a meter scale plasma wakefield accelerator", Nature,445, p. 741-744, 2007

[3] T. Tajima and J. M. Dawson, "Laser Electron Accelerator", Phys. Rev. Lett., **4**3, 267, (1979).

[4] J. M. Dawson "Nonlinear electron oscillations in a cold plasma", Phys. Rev., vol. 133, pp. 383-387, 1959

[5] P. Chen, J. M. Dawson, R. W. Huff, and T. Katsouleas, "Acceleration of Electrons by the Interaction of a Bunched Electron Beam with a Plasma", Phys. Rev. Lett., **5**4, 693, 1985.

[6] Y. B. Fainberg, V. A. Balakirev, I. N. Onishchendo, G. L. Shidelnikov and G. V. Sotnikov, "Wakefield excitation in plasma by a train of relativistic electron bunches," Fizika Plazmy, vol. 20,pp. 674-681, 1994

[7] E. Esarey, P. Sprangle, J. Krall, and A. Ting, "Overview of Plasma-Based Accelerator Concepts" IEEE Trans. Plasma Sci., vol. 24,no. 2,pp. 252, 1996

[8] N. A. Krall and A. W. Trivelpiece, "Principles of Plasma Physics", Chapter 4, 1973

[9] Mori, W. B. and Katsoules, T., "Wavebreaking of longitudinal plasma oscillations" Physica Scripta T30, 137, 1990

[10] T. Katsoules, S. Wilks, P. Chen, J. M. Dawson, and J. J. Su, "Beam loading in plasma accelerators" Particle Accelerators, vol. 22,pp. 81-99, 1987

[11] W. Lu, C. Huang, M. Zhou, W. B. Mori and T. Katsouleas, "Limits of linear plasma wakefield theory for electron or positron wake", Phys. Plasmas 12, 063101, 2005

[12] J. B. Rosenzweig, "Nonlinear plasma dynamics in the plasma wakefield accelerator" Phys. Rev. Lett., vol. 58,pp. 555-558, 1987

[13] P. Sprangle, E. Esarey and A. Ting, "Nonlinear theory of intense laser-plasma interactions" Phys. Rev. Lett., vol, 64, pp.2011-2014,1990

[14] E. Esarey and M. Pilloff, "Nonlinear analysis of relativistic harmonic generation by intense lasers in plasmas" IEEE Trans. Plasma Sci., vol, 21, pp. 95-104,1993

[15] J. B. Rosenzweig, B. Breizman, T. Katsouleas, and J. J. Su, "Acceleration and focusing of electrons in two-dimensional nonlinear plasma wakefields" Phys. Rev. A, vol. 44, pp. R6189-R6192, 1991

[16] P. Sprangle, E. Esarey, J. Krall and G. Joyce, "Propagation and guiding of intense laser pulses in plasmas" Phys. Rev. Lett., vol. 69, pp.2200-2203,1992

[17] W. Lu, C. Huang, M. Zhou, M. Tzoufras, F. S. Tsung, W. B. Mori, and T. Katsouleas, "A nonlinear theory for multidimensional relativistic plasma wave wakefields", Phys. Plasmas 13, 056709, 2006

[18] Akhiezer A. I. and Polovin R. V., Sov. JETP 3, 696, 1956

[19] Coffey T. P., Phys. Fluids 14, 1402, 1971

[20] T. Katsoules and W. B. Mori, "Wave-breaking amplitude of relativistic oscillations in a thermal plasma" Phys. Rev. Lett., vol. 61, no. 1, pp.90, 1988

[21] N. A. Krall and A. W. Trivelpiece, "Principles of Plasma Physics", page 251, 1973

[22] C. K. Birdsall and A. B. Langdon, "Plasma Physics via Computer Simulation", Foreword by J. Denavit, 1985

[23] W. Lu, C. Huang, M. Zhou, W. B. Mori, and T. Katsouleas, "A nonlinear kinetic theory for multi-dimensional plasma wave wakefields", Phys. Rev. Lett., vol. 96, 165002, 2006

[24] Mora P. and Antonsen Jr. T., "Kinetic modeling of intense, short laser pulses propagating in tenuous plasmas", Phys. Plasma, vol. 1, pp. 217-229, 1997

[25] C. Huang et. al. "Hosing instability in the blow-out regime for plasma wakefield", Phys. Rev. Lett., vol. 99, 255001, 2007

[26] M. Zhou et. al., "Beam head erosion in self-ionized plasma wakefield accelerators", Proceedings of PAC07, Albuquerque, NM, June 2007, p. 3064

[27] F. S. Tsung, R. Narang, W. B. Mori, C. Joshi, F. A. Fonseca, and L. O. Silva, "Near-GeV-energy laser-wakefield acceleration of self-injected electrons in a centimeter-scale plasma channel", Phys. Rev. Lett., vol. 93, no.18, 185002, 2004

[28] S. Deng et. al. "Modeling of beam-ionized sources for plasma accelerators", Proc. PAC, pp.1933, 2003

[29] M. Zhou et. al. "Modeling self-ionized plasma wakefield acceleration for afterburner parameters using QuickPIC", Proceedings of PAC05, Knoxville, TN, May 2005, p. 2905

[30] The E-167 Collaboration, "Multi-GeV Plasma Wakefield Acceleration Experiments", proposal, 2005

[31] The E-168 Collaboration, "Multi-GeV Plasma Wakefield Acceleration Experiments", proposal, 2006

[32] H. Nakanishi et. al. Nucl. Instrum. Mesh., vol. A328, p. 596, 1993

[33] A. Modena et. al. "Electron acceleration from the breaking of relativistic plasma waves", Nature, vol. 337, pp. 606-608, 1995

[34] T. C. Chiou, T. Katsouleas, C. Decker, W. B. Mori, J. S. Wurtele, G. Shvets and J. J. Su, "Laser wakefield acceleration and optical guiding in a hollow plasma channel", Phys. Plasma, vol. 2, pp.310-318, 1995

[35] S. P. D. Mangles, C. D. Murphy, Z. Najmudin et. al., "Monoenergetic beams of relativistic electrons from intense laser-plasma interactions", Nature, vol. 431, pp. 535, 2004

[36] C. G. R. Geddes, Cs. Toth, J. van Tilborg et. al., "High-quality electron beams from a laser wakefield accelerator using plasma-channel guiding", Nature, vol. 431, pp. 538, 2004

[37] J. Faure, Y. Glinec, A. Pukhov et. al., "A laser-plasma accelerator producing monoenergetic electron beams", Nature, vol. 431, pp. 541, 2004

[38] W. P. Leemans, et al., "GeV electron beams from a centimetre-scale accelerator", Nature Phys. 2, p.696, 2006

[39] C. Joshi, B. Blue, C. E. Clayton et. al. "High energy density plasma science with an ultrarelativistic electron beam", Phys. Plasma, vol. 9, no. 5, pp. 1845, 2002

[40] Lee, S. et. al., "Energy doubler for a linear collider", Phys. Rev. STAB, vol. 5, 011001, 2002

[41] R. Keinigs and M. E. Jones, " ?? ", Phys. Fluids 30, 252, 1987

[42] P. Muggli et. al., "Meter-scale plasma-wakefield accelerator driven by a matched electron beam", Phys. Rev. Lett., vol. 93, no. 1, 014802, 2004

[43] B. E. Blue et. al., "Plasma-wakefield acceleration of an intense positron beam", Phys. Rev. Lett., vol. 90, no. 21, 214801, 2003

[44] M. Hogan et. al., "Multi-GeV energy gain in a plasma wakefield accelerator", Phys. Rev. Lett., 95, 054802, 2005

[45] M. Tigner, Physics Today, Vol 54, Nb 1, Jan 2001

[46] C. Clayton et. al., "Transverse betatron dynamics of a 30 GeV beam in a long plasma", Phys. Rev. Lett., vol. 88, 154801, 2002

[47] C. O'Connell et. al., "Dynamic focusing within a single ultra-relativistic electron bunch", Phys. Rev. Special Topics-AB, vol. 5, 121301, 2002

[48] M. Hogan et. al., "Focusing of a positron beam", Phys. Rev. Lett., vol. 90, 205002, 2003

[49] P. Muggli et. al., "Halo formation around positron beam core", to be submitted for publication

[50] S. Wang et. al., "Demonstration of a plasma wiggler with high beam brightness", Phys. Rev. Lett., vol. 88, 135004, 2002

[51] D. K. Johnson et. al., "Positron production by X rays emitted by betatron motion in a plasma wiggler", Phys. Rev. Lett., vol. 97, 175003, 2006

[52] Pointed out by D. L. Bruhwiler, Advanced Accelerator Conference, 2002

[53] C. O'Connell et. al., "Plasma production via field ionization", Phys. Rev. Special Topics-AB, vol. 10, 101301, 2006

[54] E. Oz et. al., "Ionization-induced electron trapping in ultrarelativistic plasma wakes", Phys. Rev. Lett., vol. 98, 084801, 2007

[55] V. Yakimenko and R. Ischebeck, "Summmary report of e-beam driven accelerators working group", Proceeding of 12th Advanced Accelerator Concepts Workshop, p. 158

[56] J. Rosenzweig et al., Phys Rev. Lett. 95, 195002, 2005

[57] R. Gholizadeh et al., "Analysis of ion motion and scattering in the extreme regime of high intensity electron beams in plasma wakefield accelerators", Proceeding of 12th Advanced Accelerator Concepts Workshop, p. 504

[58] Francis F. Chen, "Introduction to plasma physics and controlled fusion, second edition", based on formulae from p.180 to p.181

[59] J. M. Dawson, "Particle simulation of plasmas", Reviews of Modern Physics, vol. 55, no. 2, 1983

[60] C. Huang, "Quasi-static modeling of beam-plasma and laser-plasma interactions", Ph.D. dissertation, 2005

[61] C. Huang, "Development of a novel PIC code for studying beam-plasma interactions", Master's thesis, 2003

[62] C. Huang, Private communication

[63] In [3], it was argued that $D_j = D_\rho = (\Delta x)^2$ since the scale that $\mathbf{j}_{\perp\xi}$ and ρ vary is on the order of the transverse grid size (which resolves the plasma wavelength). In a more general situation where the plasma density can vary, the scale is better represented by c/ω_p.

[64] V. K. Decyk and C. D. Norton, "UCLA Parallel PIC Framework", Comput. Phys. Commun. 164, pp. 80, 2004

[65] M. V. Ammosov et. al. "Tunnel ionization of complex atoms and of atomic ionis in an alternating electromagnetic field", Sov. Phys. JETP, Vol. 64, No.6, pp.1191, 1986

[66] D. Bauer and P. Mulser, "Exact field ionization rates in the barrier-suppression regime from numerical time-dependent Schrodinger-equation calculations", Phys. Rev. A., Vol. 59, No.1, pp.569, 1999

[67] D. L. Bruhwiler et. al. "Particle-in-cell simulations of tunneling ionization effects in plasma-based accelerators", Phys. Plasmas, Vol. 10, No.5, pp.2022, 2003

[68] S. August et. al. J. Opt. Soc. Am. B, 858,1991

[69] R. Hemker, Ph. D thesis, UCLA (2000)

[70] R. Fonseca et. al., Lect. Notes Comput. Sci., 2331, 342 (2002)

[71] J. D. Jackson "Classical electrodynamics", Third edition, 1999

[72] P. Michel et. al., "Radiative damping and electron beam dynamics in plasma-based accelerators.", Phys. Rev. E, Vol. 74, No. 2, pp. 26501-1-14, 2006

[73] G. W. Ford and R. F. O'Connell, Phys. Lett. A 174, 182, 1993

[74] Calculation performed by Adrian Down, UC Berkeley, Summer 2006. Note: an alternative form of the relativistic Larmor formula (with $\beta = \frac{v}{c}$) was used.

[75] Miaomiao Zhou, "Development and applications of the ionization package in QuickPIC – a novel quasi-static PIC code for PWFA study", master's thesis, 2005

[76] R. Siemann, "Betatron motion in action-angle variables", ARDB notes ARDB-284, SLAC, 2002

[77] Simulations performed and analyzed by Adrian Down, UC Berkeley, Summer 2006.

[78] John von Neumann, "Various techniques used in connection with random digits", John von Neumann, Collected Works, volume V. Oxford, 1963

[79] H. L. Buchanan, "Electron beam propagation in the ion-focused regime", Phys. Fluids 30 (1), p. 221, 1987

[80] J. Krall, et. al., "Numerical simulations of axisymmetric erosion processes in ion-focused regime-transported beams", Phys. Fluids B 1(10), p. 2099, 1989

[81] N. Barov et. al., "Propagation of short electron pulses in underdense plasmas", Phys. Rev. E, Vol. 49, No. 5, p. 4407, 1994

[82] N. Barov et. al., "Propagation of short electron pulses in a plasma channel", Phys. Rev. Lett., Vol. 80, No. 1, p. 81, 1998

[83] P. W. Werner et. al. , "Erosion of a relativistic eletron beam propagating in a plasma channel", Phys. Rev. Lett., Vol. 73, No. 22, p. 2986, 1994

[84] William M. Sharp and M. Lampe, "Steady-state treatment of relativistic electron beam erosion", Phys. Fuids 23 (23) p. 2383, 1980

[85] S. Lee, T. Katsouleas, R. G. Hemker, E. S. Dodd, and W. B. Mori, " Plasma-wakefield acceleration of a positron beam", Phys. Rev. E., Vol. 64, 045501, 2001

[86] D. L. Bruhwiler et. al. "Simulation of ionization effects for high-density positron drivers in future plasma wakefield experiments", Proceedings of PAC03, 2003, p. 734

[87] J. S. T. Ng et. al., "Observation of plasma focusing of a 28.5 GeV positron beam", Phys. Rev. Lett., Vol. 77, No. 24, 244801, 2001

[88] K. V. Lotov, "Acceleration of positrons by electron beam-driven wakefields in a plasma", Phys. Plasma, Vol. 14, 023101, 2007